Multi-proxy analysis of the sedimentary and climatic response to the Palaeocene-Eocene Thermal Maximum in the Hengyang Basin, Hunan Province, China

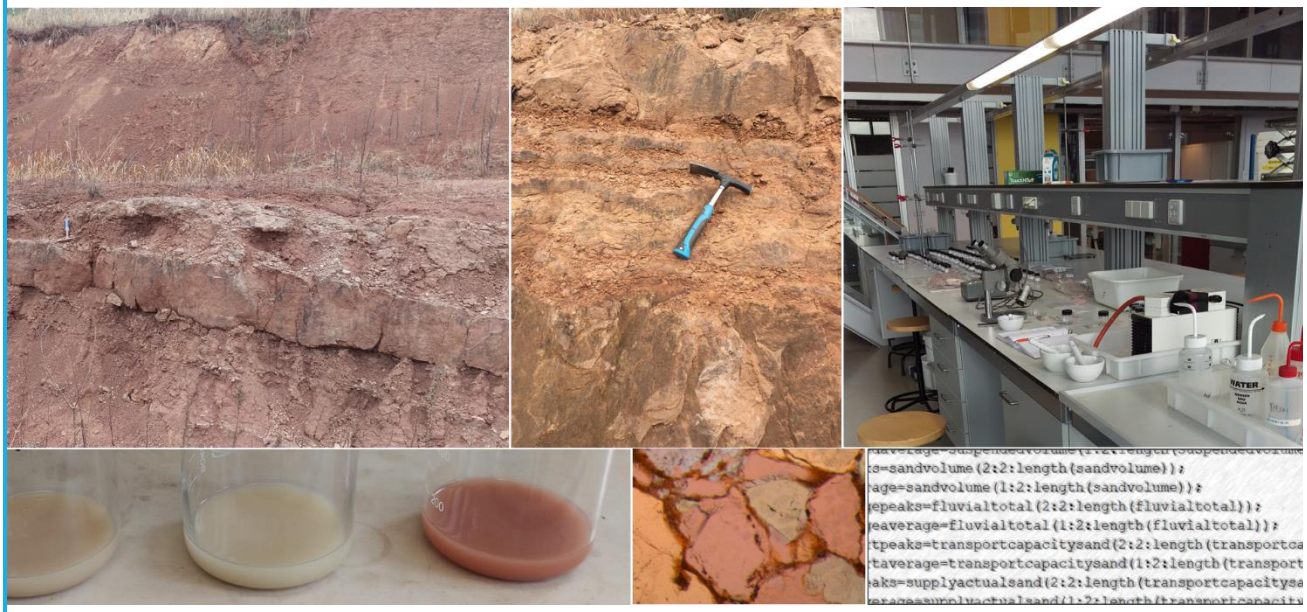

Author: Matthias Mäder

Student Number: 4621379

MSc Thesis
Applied Earth Sciences

TU Delft Delft University of Technology

Faculty of Civil Engineering & Geosciences
Department of Geosciences and Engineering

August 08, 2018

Multi-proxy analysis of the sedimentary and climatic response to the Palaeocene-Eocene Thermal Maximum in the Hengyang Basin, Hunan Province, China

By

Matthias Mäder

To obtain the degree of Master of Science at the Delft University of Technology

To be defended publicly on Thursday August 16, 2018

Thesis Committee:

Dr. H.A. Abels	TU Delft – Department of Geoscience and Engineering
Dr. J.E. Storms	TU Delft – Department of Geoscience and Engineering
Dr. M. Vizcaino	TU Delft – Department of Geoscience and Remote Sensing

TU Delft Delft University of Technology

Contents

Abstract

The Paleocene-Eocene Thermal Maximum (PETM) was a time of relatively abrupt climate change with intensive atmospheric greenhouse warming of 5 - 8˚C and is regarded as quasi-analogous for the modern anthropogenically-induced global warming. It therefore attracted considerable attention from geologists over the last decades. The PETM occurred 56 million years ago and is characterized by a sharp negative $\delta^{13}C$ isotope excursion which has been observed in terrestrial and marine sediment records the world over. The PETM global warming led to a significant alteration in regional climate and to an enhanced hydrologic cycle which triggered an increase in weathering and sediment discharge from catchments to basins.

The sedimentary, biotic, and climatic responses to the PETM have been studied intensely on the American and European continents. However, detailed analyses of the impact to the PETM on the Asian continent remain rare. Here, a detailed analysis of the sedimentary and climatic response to the PETM in the Hengyang Basin, Hunan Province, China, is presented. High-resolution isotope measurements of pedogenic carbonate nodules reveal the characteristic isotope excursion of the PETM and strongly improve the previous low-resolution isotope series. Pedogenic features and clay types of PETM floodplain deposits indicate oxic conditions and a climate with pronounced seasonality in which intensive dry periods alternated with wet seasons. Grain size analysis of the paleosols support the hypothesis of coarsening deposits as a response to the PETM even though the coarsening is not strongly pronounced. Sediment bypassing and a depleted regolith in coarse material is suggested as the main reasons for the only minor pronounced coarsening in the PETM units. A generalized PETM model, which was simulated in PaCMod, a spatially lumped numerical model developed at the University of Delft, Netherlands, predicts an increase in net precipitation and erosion in the catchment area during the PETM. As a result, the simulated water discharge increases and lead to increased bedload and suspend load transport within the river system. These modelled results are correlative with the geological findings in the Hengyang basin. The Chinese terrestrial PETM record studied here corroborates the global continental impact of the greenhouse warming event through a shift towards pronounced aridity alternating with intensified wet seasons resulting in an oxic floodplain environment with a minor coarsening in grain size.

Keywords

Paleocene-Eocene Thermal Maximum, Paleosols, Clay minerals, Grain size, End-member modelling, Thin section, Sediment-Transport model, palustrine, alluvial, Hengyang basin

List of abbreviation

CIE	Carbon Isotope Excursion
Cl	Chlorite
EM1, EM2, EM3, EM4	End-member 1, 2, 3, 4
F	Feldspar
I	Illite
I-Sm	Mixed-layer Illite - Smectite
K	Kaolinite
K-Sm	Mixed-layer Kaolinite - Smectite
K/Sm	Kaolinite / Smectite - ratio
MAP	Mean Annual Precipitation
MAT	Mean Annual Temperature
PETM	Paleocene-Eocene Thermal Maximum
POE	Pre-Onset Excursion
Q	Quartz
SD	Standard Deviation
Sm	Smectite

List of Figures & Tables

1. Introduction

Around 56 million years ago, a relatively abrupt climate change with an intense period of global warming, known as the Paleocene-Eocene Thermal maximum (PETM) took place (Kennet and Stott, 1991; McInerney and Wing, 2011). The PETM is characterized by a sharp negative $\delta^{13}C$ isotope excursion (CIE) in terrestrial and marine geological records and marks the boundary from the Paleocene to the Eocene epoch (Röhl et al., 2007; Kenneth et al., 2009; Zhu et al., 2010; Jaramillo et al., 2010). This carbon isotope excursion to lighter values in atmospheric carbon dioxide indicates a rapid influx of carbon from a ^{13}C depleted reservoir such as methane hydrates into the atmosphere and ocean carbon pool. The ramifications of this gas accumulation led to a period with intensive atmospheric greenhouse warming of 5 - 8˚C (Wing et al., 2005), ocean acidification (Zachos et al., 2005; Penman et al., 2014) and a biotic impact on fauna such as dwarfing or emergence of land mammals (Gingerich, 2003; Gingerich, 2010; Koch et al., 1992). Analysed oxygen isotope ratios of benthic and planktonic foraminifera indicated a warming of about 5 - 6˚C in the deep water (Kennett and Stott, 1991) and an increase in surface water temperature of about 3 - 4˚C (McInerney and Wing, 2011). The source of this huge amount of isotopically light carbon release is still under debate (McInerney and Wing, 2011). The most prominent causes being discussed are thermal dissociation of marine methane clathrates reservoirs (Dickens, 2000), orbitally paced carbon release from permafrost (DeConto et al., 2010), rapid burning of accumulated terrestrial organic carbon (Kurtz et al., 2003), and volcanic outgassing in the North Atlantic (Svensen et al., 2004).

The duration of the CIE onset is currently also at issue. Wright and Schaller (2013) claimed an onset duration of the $\delta^{13}C$ isotope excursion of only 13 years, which was rejected by other scientists (Zeebe et al., 2014; Pearson and Thomas, 2015). Other researchers suggested a much longer duration in the range of 5 – 20 ky (Magioncalda et al., 2004; Zachos et al., 2005; McInerney and Wing, 2011; Van der Meulen, 2015). Studies of continental sediments in the Bighorn basin, Wyoming USA, were based on cycle counts of external forcing and sedimentation rates and estimated a duration of the PETM phase of 115 ky and a recovery-phase of 42 ky (Abdul Aziz et al., 2008). Yet other studies emphasized the rough timescale of the PETM duration (Westerhold et al., 2018; Van der Meulen et al., 2018). The duration of the recovery and the definition of the recovery-phase remains controversial (Abdul Aziz et al., 2008; Murphy et al., 2010; McInerney and Wing, 2011; Van der Meulen, 2015; Turner et al., 2017).

Sophisticated climate models predict that an increase in global mean temperature triggers an increase in global mean precipitation (Collins et al., 2013). Furthermore, several clay mineral studies and leaf physiognomy analyses also revealed evidence of an increased intensity of the water cycle during the PETM (Bolle and Adatte, 2001; Wing et al., 2005; Chen et al., 2016). PETM is often linked with an increase in the hydrological cycle through a vigorous alteration in precipitation as a function of seasonality and region (Carmichael et al., 2017). Consequently, weathering, erosion, sedimentation rate and the runoff increased and led to higher energy discharge regimes at certain paleoenvironmental depositions (John et al., 2008; Carmichael et al., 2017). However, the real changes in precipitation patterns during the PETM are still poorly understood because of the

diverse and sometimes conflicting results of globally analysed precipitation proxies (Baczynski et al., 2017; Carmichael et al., 2017).

Several well-preserved terrestrial outcrops that contain the CIE of the PETM have been studied in detail. The Bighorn basin in Wyoming is the most elaborated fluvial geological record where the PETM and the sedimentary responses have been documented and discussed (Kraus et al., 2007; Abdul Aziz et al., 2008; Van der Meulen et al., 2015). On the European continent, a well-documented geological record containing the PETM related CIE is found in the Tremp basin in Spain (Schmitz and Pujalte, 2003; Pujalte et al., 2015; Colombera et al., 2017; Anema, 2017). The Hengyang basin in south central China represents a terrestrial record where the PETM is studied on the Asian continent (Ting, 1998; Bowen et al., 2002; Ting et al., 2003; Smith et al., 2006). The paleoenvironments in the Hengyang basin as compared to the Bighorn and Tremp basin, are not intensively documented. Previous studies that employed magnetostratigraphy and biostratigraphy showed the occurrence of PETM fauna in the carbon isotope excursion related to the PETM (Ting, 1998; Bowen et al., 2002; Ting et al., 2003; Smith et al., 2006). Nevertheless, a high-resolution isotope record with a convincing PETM $\delta^{13}C$ isotope signal remains absent. Analyses revealing crucial information that enables reconstruction of the paleoclimate such as clay composition (Singer, 1984; Yemane et al., 1987; Bolle and Adatte, 2001; Saleh, 2013; Chen et al., 2016) and characteristics of paleosols (Retallack, 1988; Kraus, 1999; Kraus and Riggins, 2007; Kraus et al., 2013) have not yet been reported. Grain size analysis to detect potential coarsening deposits as a sedimentary response to the PETM found in other geological PETM records (Pujalte et al., 2015; Colombera et al., 2017) is also lacking.

Based on previous findings on different continents, a change in pedogenic features of the paleosols, an alternation of the grain size distributions towards coarser particles and a shift in the clay mineralogy composition are expected to indicate responses to a potentially wetter and warmer climate accompanied by an increased sediment discharge. To determine if this is also the case in China the climatic and sedimentary response to the PETM in the Paleogene sediment record of the Hengyang basin is analysed in this study in the best possible detail.

This analysis is the first study that presents high resolution of $\delta^{13}C$ isotope signals based on isotope ratio mass spectroscopy results of more than 250 collected carbonate nodules from the investigated basin. Furthermore, a complete detailed stratigraphy including lithological descriptions and interpretations of the pre-PETM, PETM and post-PETM fine beds and intercalating sand bodies is presented. The lithostratigraphy is focused on four available intervals which correspond to Paleocene and Eocene strata previously indicated as containing the isotope excursion. Additionally, clay mineralogy composition analysis was conducted to unveil possible changes as a response to climatic shifts during the PETM. Grain size analysis was performed to detect potential trends in the clastic grain size distribution during the pre-PETM, PETM body and recovery-phase, revealing information about transport and sediment discharge. Further, thin sections of the collected sand samples were analysed using microscopy to emphasize evidences of changes in sediment deposition, transport path and mineralogy as a response to the abrupt climate change.

As already mentioned, most sediment records and climate models predict that weathering, erosion, sedimentation rate and runoff increased triggered by global temperature increase during the PETM. Here a spatially lumped numerical simulation catchment model called PaCMod, which was created at Delft University of Technology (Forzoni et al., 2014), was used to investigate downstream sediment transport propagation within a fluvial catchment in reaction to greenhouse warming. A general scenario with typical PETM input parameters was implemented to simulate the climate and sedimentological response to the PETM in terms of precipitation, water discharge, erosion rate, sediment transport and storage. The results are presented and compared with the field observation findings as well as the rock analysis from the Hengyang basin.

In the following section the geological setting and findings of previous work in the Hengyang basin are described. The methodology and the results of the field studies, laboratory grain size analysis, thin section evaluation, clay composition and stable isotopes measurements are then presented. Thereafter, the simulated outcomes of the numerical modelling for a general PETM scenario are presented. Finally, the results are critically discussed, and conclusions and recommendations are drawn.

2. Hengyang Basin

2.1 Palaeogeographical setting - Geological chronology

The global geographical settings at early Paleogene looked almost the same as the geographical setting in present age. However, there was one major difference in the region of south-east Asia. Videlicet, the Indian plate was likely separated from the Eurasia plate (**Figure 1A**). Studies of palaeomagnetic reconstructions revealed a very high drifting speed of the Indian plate towards the Eurasia plate during the late Cretaceous (Klootwijk et al., 1992). The timing of the final collision is under debate (Aitchison et al., 2007; Zhu et al., 2015) but suggested ages lie in the range between 50 and 59 My ago (Bouilhol et al., 2013; Hu et al., 2017). Even in case of an early (59 ± 1 My) collision (Hu et al., 2017), the proto Himalaya orogen grew slowly and reached roughly 1 km at late Paleocene and 2.3 km in the beginning of the Miocene (Ding et al., 2017) and is therefore only of minor extent at PETM time.

The region of the Hengyang basin is marked by shortening during the Mesozoic and crustal extension during the Jurassic to early Cenozoic (Li and Li, 2007). The basin consists of a Triassic to Jurassic marine terrestrial sequence and a late Mesozoic to Cenozoic terrestrial sequence which is composed of fluvial and lacustrine sandstones and mudstones (Yan et al., 2011). The results of relatively young (80 - 120 My) detrital zircon U-Pb measurements suggest that the Upper Cretaceous sandstones are linked with Cretaceous granitic volcanism alongside the south-eastern margin of South China indicating the existence of a coastal mountain belt catchment with a related sediment transport in a south-west direction to the basin during late Cretaceous to early Tertiary (Yan et al., 2011) (**Figure 1B**). The paleo coordinates of the Hengyang basin were estimated at 27 °N and 108 °E (Fossilworks database, 2016) and forecloses a significant latitudinal motion to its current location which was also found in the paleomagnetic study of Late Cretaceous and Paleogene records in the basin (Sun et al., 2006).

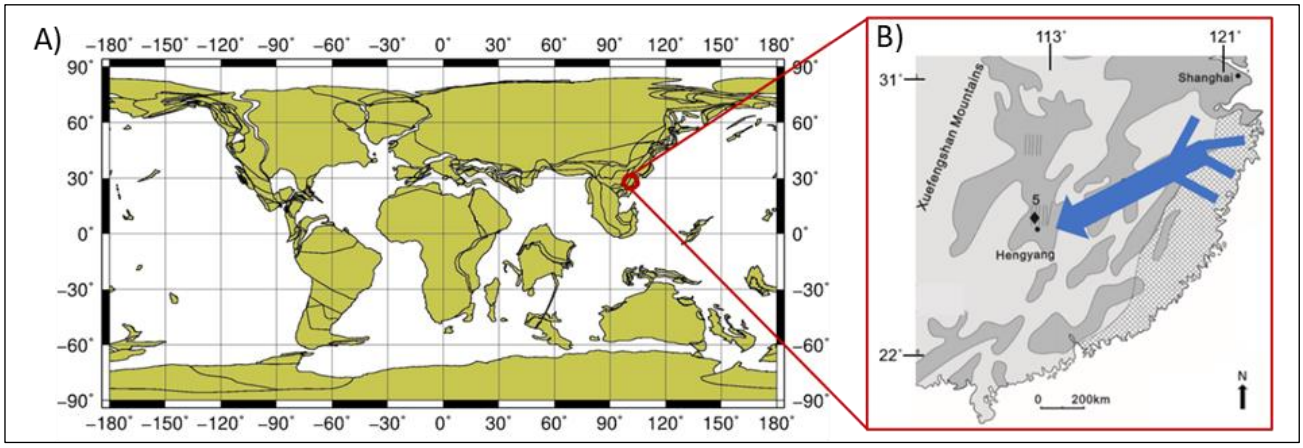

Figure 1. The paleo-geographical setting at 65 My ago (Panel A). Panel B shows a detail of the Hengyang basin at present location with the expected late Cretaceous and early Paleogene sediment transport path indicated in the blue arrow according to Yan et al. (2011). (Panel A from http://www.odsn.de/odsn/services/paleomap/paleomap.html and Panel B modified after Yan et al., 2011)

2.2 Geological setting

The Hengyang basin is situated in the south China craton at the border between the Cathaysian block and the Yangtze block (Yan et al., 2011). The basin is approximately 5200 km^2 and lies in the Hunan Province near the city of Hengyang in south-central China (Liu and Fu, 1986) (**Figure 2A**). The basin is characterized by a syncline structure with a corresponding fold axis running in a south-west to north-east direction (Bowen et al., 2002) (**Figure 2B**).

At present, the basin is terminated by hilly late Paleozoic rocks in the south and by the Heng Shan mountain in the north. A barrier of upper Paleozoic formations in the east and by the mountain range on the border between Hengyang and Changning in the west restricts the basin in the other cardinal direction (Young et al., 1938). The basin is characterized by Cretaceous and Paleogene red beds (Ting et al., 2003). Two sections on the south limb have been reported. Section 1 is between Lingcha and Baijialong, which mainly consist of sandstone intercalated with red mudstone. Section 2 is close to Limuping and is poorly documented (Bowen et al., 2002; Ting et al., 2003). Section 3 lies on the north limb between the two villages Lingcha and Tianzhicun.

Two main formations, namely the upper Lingcha Formation and the stratigraphically lower Limuping Formation have been identified and described (Wang et al., 2011). The Upper Lingcha Formation contains 12 mammalian species and is of PETM age (Ting et al., 2012). The lower Lingcha fauna in the Limuping Formation preserves one mammalian and one reptilian species that have been determined to lie within the timescale of the C25n/C24r reversal and is therefore interpreted as late Paleocene (Bowen et al., 2002; Ting et al., 2003; Wang et al., 2011). The Palaeocene-Eocene boundary was determined to be within the Lingcha Formation in section 3 at a stratigraphic level of 238 m which corresponds to the lowest point where the CIE was detected (Wang et al., 2011).

In this study, the focus was on the upper parts of section 3 on the north limb due to the quality, thickness, continuity and accessibility of the exposed outcrops.

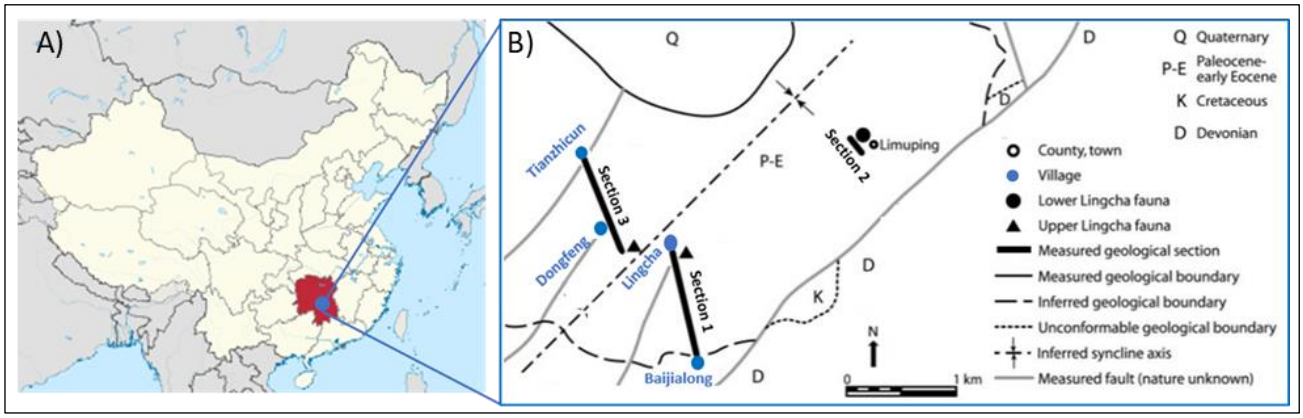

Figure 2. Panel A depicts the investigated area in south-central China. Panel B represents the previous investigated sections of the Hengyang basin. This study focuses on the upper parts of section 3 close to Lingcha on the north limb of the syncline. (Panel A from Wikipedia, Panel B modified after Bowen et al, 2002).

3. Methodology

3.1 Field research - lithological logs

The upper part of section 3 of Bowen et al. (2002) between Lingcha and Dongfeng village (**Figure 2B**) was sampled in detail in four stratigraphic intervals nearer to Dongfeng village and was therefore named as Dongfeng section. The four intervals of the Dongfeng section were named with 3A, 3B, 3C, 3D (**Figure 3**) and are based on already existing and accessible outcrops or from dug trenches in covered intervals or within the outcrops. The digging of trenches was needed because of the presence of vegetation and human activities on site.

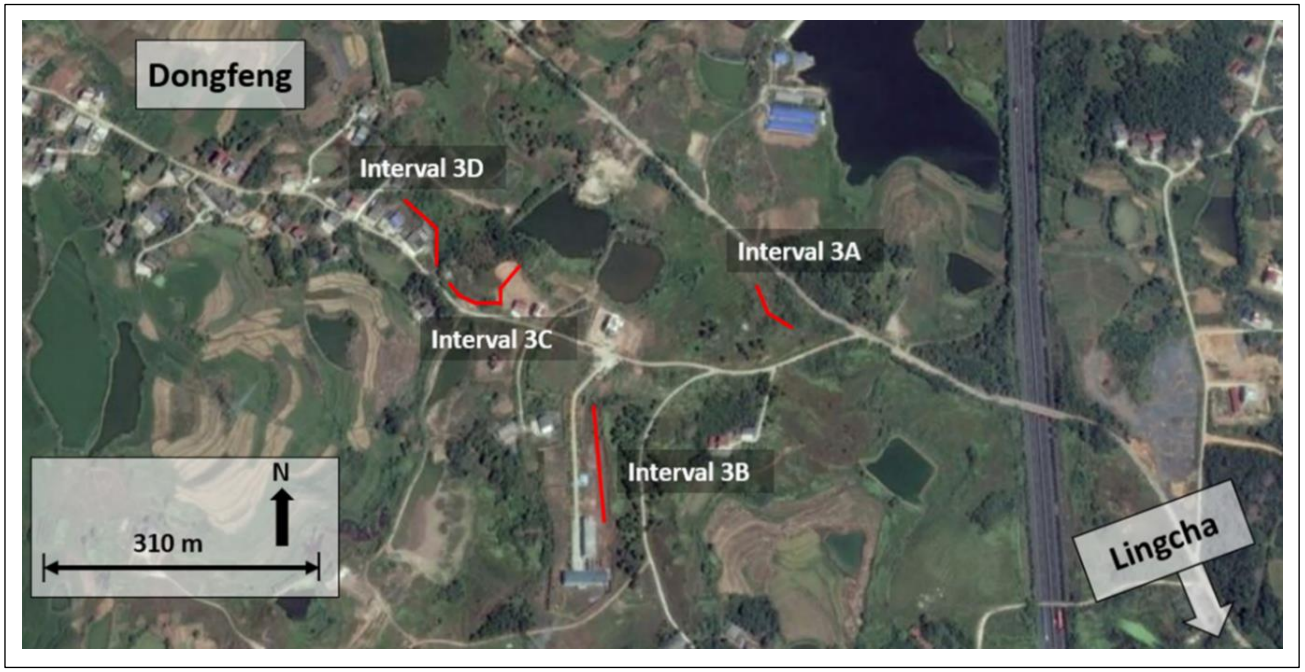

Figure 3: Satellite photo from Google Maps showing the study area near Dongfeng village. The Dongfeng section is composed of the four study intervals (3A, 3B, 3C, 3D) indicated by red lines.

All outcrops were cleaned from weathered stratum. The trenches were approximately 1 m deep, 1 m wide, and up to 2 m in vertical length. The stratigraphic intervals (3A, 3B, 3C, 3D) were separated from each other and no stratigraphical contacts were exposed or found. Separately dug trenches within an interval were related to each other through following lateral continuous marker beds. The four stratigraphic intervals correspond to a total stratigraphic thickness of about 50 meters when excluding the stratigraphic gaps and a corresponding total stratigraphy of 65.5 m when including the gaps.

The locations were tracked with a GeoXT Trimble dGPS tool. The dip direction and dip angle were measured at different locations using a conventional compass. The dip direction and dip angle were assumed to be constant since no unconformity is exposed. The dip direction and dip angle measurements were averaged to 140˚/07˚. Using this orientation together with the measured GPS location data, the stratigraphic gaps between the four

outcrops were approximated by means of the software QGIS and trigonometric projection. Finally, the approximated gaps were compared with the field estimates which are then shown to be close to the approximations. Because of the potential occurrence of faults and the wide range of measured dip directions (110˚ - 180˚) and dip angles (4˚ - 10˚) in the field the approximated stratigraphic gaps are fraught with uncertainties. A difference in dip angle of 3˚ over 200 meters can lead to a difference in vertical direction of around 10 meters. Therefore, it is possible that the stratigraphic gaps presented here are underestimated in the range of 0 to 10 meters, neglecting the error range of the GPS measurements.

Interval 3A with the geographical coordinates 27.024˚N, 112.835˚E and a continuous thickness of 11.5 meters is composed of 8 connected trenches and represents the stratigraphical uppermost, respectively the geological youngest interval of the Dongfeng section. Outcrop 3B is in an occasionally active chemical factory at 27.022˚N, 112.832˚E and has a thickness of 13.0 meter and lays stratigraphically below interval 3A. Interval 3C represents the thickest stratigraphical succession of the Dongfeng section. The succession consists of two connected outcrops with the geographical coordinates 27.024˚N, 112.830˚E and has an overall thickness of 15.75 meters. The stratigraphically lowest and therefore the geological oldest interval 3D is exposed at 27.025˚N, 112.830˚E and is composed of 6 connected trenches with a summed thickness of almost 10 meters.

The sand bodies were described in terms of size, shape and sorting of the grains and distinctive depositional structures and features. The fine layers were described at cm scale in grain size, the matrix and mottling colours using the Munsell colour charts and characteristic sedimentary and pedogenic features, such as mottling, slickensides, blocky peds, carbonate nodules and fossil fragments. The facies interpretation regarding the development of the paleosols and its characteristic horizons of deposition follows the approach used in the field recognition of paleosols done by Retallack (1988).

Sandstone samples were taken of each sand layer for thin section microscopy analysis. In a previous study by Chaowen Wang (2014) of China University of Geosciences, Wuhan, China, soil samples were collected at interval 3B and 3D to perform the clay analysis.

3.2 Stable Isotope measurements

Pedogenic carbonate nodules samples were collected at a spacing of 25 cm from fresh rock surface in each stratigraphic interval. At least two carbonate nodules per spacing, where present, were used for the stable isotope ratio mass spectroscopy measurement. The nodules mainly consist of two types of carbonatic minerals, sparite and micrite. Sparite is a calcite spar and is a recrystallization product of micrite, which emerges during diagenesis and contain isotope ratios of secondary origin (Bowen et al., 2001). Therefore, the calcite spars do not reflect the original environments of deposition (Nelson, 2018). The nodules were crushed at Delft University of Technology, Netherlands, into small nodule fractions to separate micrite from spar by hand whilst using an Olympus Tokyo 206618 microscope. The pure micrite pieces were cleaned and ground into powder by use of a mortar. At Utrecht University, Netherlands, 50 – 100 µg of each micrite powder sample was weighted then sealed in air tight glass test tubes. The samples were then flushed with helium gas for at least 5 minutes under

controlled flow rates and ensured outflow conditions. This is of utmost importance to prevent atmosphere accessibility forming NO_2 during the measurement procedure and to eliminate any current atmospheric CO_2. Afterwards the samples were heated to 65˚C before they were acidized with orthophosphoric acid. 64 samples and 15 standard samples (11 naxons, 4 IAEA-CO-1) were processed in a single measurement round. Naxos, which is a carbonate sample from Utrecht University, as well as IAEA-CO-1 samples were used as standards to normalize and correct the isotope ratio measurements to the Vienna PeeDee Belemnite VPDB scale. The carbon and oxygen isotope ratios were measured by a Delta V isotope ratio mass spectrometer coupled with a Thermo Finnigan Gas Bench. The average measurement standard deviation of replicate measurements was less than 0.2‰ for the carbon and oxygen measurement. The results of the $\delta^{13}C$ are presented and discussed in the principal part of this thesis whereas the $\delta^{18}O$ signal is analysed in the supplementary material (***9.1***). The measurement procedure and the isotope ratio measurements were conducted at the Earth Science Laboratory at Utrecht University, Netherlands.

3.3 Grain size analysis – End-member modelling

The analysed rock samples contained high variabilities in minerals, grain sizes, organic material and calcium carbonate components which indicated the need to test various acid treatment procedures to obtain the purest solution and thus the most accurate and reliable results. Here, only the procedure that produced the purest solution is explained.

Initially, the samples were crushed into smaller pieces by means of a hand crusher or a Jaw Crusher machine. Afterwards, the samples were oxidized and treated with acid to avoid unwanted impurities. Thereby, 5 ml of 30% H_2O_2 solution was used to remove the organic material of the sample. Subsequently, the calcium carbonate components were removed using 10 ml of 10% HCl acid in a first round and another 5ml 10% HCl in a second round. The chemical reactions were expedited by heating the samples. Once cooled, the sample solution was left to rest for 24 hours. Finally, a $Na_4P_2O_7.H_2O$ crystal powder was used to neutralize the clay particles and further disperse the grains of the previous crushed and treated rock samples. Next, the samples were faced with an ultrasonic transducer for five minutes to separate the grains. Following this, the grain size distribution was conducted using a Sympatec HELOS/KR laser diffraction particle size measurer with advanced wet disperser QUIXEL.

The grain size measurements were conducted at the Earth Science Laboratory at VU Amsterdam, Netherlands. In total, 73 paleosol samples were measured. The sandstone samples of interval 3B and 3C were analysed using a microscope and not by this method. The obtained results reveal statistics about the mean grain size as well as the percentage of clay, silt and sand. Furthermore, the standard deviation, median, skewness and kurtosis were automatically computed. All particles smaller than 8 µm were defined as the clay fraction. The silt fraction was determined by grains having a size range of 8 µm – 63 µm and the largest grains > 63 µm were specified as sand particles. The grain size distributions were separately analysed using box plots for the 3 distinctive phases, namely pre-PETM, PETM body, and recovery. Furthermore, end-member modelling was conducted to

investigate grain size distribution patterns. The end-member modelling was realized in MATLAB by means of the AnalySize version 1.1.0 algorithm by Paterson and Heslop (2015) combined with the non-parametric fitting approach of Van Hateren et al. (2017).

3.4 Clay analysis

The clay composition has been analysed by Dr. Chaowen Wang at State Key Laboratory of Geological Processes and Mineral Resources at the China University of Geosciences (Wuhan), China. Rock samples were collected in a previous study at two distinctive stratigraphic intervals, 3B and 3D which correspond to the PETM body (3B) and pre-PETM phase (3D). Each sample was analysed for percentage composition of clay minerals. The clay composition from the pre-PETM rocks were compared with the clay composition from the PETM body. The clay fraction was isolated from the bulk material by employing a procedure used by Jackson (1975). The entire clay analysis procedure is described in detail by Wang et al. (2017).

3.5 Sandstone Thin section – microscopic analysis

Samples were taken from each sandstone layer in the field. Thin sections were prepared at the Earth Sciences Laboratory of Utrecht University, Netherlands. The 30 µm thick thin sections were analysed by means of a polarisation microscope of the type "Leity Laborlux 11 Pol S". The samples were analysed in terms of their grain size and shape to reveal information about the sedimentary maturity. The mineral content was determined, and the sandstone classified using the schema presented in Folk et al. (1970). The structure and composition of the matrix was described based on the classification of Pettijohn et al. (1973) to obtain crucial information regarding the depositional environment. A further search for potential deformation of elongated weak minerals and other evidence of diagenesis such as pressure solution was performed to attempt to predict the burial history of the samples. Microscopic analysis was used to spot possible differences between the pre-PETM and PETM samples. To do this, thin sections were separated into the two distinctive phases of deposition. The division of the two groups was only feasible due to the similarity of the individual samples of each group.

3.6 PETM – Modelling with PaCMod

PaCMod is a spatially lumped numerical catchment model with short computation time and was developed to simulate time dependent sediment and water flux feedbacks to climatic, environmental and tectonic inputs. The catchment is the upland which acts as the mainly erosional part of a drainage basin in which sediments can be transiently stored on hillslopes, alluvial fans, confined floodplains and channel deposits. The extensive description of PaCMod is presented in Forzoni et al. (2013; 2014) and Forzoni (2014).

PaCMod is used to investigate the response of downstream sediment flux to typical and generalized PETM climate inputs. The focus of the simulation is on the resulting water discharge and on the sediment transport and storage. Water discharge strongly depends on precipitation and evaporation which are both expected to be

boosted because of the massive temperature increase during the PETM (Wing et al., 2005). The sediment transport is analysed in terms of bedload and suspended load within the river which can reveal general information about the transported grain size. The sediment transport is also dependent on the sediment supply and the transport capacity which are also simulated.

The biggest unknown but critical factor that influences erosion, transport and sediment storage is precipitation. Precipitation is calculated by means of the MATLAB routines of the climate catchment model in PaCMod. These calculations are based on typical PETM input parameters which are divided into three sections namely, climate, morphology and lithology. These are presented in **Table 1**. The parameters of the morphology (catchment) and lithology are taken from the Hengyang Basin. The climate inputs were based on global PETM data from literature. The input parameters which are not presented in **Table 1** are less significant or contain an indefinable value because of unavailable information. Therefore, standard parameters defined for the Golo catchment based on Forzoni (2014) were used. The precipitation calculation strongly depends on altitude and temperature. The temperature input series was chosen by typical estimated PETM values and is characterized by the four distinctive temperature phases (**Figure 4**). A maximum mean annual temperature (MAT) of 30˚C during the PETM was chosen and corresponds to a modelled result by Heinemann et al. (2009). The base temperature during pre-PETM phase was set at 20˚C with a sudden increase of MAT by + 10˚C within 5 ka. The temperature during the PETM body was held constant at 30˚C for 100 ka before the recovery to lower temperatures took place. The integrated tectonics routines of PaCMod were completely neglected in the simulation due to the lack of information concerning the paleotectonic in the catchment and basin area.

The climate catchment model calculates the fluvial water discharge, which is subject to precipitation, temperature, evaporation, runoff and infiltration. Furthermore, general results for bedload and suspended load transport which represents the catchment outlet are generated. Sediment supply and the transport capacity of a river system based on the input parameters were also calculated. However, the climate catchment model reveals only general trends in sediment transport and storage and does not provide any quantitative numbers for the Hengyang basin. Nevertheless, the calculated precipitation, evaporation and water discharge can be regarded as semi-quantitative results. In a second step, the simulated precipitation from the first step is used as the main input series into the river system response model routines in PaCMod. These routines depend on the catchment area and the listed parameters in **Table 1** with additional parameters from the Golo river system presented by Forzoni (2014). These routines reveal semi-quantitative numbers concerning the erosion rate, sediment transport and sediment storage of the Hengyang Basin. The sensitivity of the input parameters is elaborately discussed by Forzoni (2014) and is therefore only briefly explained in the supplementary material (***9.3***).

Table 1. The most significant and available input parameters which were used for the numerical modelling in PaCMod. Climate parameters were selected from different locations whereas the catchment paramters were based on the Hengyang basin.

Climate parameters		
Parameter	**Value**	**Estimation based on: / Literature**
Seasonal Temperature Difference	18˚C	Snell et al., 2012
Storminess coefficient	0.5	Anema, 2017
Snow coefficient	0.01	-
Morphology – Catchment parameters		
Maximum relief	1000 m	(Estimate) Heinemann et al., 2009
Latitude	27˚	Fossilworks database, 2016
River length	400 km	Yan et al., 2011
Catchment area	10000 km^2	Yan et al., 2011
Lithology parameters		
Median Grain size (bedload)	0.25 mm	Grain size analysis

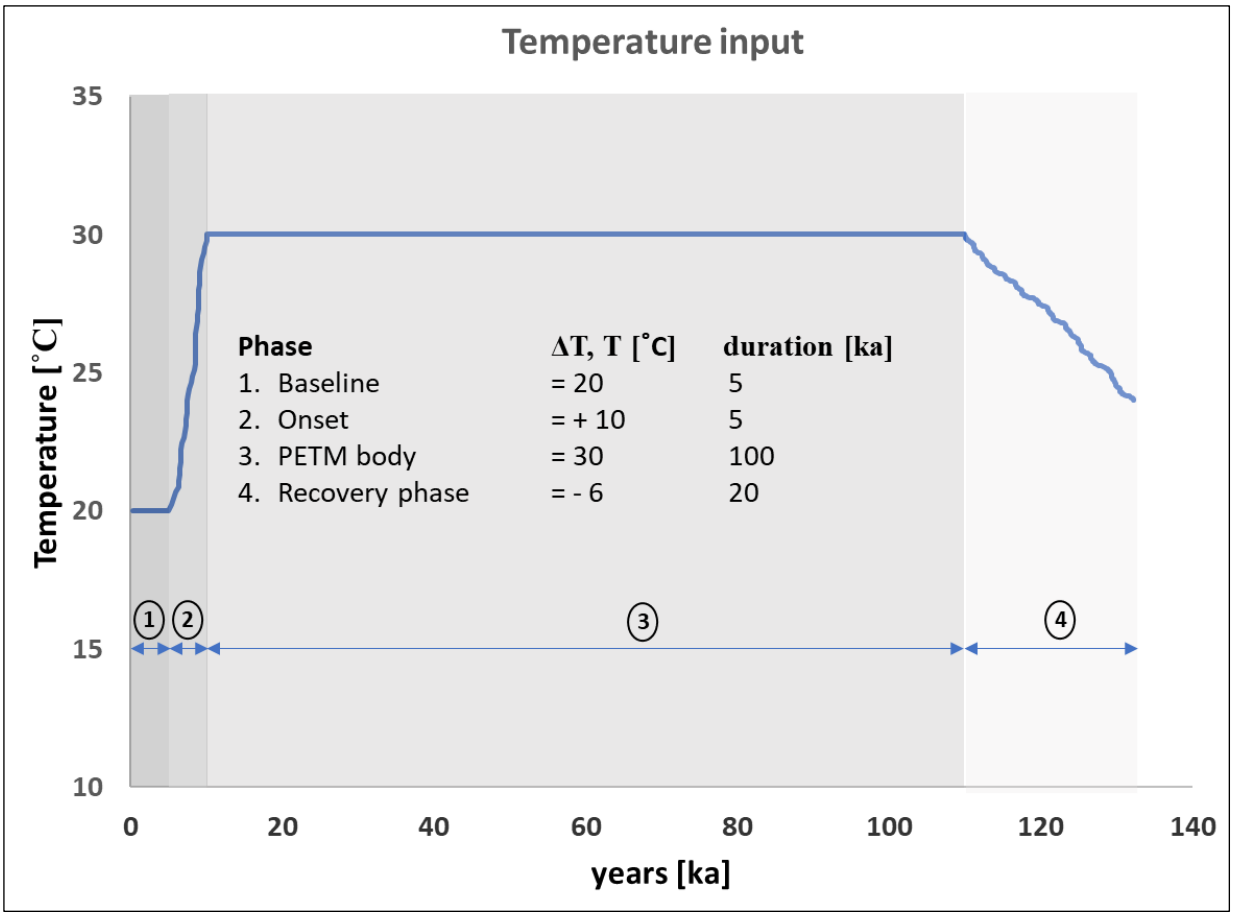

Figure 4. The used temperature input signal for the PETM with its distinctive phases.

4. Results

4.1 Stratigraphy – Facies Description and Interpretation

The stratigraphical logs that include the sedimentary and pedogenic features of the four distinctive intervals 3A, 3B, 3C, 3D of the Dongfeng section are provided in **Figure 5.2** with the corresponding legend (**Figure 5.1**).

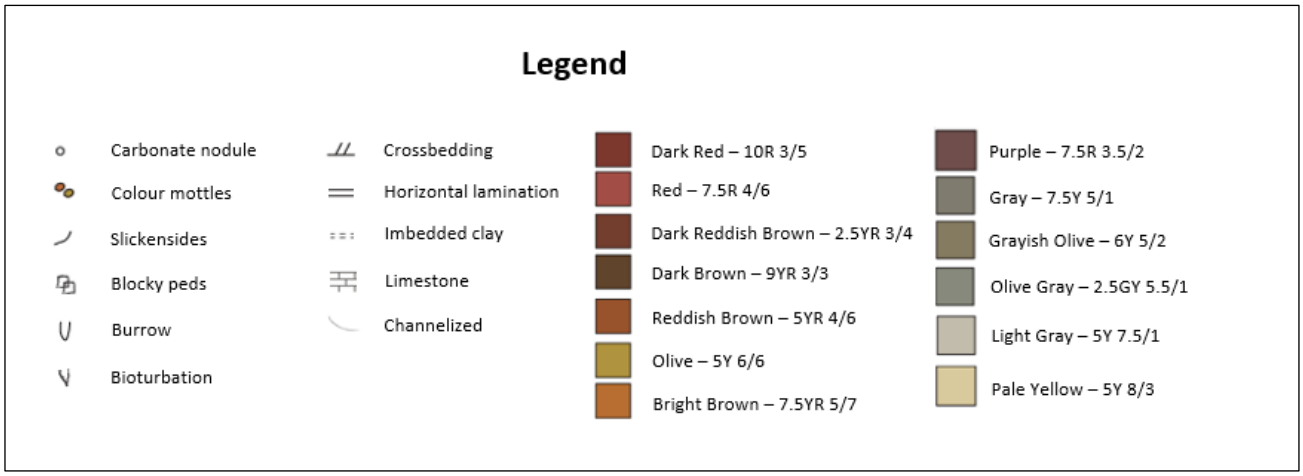

Figure 5.1. The corresponding legend for **Figure 5.2**. Note that the colour of the layers and mottles were combined into fewer colour bins to increase readability of the log.

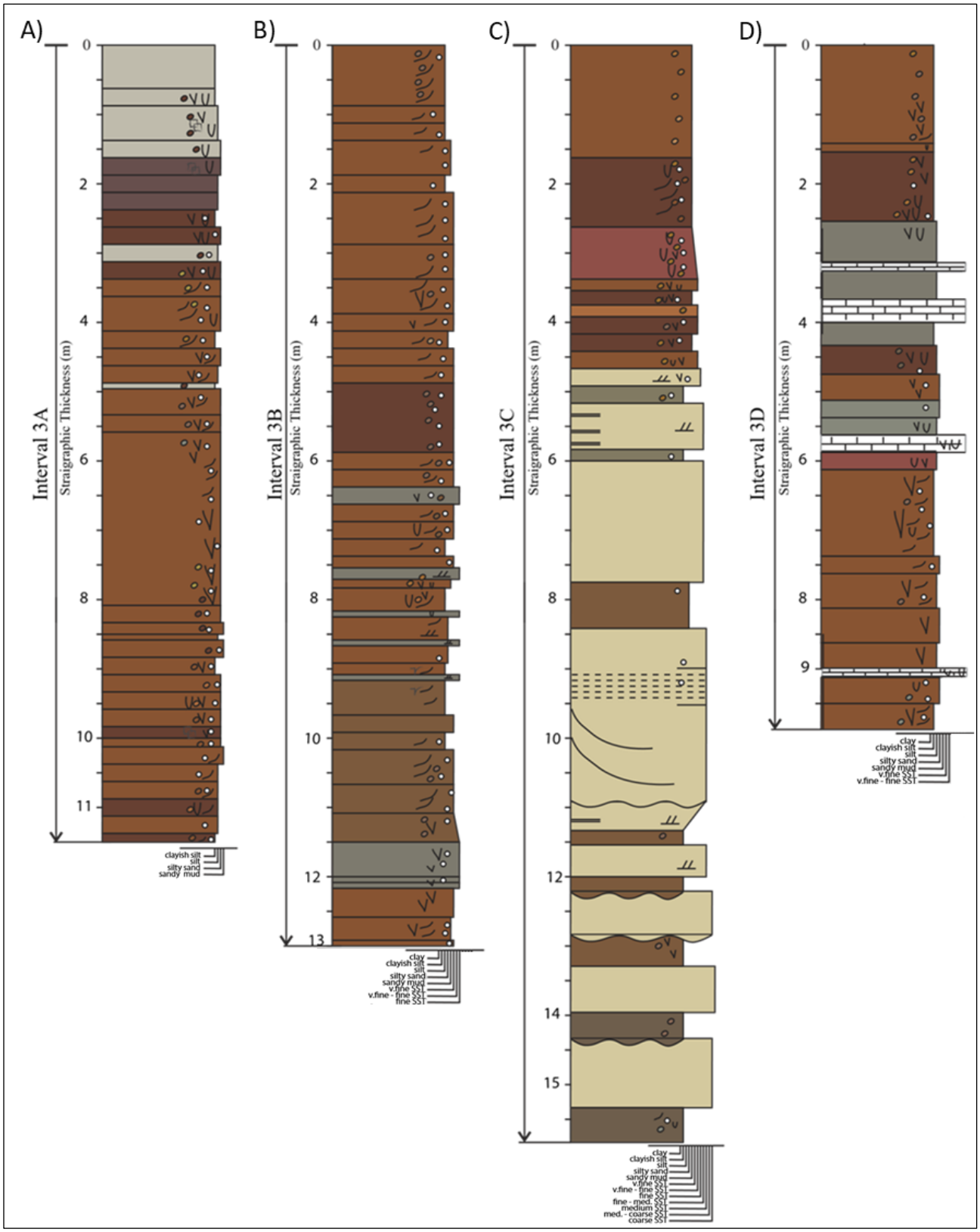

Figure 5.2. The four distinctive stratigraphic intervals of the Dongfeng section in the Hengyang Basin. The figure illustrates the lithological logs of interval 3A (Panel A), interval 3B (Panel B), interval 3C (Panel C) and interval 3D (Panel D). Interval 3A represents the geologically youngest strata and interval 3D represents the lowest and therefore oldest strata. The corresponding legend to this figure is presented in **Figure 5.1**.

4.1.1 Interval 3D – Description

Interval 3D is around 10 m thick and represents the stratigraphically oldest interval (**Figure 5.2D**). The lowest units from 10 m to 6.25 m are of reddish-brown colour (5YR) and consist of clayish silt and minor sandy silt with abundant slickensides. The layers are strongly bioturbated and contain carbonate filled burrows. Occasionally, mottles and mm scale carbonate nodules were found. At meter 9, a 10 cm thick indurated and bioturbated limestone occurs. Above the reddish-brown units, a sharp transition to limestone dominated greyish-olive units occurs (**Figure 6**). These units exhibit bioturbated carbonatic silt with carbonate filled burrows and limestone layers containing abundant ostracods. The limestone layers are classified in light grey whereas the silt layers vary in the greyish-olive to grey. A sharp transition to strongly mottled and reddish to dark reddish-brown units overlay the greyish limestone layers. These units have a grain size of silty clay and are bioturbated with burrows. Occasionally, slickenside, carbonate nodules and reduced rhizoliths were found.

4.1.2 Interval 3D – Interpretation

The carbonatic greyish-olive layers and the limestone layers were deposited in a moderately shallow lacustrine environment with subsequent pedogenesis after subaerial exposure. Aside from some mottles and slickensides, the clayish silty reddish-brown layers contain no pedogenic features and show only a moderate superimposed pedogenesis in a floodplain facies. The calcareous layers with the lighter colours are interpreted as aridisols whereas the mottled and occasionally slicked reddish-brownish clay dominated paleosols are classified as vertisols. All units of the interval 3D correspond to former B horizons.

Figure 6. The lowest part of interval 3D with the characteristic olive-greyish limestone layers intercalated with reddish-brown silty layers.

4.1.3 Interval 3C – Description

Interval 3C consists of two distinguishable parts. The lower part spans from the base to 4.75 m and is made up of sandstones alternating with silty clay units (**Figures 5.2C & 7**). The sandstone thicknesses vary from 25 cm to 2 m whereas the silty clay layers variegate between 10 and 60 cm. The silty clay layers are of dark-reddish-brown colour and are mottled. Sometimes, mm to cm scale carbonate nodules occur. The sandstones consist of fine to coarse, mostly angular sand grains. The sandstones are moderately sorted and occasionally contain small to medium sized pebbles (1 - 6 mm). The mineralogy is mainly quartz but several feldspars and large muscovite crystals (1 - 6 mm) occur. Small laminations, ripples and cross bedding are available in abundance and a clay filled channel at the stratigraphic level of 11 m exists. The upper part, ranging from 4.75 m to the top, is characterized by silty sand paleosols and very thin sandy mud layers. The silty-sandy units are slightly slicked and patchy and contain some mm to cm scale carbonate nodules. The structure is strongly mottled with a reddish, reddish-brown to purple colour. The very fine sandstone layers are strongly bioturbated with mostly vertical burrows with a size of 1 - 3 cm. The colour varies in the yellow-red range in 2.5YR and 5YR.

4.1.4 Interval 3C – Interpretation

The sandy bodies of the lower part are interpreted as fluvial channel deposits. The alternatingly imbedded silty clay layers are inferred to be episodically silty flood depositions. The distinctive pedogenic features of the intermittent silty clay layers point to periodical soil formation. However, the pedogenic development was weak. These paleosols were regarded as spodosols corresponding to former B horizons. The finer units in the upper part were deposited in distal floodplains and show a moderately developed pedogenesis and were interpreted as vertisols.

Figure 7. The lower part of the medium to coarse sand beds of outcrop 3C showing large scale cross stratification. The intercalated mottled silty clay layers are of cm to dm scale and are of dark-reddish brown colour.

4.1.5 Interval 3B – Description

Interval 3B can be divided into 2 parts. The lower part, ranging from the base to 6.4 m is constituted of sandy mud with pedogenic slickenside features, abundant carbonate nodules and very fine bioturbated 10 - 50 cm thick sandstone layers (**Figures 5.2B & 8**). These greyish sandstone layers are fine grained with angular shape and are moderately to well sorted with occasionally small angular granules (< 2 mm) in it. Blackish shale fragments with a width and length of 1 cm and mm scale carbonate nodules occur occasionally. The Munsell colour of the paleosols are in the reddish to dark-brown range of 5YR. The upper part of the interval starts from a sharp base at 6.4 m and consists of clayish silt, sandy silt and sandy mud intervals with abundant slickenside and mm to cm scale carbonate nodules which were dispersed and seldomly reduced. The matrix is mottled, and the soil colour is in the reddish-brown range of 5YR as found in the Munsell colour chart.

4.1.6 Interval 3B – Interpretation

The sandy units of the lower part are interpreted as proximal to distal crevasse splay deposits with subsequent soil formation. In contrast to these lower units, the upper mostly finer units of 3B deposited in more distal region of the crevasse lobe. These upper units show strongly developed pedogenesis because of the abundant pedogenic features and are vertic corresponding to former B horizons.

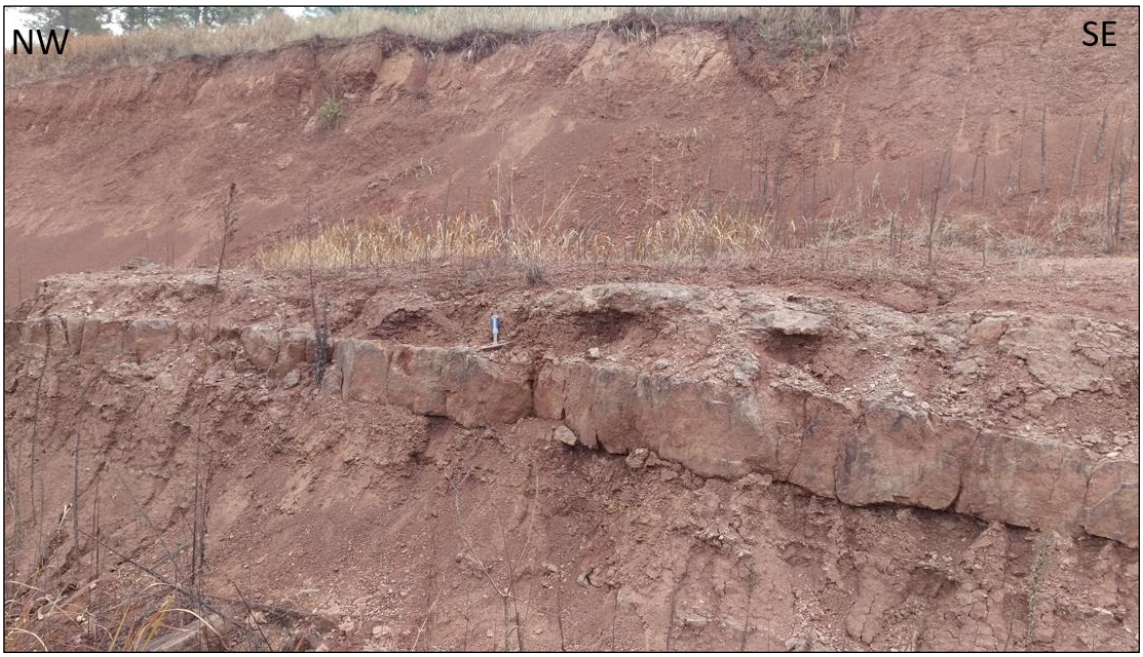

Figure 8. The photo belongs to interval 3B, which lies in a former factory. The upper part shown here consists of brownish paleosols with cm scale very fine sand beds. The lower part is characterized by red-brown paleosols intercalated by dm scale fine sand beds. The hammer in the middle of the picture is used for scale and is 30 cm in length.

4.1.7 Interval 3A – Description

Interval 3A consists of three distinguishable parts. The part from the base to the 8.25 m mark is composed of clayish silt to sandy mud (**Figure 5.2A**). The structure is mottled with abundant bioturbation and mm to cm scale carbonate nodules and occasional desiccation cracks. The colour is in the reddish brown to bright brown in the range of 7.5YR with some dark brownish layers.

The intermediate part appears homogenous and shows a grain size of silt to sandy silt with abundant mm to cm scale carbonate nodules and abundant pedogenic features, namely slickenside and mottling. Occasionally, bioturbation including burrows occurs. The Munsell colour is dominantly reddish brown in the 5YR scale.

The section from 3.4 m to the top consists mainly of bioturbated paleosols with a grain size of silt to sandy silt. Burrows and blocky peds occasionally occur in a predominantly mottled paleosol. At 1.6 m a sharp transition to light grey colours occurs whereas a purple colour dominates the units below. Besides the mottles and some blocky peds, the greyish and purple units do not show strong pedogenic features. In fact, slickensides and carbonate nodules are completely absent.

4.1.8 Interval 3A – Interpretation

The lower and intermediate units are pedogenic, strongly developed and are interpreted as vertic corresponding to a B horizon. These units were deposited in a distal region of a floodplain. In contrast, the upper purple and greyish units do not show pedogenic features and are interpreted as waterlogged floodplain facies with only moderate superimposed pedogenesis.

4.2 Carbon Stable Isotope record

4.2.1 Isotope record – Description

The results of the carbon stable isotope measurement are presented next to the stratigraphic composite log of the Dongfeng section in **Figure 9**. The carbon isotopes range between - 5.2‰ and - 14.3‰ $\delta^{13}C$. The $\delta^{13}C$ isotope signals in the lowest interval of the Dongfeng section show four distinctive isotope clusters. The lower two clusters are concentrated around - 8‰, resp. - 6 ‰ $\delta^{13}C$. The upper two clusters at the stratigraphic level of 7 - 8 m respectively 4.5 - 5.5 m show a wide spread from values of - 6‰ to - 11‰ $\delta^{13}C$. Interval 3D has a mean of - 6.9‰ $\delta^{13}C$ with a standard deviation (SD) of 1.3.

Above this interval, between 22 m and 24 m, the isotope signal shows a range of carbon isotope values between - 8‰ to - 11‰ $\delta^{13}C$. These nodules were samples from the finer sediments intercalating in the alluvial sandstone body occurring in the interval. The isotope signals from the floodplain soils directly above the alluvial sands show a less spread record averaging at - 9.2‰ ± 1.1‰ $\delta^{13}C$. This entire interval (3C) has a mean of - 9.1‰ $\delta^{13}C$ with a SD of 0.7 and depicts a shift towards lighter ^{13}C values of over 2‰ compared to the mean of the basal interval (3D) of the Dongfeng section.

In interval 3B, a cluster ranging from 37 - 41 m shows variable carbon isotope results. By contrast, above this part little fluctuation occurs around - 12.4‰ $\delta^{13}C$ with a SD of 0.6 and reveals a preceding major shift to lighter

values of around - 3.3‰ $\delta^{13}C$ with respect to the mean of the interval directly below. These negatively shifted values remain stable over the stratigraphic interval from 42.5 m to 59 m. At 59 meters, the carbon isotope signal starts continuously increasing to heavier compositions with a rapid shift at 63 m.

4.2.2 Isotope record – Interpretation

Clearly, the negatively shifted carbon isotope values of interval 3B represents carbon isotope values that are part of the PETM body. These negatively shifted isotope values continue in interval 3A until 63 m when a sudden and rapid shift towards heavier isotope compositions occur. This rapid decline is interpreted as the end of the PETM body and at the same time as the initiation of the recovery-phase. Besides the rapid shift in the isotope signal, some confidence is provided to label this upper part as the onset of the recovery because the sediments change in character, although this may result in circular reasoning.

The isotope compositions of interval 3C and 3D are evidently heavier in comparison to the isotopes values of the PETM body and are therefore interpreted as pre-PETM. However, interval 3C is already shifted by more than 2‰ on average compared to the mean of interval 3D and does not show typical pre-PETM baseline values. Therefore, interval 3C is interpreted and analysed as an individual group. The fluctuation in the isotope record as well as the allocation of the CIE onset is elaborately discussed in the discussion chapter (***5.1***).

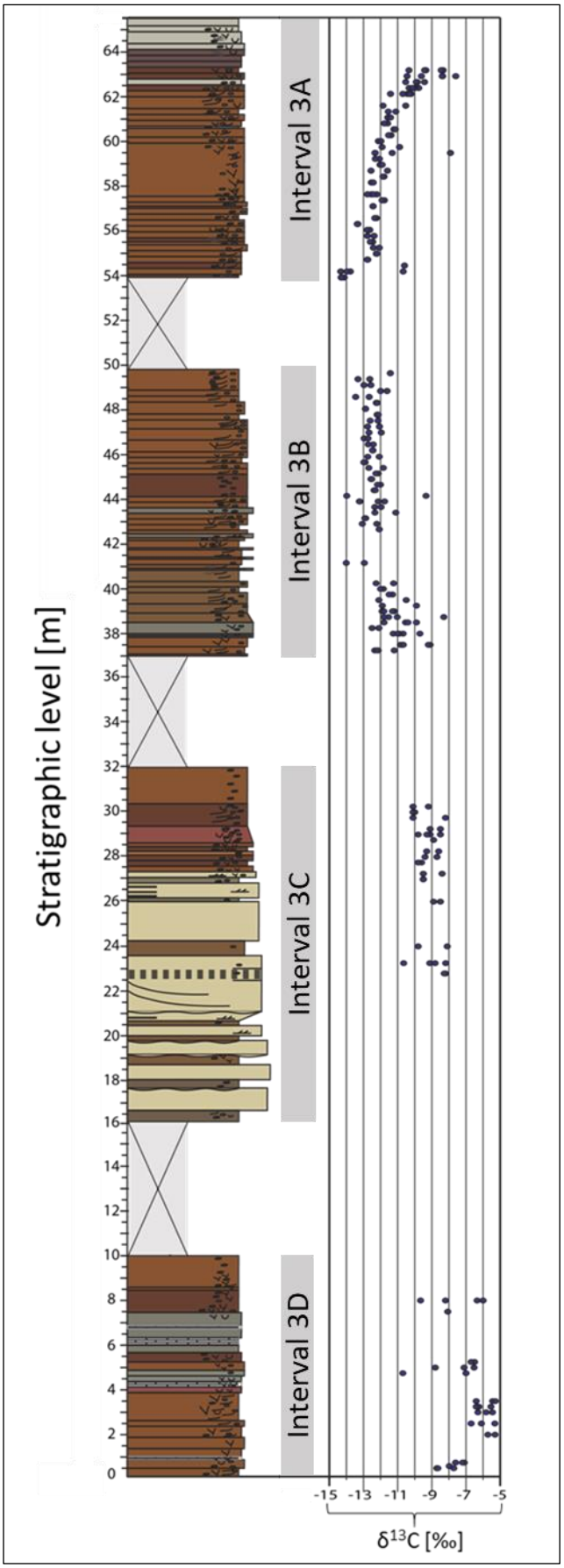

Figure 9. The $\delta^{13}C$ isotope signals of pedogenic carbonate of composite log of the Dongfeng section. The shaded boxes with a cross represent the stratigraphic gaps.

4.3 Grain size analysis

4.3.1 Grain size distribution

The results of the grain size analysis of the floodplain record are presented in the ensuing **Figures 10, 11, 12, 13, 14**. As described in the methodology section (***3.3***), the alluvial sandstone layers of the Dongfeng section between 16.5 and 27 m and the sandstone layers of the lower PETM body between 37 and 43 m are excluded from this grain size analysis. The distributions are based on 57 bins ranging from 0.12 µm to 2000 µm. The grain size analysis revealed mostly clay to silt dominated distributions (**Figure 10**). The most frequent particles were in the range of 3 - 10 µm. Most of these distributions show an almost symmetrical unimodal distribution with a small positive skewness. Some of the rock samples contain a larger amount of sand besides the clay and silt fraction and are characterised by a bimodal distribution. Grains with a size larger than 500 µm are completely absent in the measured paleosol samples.

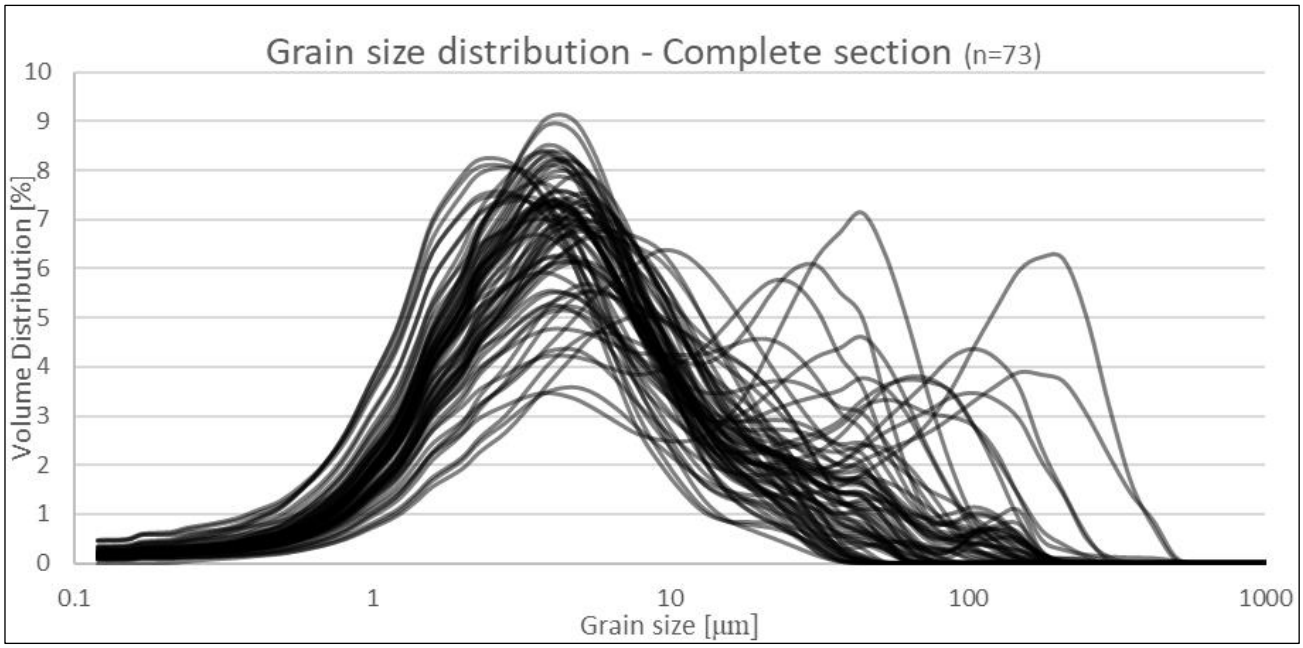

Figure 10. Grain size distribution of all 73 samples that were measured depicting the clay and silt dominated distributions.

The grain size distributions were separated according to the distinctive period of deposition (**Figure 11**). The pre-PETM phase contains all the samples from the base to 32 m but is subdivided into two groups. The first pre-PETM group (pre-PETM1) consists of the units from 0 to 10 m whereas the units from 16 to 32 m of the Dongfeng section belong to the pre-PETM2 group. The PETM body includes samples from 37 to 63 m and the recovery-phase from 63 m to the top (**Figure 14D**).

The distributions of the pre-PETM1 samples were of unimodal types whereas the pre-PETM2 consists of unimodal and bimodal distributions. Same as the pre-PETM2 samples consist the samples from the PETM body of bimodal and unimodal distributions. The recovery-phase is characterized only by unimodal distributions. The median, SD, kurtosis and skewness for the population of each analysis group are presented in **Table 2**.

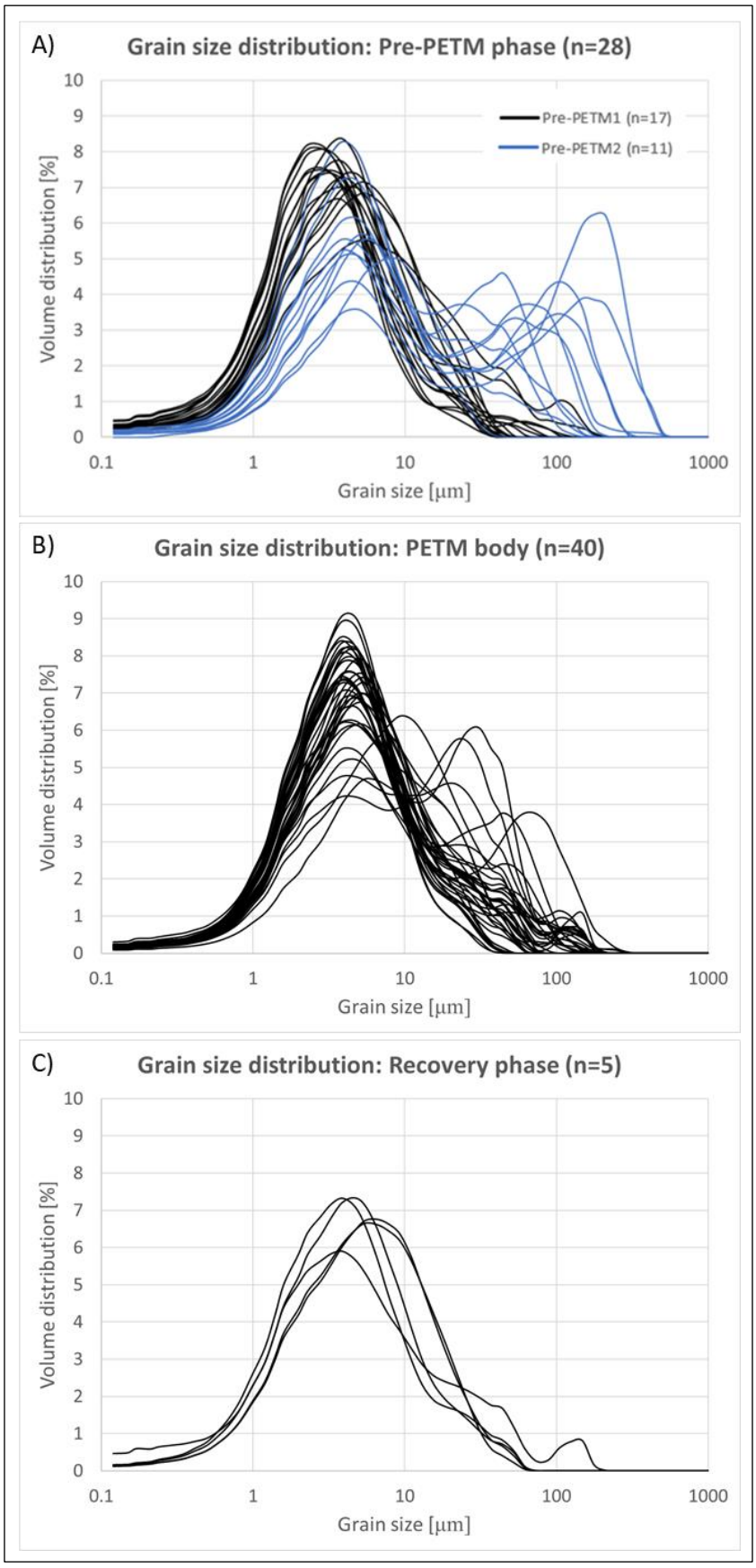

Figure 11. The grain size distributions for the distinctive period of deposition, namely pre-PETM (Panel A), PETM body (Panel B) and recovery-phase (Panel C). The number of measured samples (n) is mentioned in the title of each Panel.

Table 2: The statistical characteristics of the specific grain size populations.

Analysis group:	Median	SD	Kurtosis	Skewness
Pre-PETM1	3.30	1.50	3.43	0.18
Pre-PETM2	10.54	2.07	2.51	0.05
PETM Body	5.11	1.62	3.35	0.11
Recovery	4.12	1.58	3.22	0.17

The median of the pre-PETM2 distributions is on average the highest, followed by the median of the PETM body whereas the pre-PETM1 population has the lowest median. The SDs of pre-PETM2 and PETM body are the highest because of the abundance of bimodal distributions. The kurtosis is the highest in pre-PETM1 group revealing a frequent deviation in the clay fraction between 2 and 7 µm. This is also seen in the positive skew. The differences in clay, silt and sand content between the distinctive groups are summarized in **Figure 12**. In all the distinctive groups the clay fraction was the largest followed by the silt fraction and the sandy particles which represent the smallest fraction. The clay fraction accounts for roughly 52% to 85% whereas the silt fraction makes up roughly 17% to 34%. Pre-PETM1 samples have the highest clay fraction and the lowest silt and sand fraction of all the analysed groups. The pre-PETM1 group is inferred as the finest interval followed by the recovery-phase, PETM body and the pre-PETM2 group, which is the coarsest group in terms of grain size.

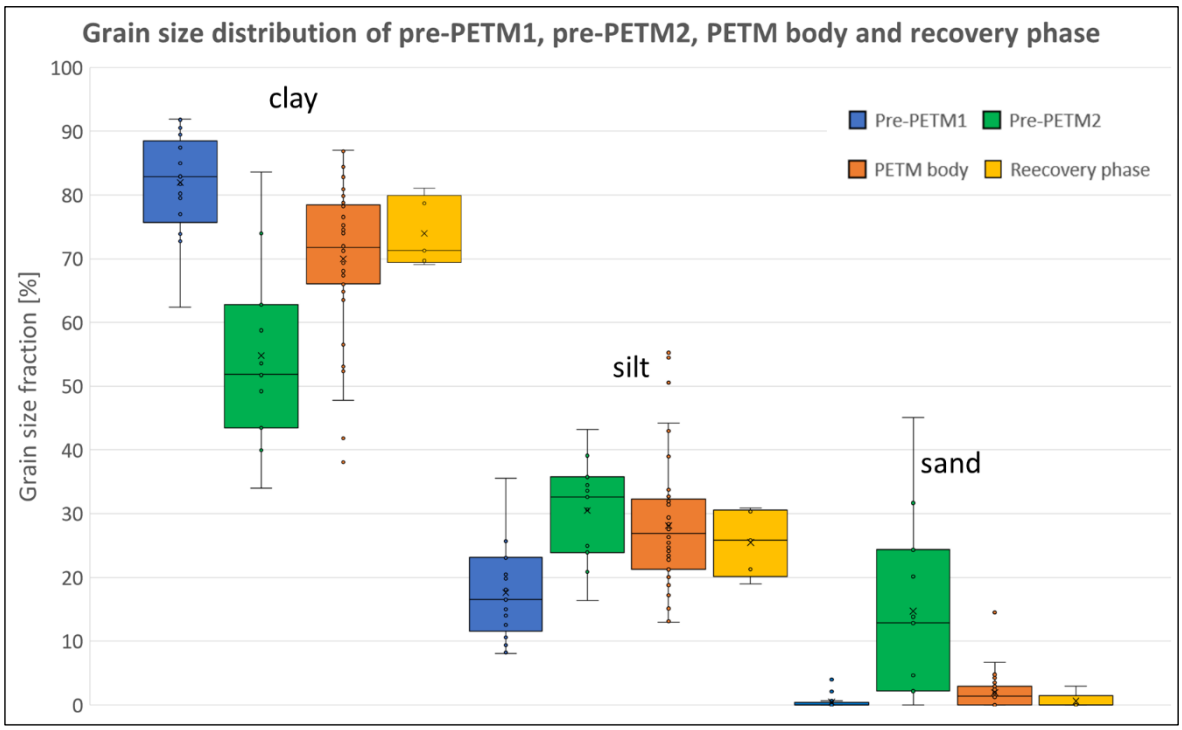

Figure 12. The grain size composition of the pre-PETM1 (n=17), pre-PETM2 (n=11), PETM body (n=40) and recovery (n=5) separated in clay (<8 µm), silt (8 - 63 µm) and sand (63 - 2000 µm) fraction. Note that the whiskers denote the lower- and upper fence, the edges of the boxes denote bounding quartiles whereas the transverse lines represent the median and the 'X' show the mean values.

Samples with abundant sandy particles were mostly found in the pre-PETM2 group at 27 - 32 m and subordinated in the PETM body (**Figure 14B**). By contrast, sandy particles in the pre-PETM1 group and in the recovery-phase are almost absent. The volumes of silt and clay fraction fluctuate over the whole interval and show a reverse path because of the rare abundance of sand.

4.3.2 End-member modelling

Applying statistics based on van Hateren et al. (2017) reveals a model with 4 end-members (EM) as the best solution to describe the grain size distributions. An increase in end-members would potentially enhance the level of distribution coverage but the improvement is only minor and mostly affects the distributions in the range of larger grain sizes (Supplementary material (***9.2***), **Figure 30**). The R-square plot presents a way of goodness-of-fit statistics (Prins et al., 2000). It clearly shows that the model represents grains up to 300 µm in a satisfying way whereas larger grain sizes are not well presented by the model (Supplementary material (***9.2***), **Figure 31**) which is insignificant for this study. The first two end-members EM1 and EM2 are unimodal distributions and lay in the clayish to fine silty range (**Figure 13C**). EM3 and EM4 are both bimodal distributions. EM4 has a coarser pronounced sandy distribution compared to EM3. The analysed stratigraphy of the Hengyang basin is dominated by EM1 and EM2. EM3 mostly occur in the PETM body and only slightly in pre-PETM1 and recovery-phase. EM4 occurs mostly between 27 to 32 m and subordinated in the intermediate and upper part of the PETM body (**Figures 13A & 14C**). The R-square plot indicate that the representation of the end-member is convincing except for the sandier interval between 27 and 32 meters where R^2 deviates from $R^2 = 1$ (**Figure 13B**).

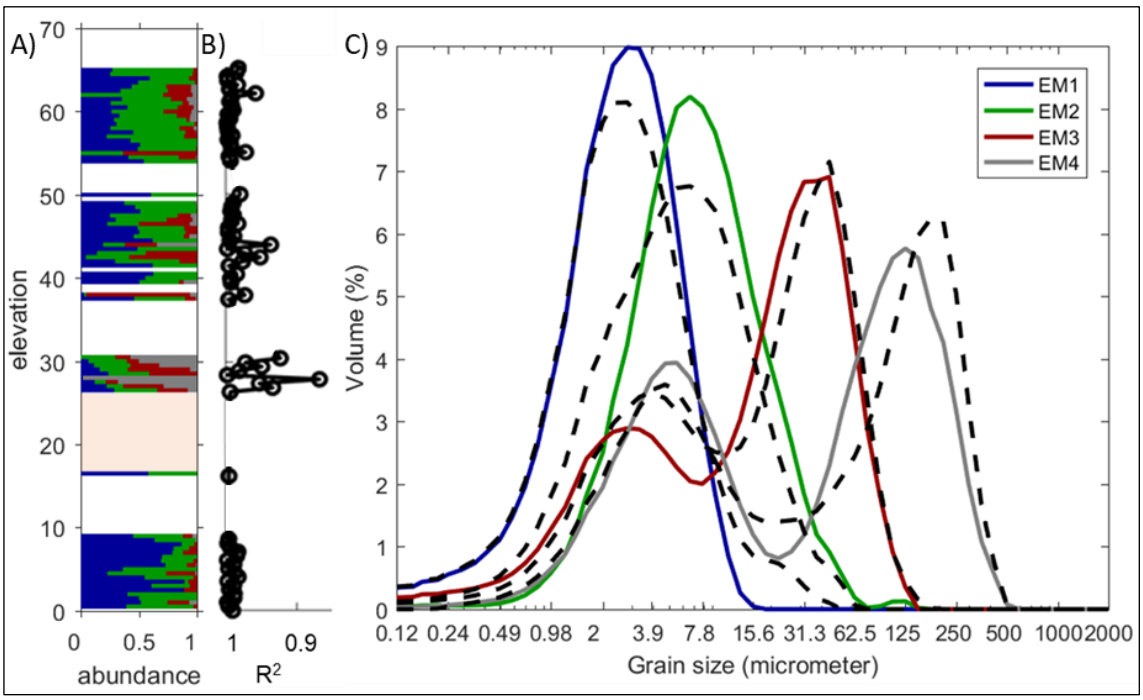

Figure 13. The end-member modelling abundance for the stratigraphic interval is presented. Panel A depicts the abundance of the four end-members which are illustrated in Panel C. The dashed lines in Panel C indicate the closest distribution of a sample to the end-member. Panel B shows the R^2 plot which represents the goodness-of-fit.

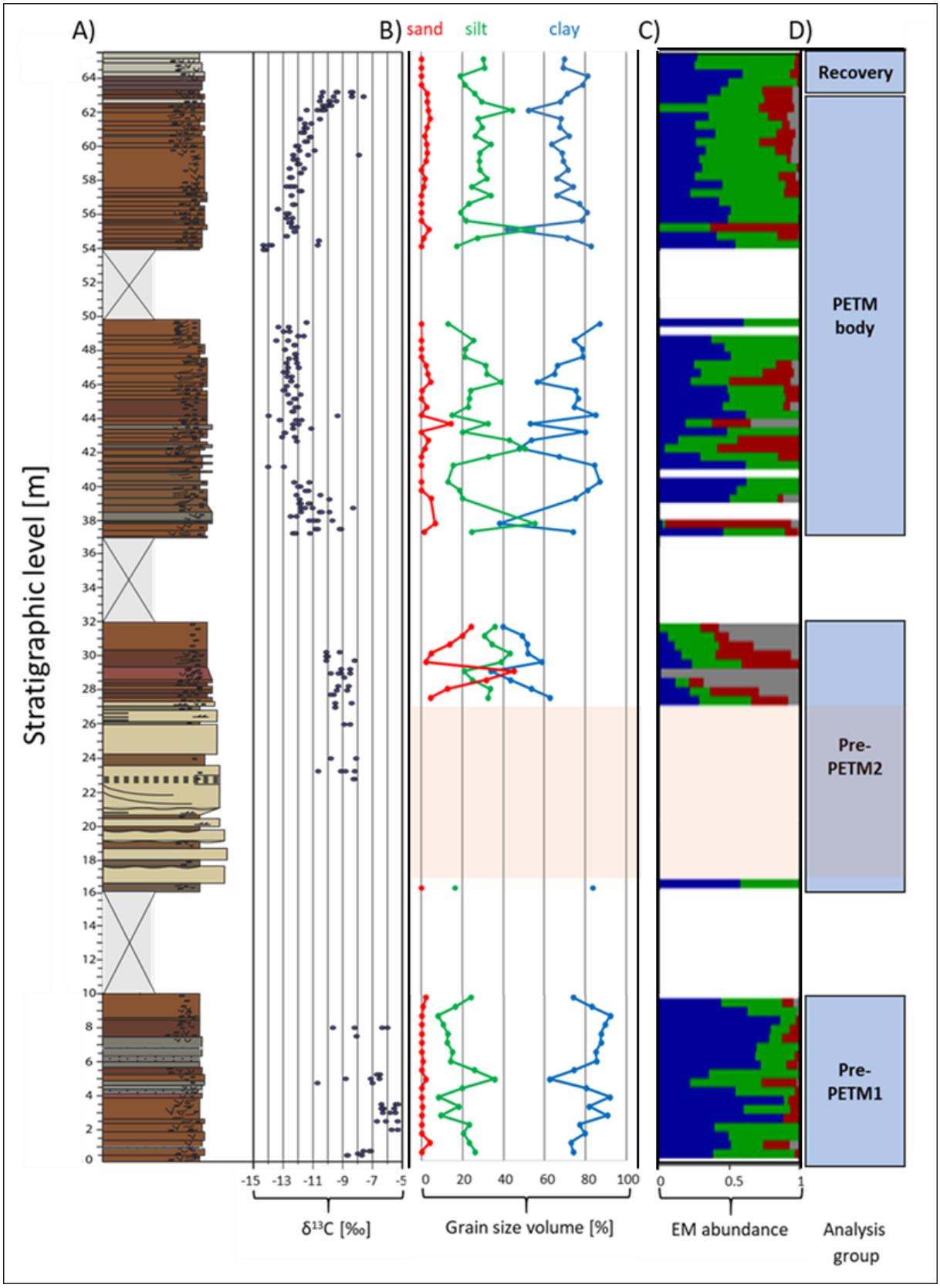

Figure 14: Panel B depicts the changes in volume of sand, silt and clay along the stratigraphic level with the corresponding isotope signal (Panel A). Panel C illustrates the end-member abundance according to **Figure 13**. The distinctive analysis groups are presented in Panel D.

4.4 Clay mineralogy assemblage

The clay mineralogy analysis was conducted by Dr. Chaowen Wang from China University of Geosciences, Wuhan, China. Samples were taken from interval 3D representing the pre-PETM clay composition and from interval 3B with a clay composition corresponding to the PETM body. The clay composition of the pre-PETM units is dominated by smectite with around 28% and mixed layer illite-smectite (I-Sm) around 30% (**Figure 15**). Pure illite has an average of around 17%, whereas mixed-layer kaolinite-smectite (K-Sm) constitutes around 20%. Kaolinite and chlorite occur only subordinately.

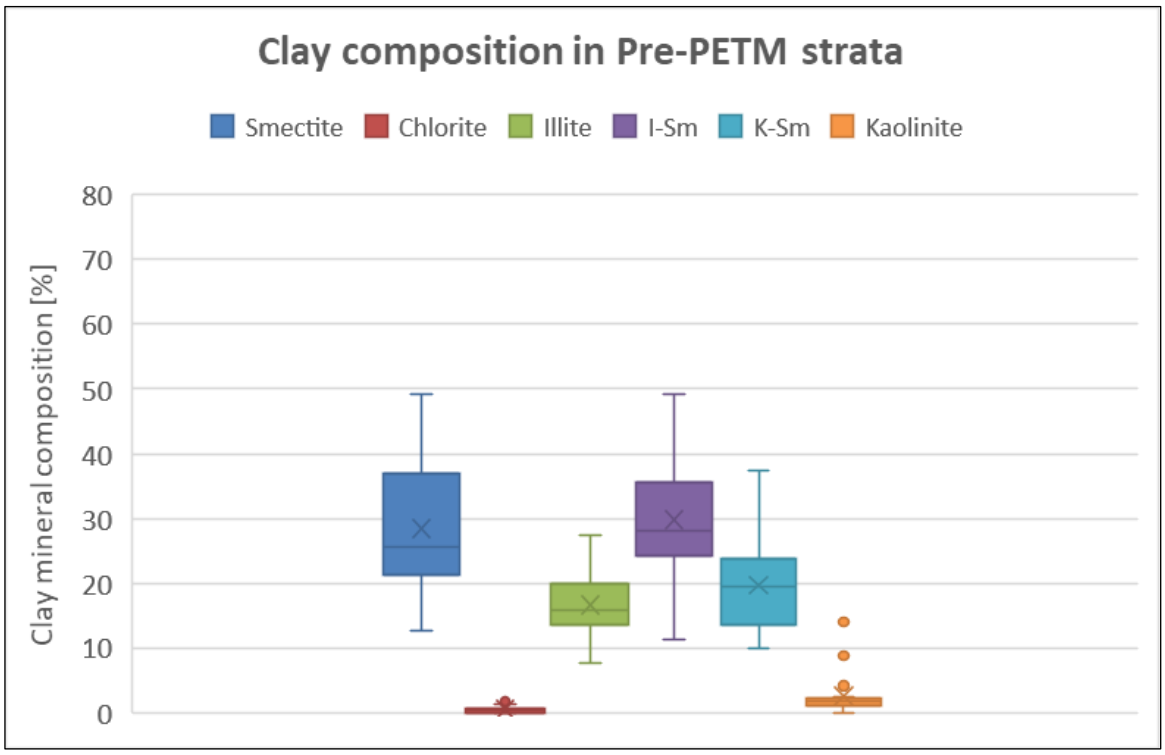

Figure 15. The summarized clay composition of the pre-PETM strata of interval 3D for the distinctive clay minerals. Note that the whiskers denote the lower- and upper fence, the edges of the boxes denote bounding quartiles whereas the transverse lines represent the median and the 'X' show the mean values. The circles indicate outliers. (The results of the clay analysis are owned by Dr. Chaowen Wang, China University of Geosciences, Wuhan.)

The clay mineral composition of the units from the PETM body are presented in **Figure 16**. Smectite is the most abundant clay mineral, on average, with a content of around 47%. Mixed-layer I-Sm is at 27% the second largest fraction. Illite constitutes 11% whereas kaolinite and chlorite rarely occur. The difference plot in **Figure 17** depicts the difference in clay composition between the PETM and pre-PETM units including the standard error range. Smectite increases by around 20% whereas illite decreases by around - 6% in the PETM units compared to the pre-PETM units. Besides the illite fraction, I-Sm and K-Sm decreases in the PETM units around - 3% and - 10%, respectively. The content of kaolinite and chlorite remains almost constant and no shift was observed. The calculated K/Sm ratio of the pre-PETM is 0.09 and decreases to 0.04 in the PETM body.

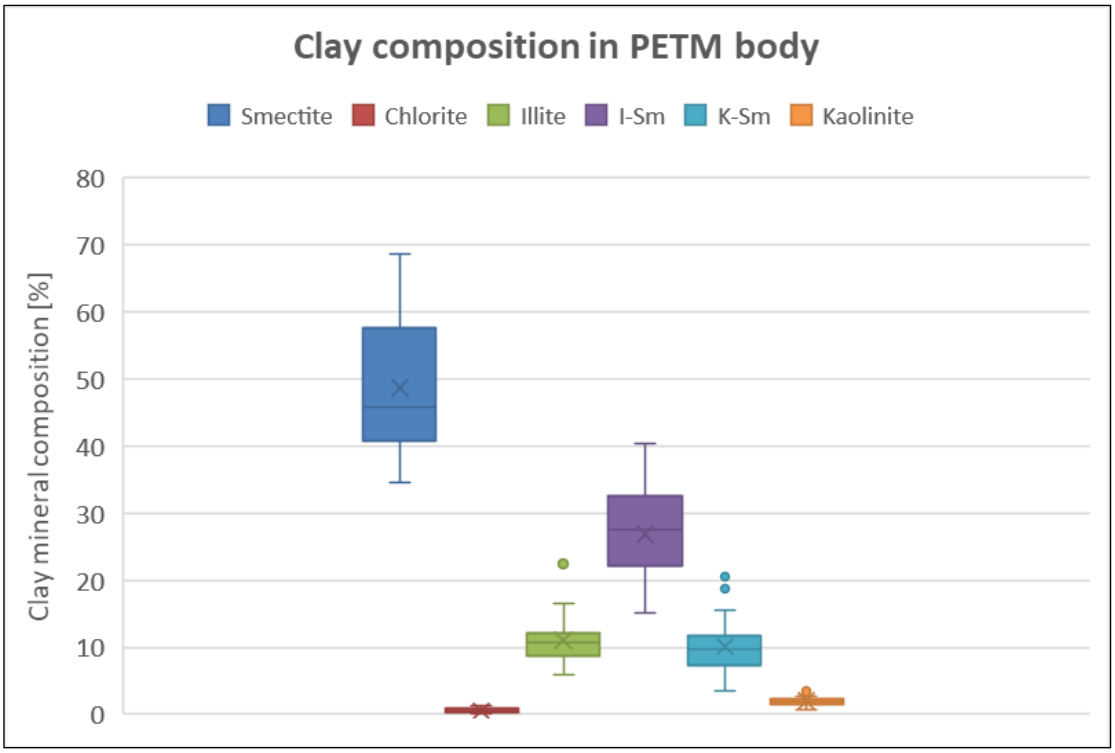

Figure 16. The summarized clay mineral composition of the PETM body collected from interval 3B. Note that the whiskers denote the lower- and upper fence, the edges of the boxes denote bounding quartiles whereas the transverse lines represent the median and the 'X' show the mean values. The circles indicate outliers. (The results of the clay analysis are owned by Dr. Chaowen Wang, China University of Geosciences, Wuhan.)

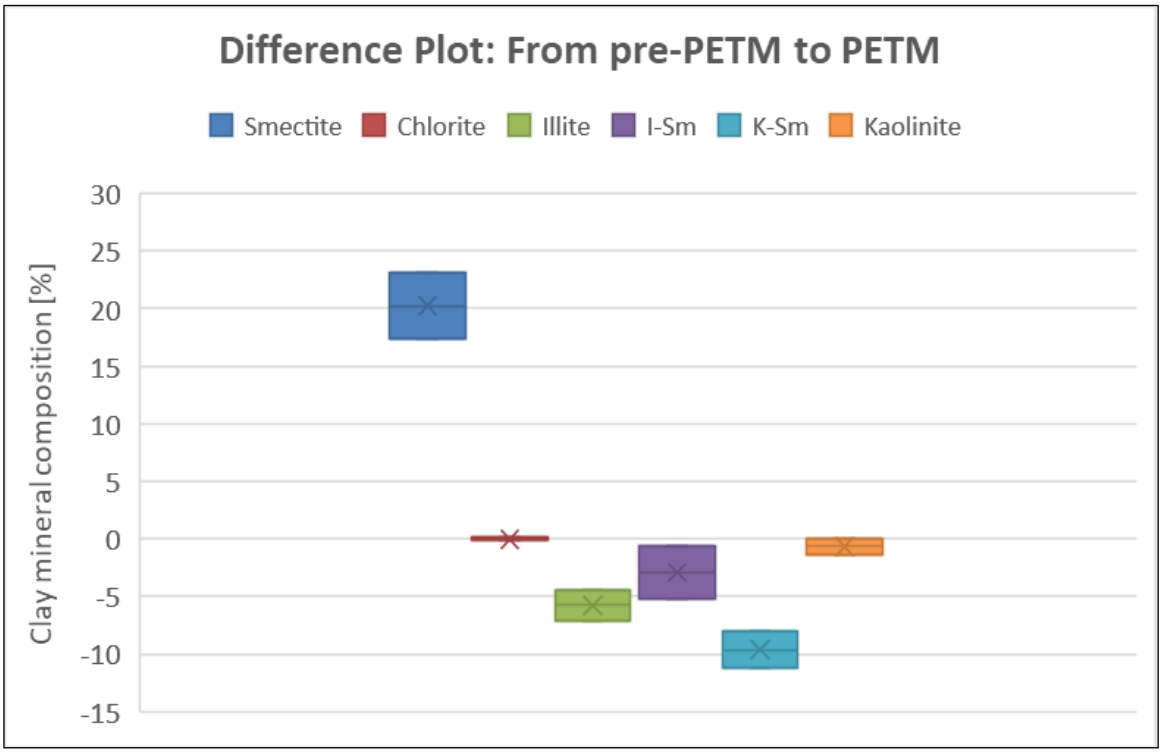

Figure 17. The difference plot depicts the difference in the distinctive clay minerals between the PETM units and the pre-PETM units. Negative values correspond to a decrease from pre-PETM to PETM. (The results of the clay analysis are owned by Dr. Chaowen Wang, China University of Geosciences, Wuhan.)

4.4 Sandstone mineralogy and sediment maturity

4.4.1 Pre-PETM sandstones

The fabric of the pre-PETM sandstones consists of subarkose, sublitharenite, lithic arkose and feldspathic litharenite. Quartz minerals dominate the framework but feldspars (~ 20% - 40%) and other rock fragments are abundant (**Figure 18**). The quartz minerals are mostly mono-crystalline and subordinated poly-crystalline. The feldspars are altered and therefore detectable in the plane polarized light. Some orthoclase minerals are twined but most are untwined. Micas often occur in type of larger muscovite crystals which are sometimes deformed and fractionised. Biotite only occurs in minor amounts. The pre-PETM samples are regarded as mineralogically moderately mature because of the alteration and the abundance of feldspars and other fragments. The grains have a size of medium to coarse and are very angular with variable sphericity. Some grains were identified as subrounded but the angularity is the dominant shape. The samples were inferred as sedimentarily immature. The grains are poorly to moderately sorted. The moderate porosity is filled with a clay rich matrix with abundant iron-oxide minerals. The grains are surrounded by iron oxide coatings (**Figure 19**), which are mostly built of hematite.

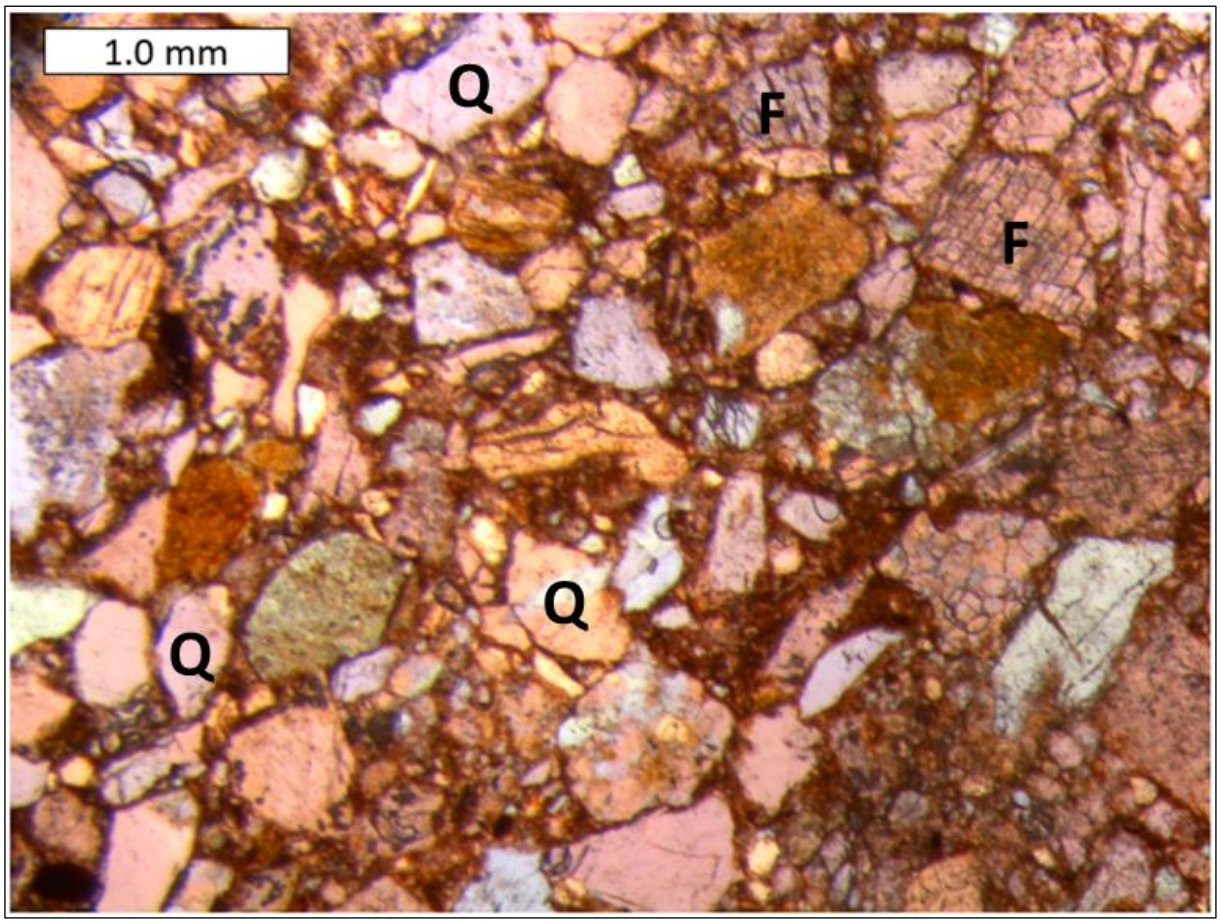

Figure 18. The thin section of a typical pre-PETM sample (collected at the stratigraphic level of 22 m). The medium to coarse grained sandstone contains abundant feldspars (F), besides the mostly monocrystalline quartz (Q) minerals. The framework is supported by a clay and iron oxide rich matrix.

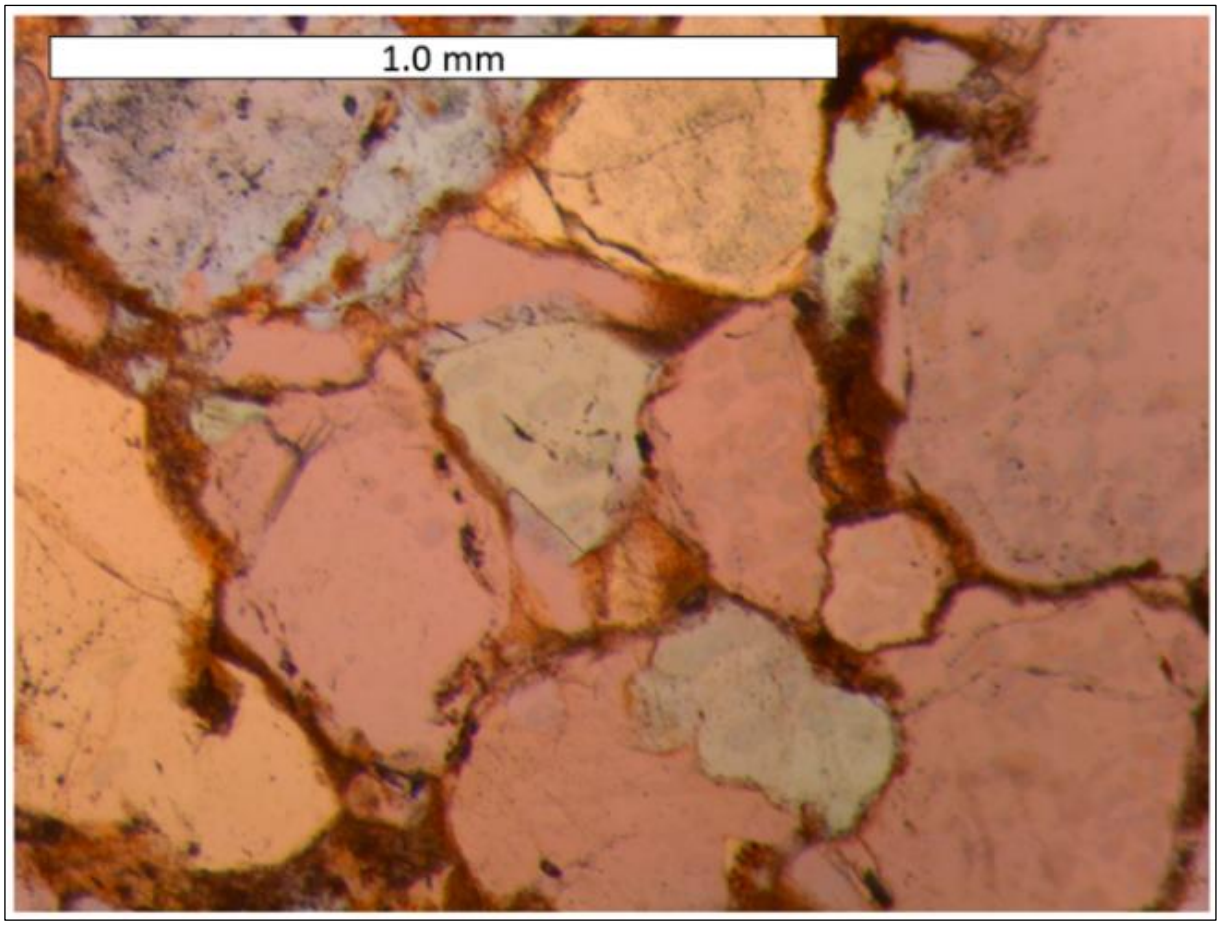

Figure 19. Thin section of a pre-PETM sample (collected at stratigraphic level of 17 m) under 10x magnification. The quartz grains are coated with an iron oxide rim and a clay rich matrix.

4.4.2 PETM sandstones

The fabric of the PETM sandstone samples which occur between 37 and 43 m are typical of subarkose and sublitharenite class which are characterized by the dominance of quartz with subordinated feldspars and other rock fragments. The grains and the moderate existing porosity are filled with a clay rich matrix. Grain-to-grain contacts are common, but a matrix supported framework dominates the argillaceous sandstones. The matrix also consists of iron oxides, mostly hematite. The grains are of very fine to fine size and they are subangular to angular with variable sphericity (**Figure 20**). Larger grains tend to be more angular than smaller ones. Occasionally, elongated particles are found which do not exhibit any evidences of orientation. The grains are moderately to well sorted. The PETM sandstone samples are regarded as texturally immature because of the angular grain shapes. In contrast to the texture, the sandstones are mineralogically mature. Mono-crystalline quartz minerals dominate the framework with subordinated poly-crystalline quartz and variable amounts (~ 10% - 25%) of feldspars, mostly orthoclase. Micas occur as minor constituent (~ 3%) in all the samples and are mostly elongated, platy muscovite and minor biotite.

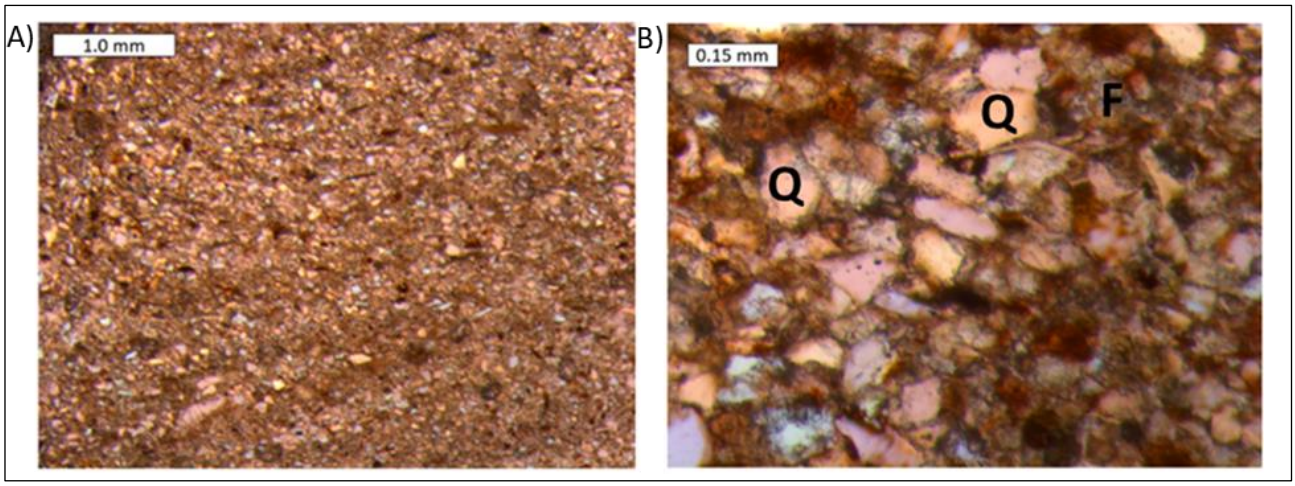

Figure 20. Panel A shows the thin section of a typical PETM sandstone sample (collected at the stratigraphic level of 38.25 m.) The very fine-grained sandstone mainly consists of monocrystalline quartz minerals within a clay rich matrix. Panel B depicts the same sample under 10 times magnification.

4.4.1 Diagenetic imprints

Regarding the burial history of the pre-PETM and PETM samples some evidences of low stage diagenesis and compaction was found. Elongated and physically weak micas mostly muscovite were deformed around quartz or feldspar grains indicating pressure impact through overburden. Furthermore, convex-concave structures were identified in several pre-PETM and some PETM samples (**Figure 21**). These convex-concave structures of quartz grains indicate first stage of pressure solution where silica is removed from the site through dissolution by pore fluids or precipitate as quartz cement (Houseknecht, 1984). However, no quartz cementation was found in the samples, which support a removal of the dissolved silica by pore fluids.

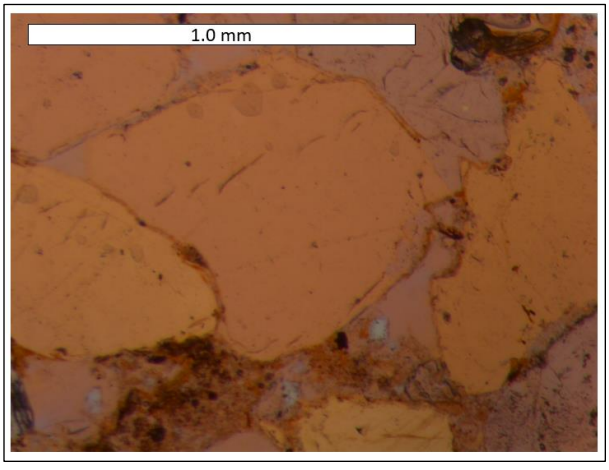

Figure 21. The thin section depicts the first stage of pressure solution in a pre-PETM sandstone sample, which was collected at the stratigraphic level of 19.5 m. The quartz grains press together whereas one grain intrude into the other and left behind a concavo-convex structure.

The results of the conducted measurements and analyses depicted clear differences between the distinctive phase of depositions. **Figure 22** illustrates the summary of all the results of the multi-proxy analysis of the Dongfeng section in the Hengyang basin, which are allocated according to their stratigraphic position.

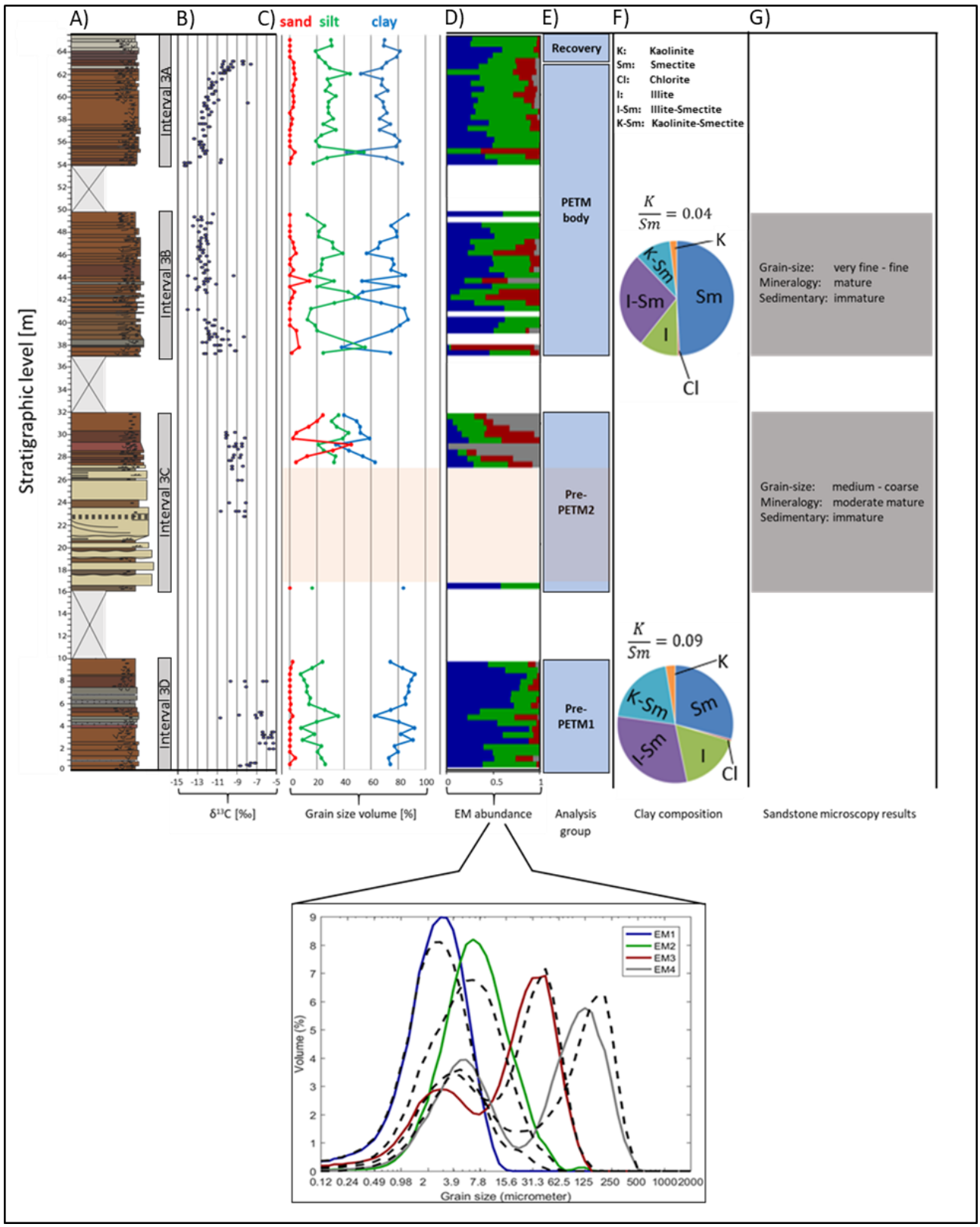

Figure 22. The summarized results of the multi-proxy analysis of the Dongfeng section in the Hengyang basin, China. Panel A represents the lithological composite log with the corresponding isotope signal (Panel B). The alteration in grain size are depicted in Panel C with the abundance of the modelled end-member distributions in Panel D. Panel E shows the stratigraphic range of the analysed groups. The clay compositions are presented in Panel F whereas the results of the microscopic analysis are given in Panel G.

4.5 Catchment, Transport, Deposition – Modelling

4.5.1 PETM-Model - climate response

Figures 23, 24, 35, 26 represent the simulated climate and sedimentary response to the PETM based on the input parameters of **Table 1**. **Figure 23B** reflects the calculated precipitation over the investigated period by means of the climate routines of the PaCMod 1D catchment model (see Methodology section (***3.6***)) (Forzoni, 2014). The precipitation trails the path of the temperature curve and emphasizes the strong linkage between the temperature input and the calculated precipitation. The precipitation sharply increases from 600 mm/year to almost 900 mm/year. The precipitation remains stable during the increased temperature period of 30˚C during the 100 ky PETM body. As soon as the temperature starts decreasing from 30˚C to 24˚C, the precipitation also decreases to 750 mm/year.

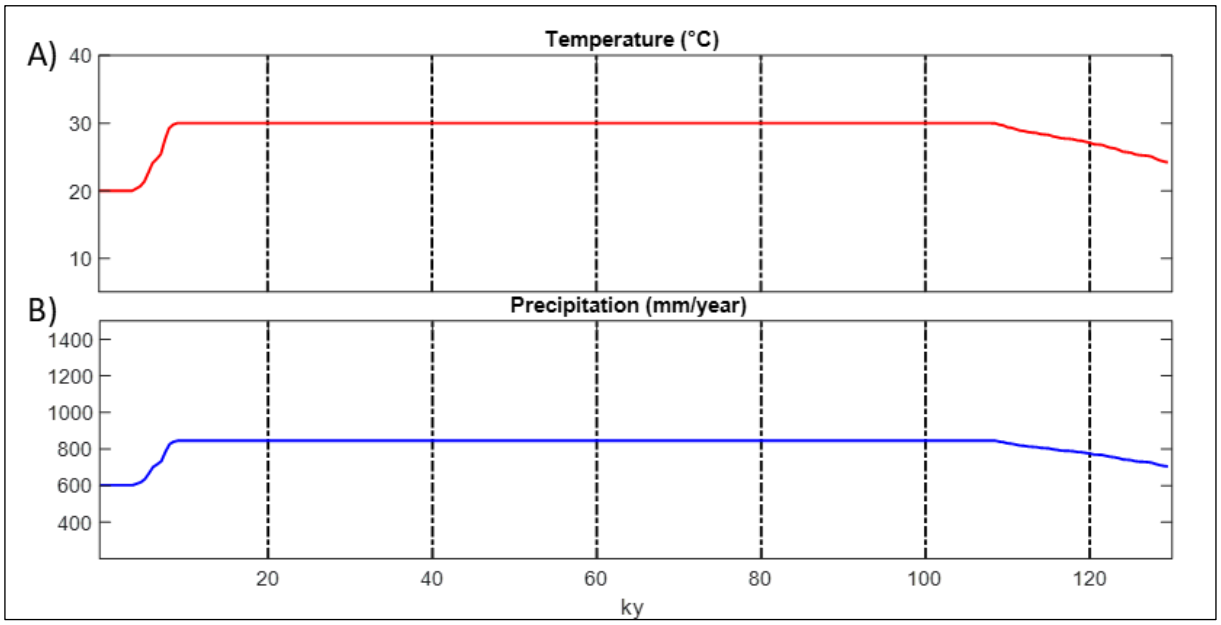

Figure 23. Panel A depicts the temperature curve which was used as input for the simulated climate – catchment model in PaCMod according to **Figure 4**. The resulting annual precipitation in mm/year is depicted in Panel B.

In addition to precipitation, the evaporation curve follows the trend of the temperature input (**Figure 24B**). Precipitation reaches daily values of around 5 mm whereas evaporation reaches 3 mm/day during the PETM body when temperature rose to 30 ˚C. The resulting net precipitation sums up to 2 mm/day during the PETM body. The red line in the precipitation plot (**Figure 24A**) reflects the amount of snow melt which contributes to the generated water discharge. However, little snow is expected and therefore the snow coefficient was set to 0.01 which leads to a snow melt of almost zero. Generally, precipitation exceeds evaporation and the net resulting precipitation is positive which causes the runoff and infiltration in the presented water discharge curve in **Figure 25A**.

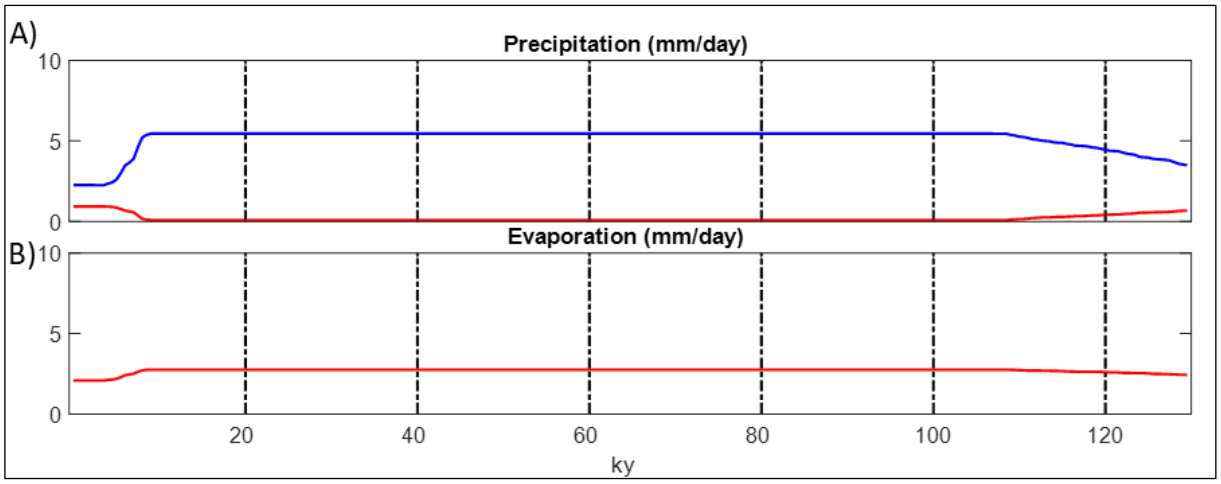

Figure 24. The simulated daily rate of precipitation (blue), snow melt (red; Panel A) and evaporation (red; Panel B). The amount of snow melt is zero over the almost entire period of the PETM. The net precipitation is positive during the PETM.

4.5.2 PETM-Model - sedimentary response

The water discharge of the river system fluctuates strongly through the entire period (**Figure 25A**). The average water discharge follows the same trend as the precipitation curves increasing from around 200 m^3/s to almost 300 m^3/s where it remains mostly stable. The bedload transport sharply increases with the rapid temperature rise during the onset of the PETM. The transported average bedload which is shown using the black line increases by around 170% compared to the base bedload transport in the first 5 ky. The bedload peaks slightly fluctuate in all the distinctive phases (**Figure 25B**). In contrast to the bedload peaks, the suspended load peaks fluctuate strongly during the entire interval (**Figure 25C**) while the average suspended load curve shows the same trend. The average suspended load sharply increases by more than 300% compared to the base values prior to the temperature increase. At 110 ky, when the temperature starts to decrease, the suspended load fraction also decreases. However, the suspended load exceeds the bedload at all distinctive phases.

The bedload supply and the transport capacity of the river show an almost similar trend and resembles the water discharge profile and the potential bedload curve (**Figure 26A**). The transport capacity continuously fluctuates around 0.006 m^3/s during the increased temperature of the PETM body whereas the bedload supply remains almost stable at slightly lower values. The transport capacity exceeds the bedload supply over the entire period. In other words, if there would be more sand available in the regolith of the catchment, the river could carry an even higher fraction of sandy particles.

The volume of confined floodplain reservoir shows a rapid increase when the temperature rise occurred and remains stable before it starts decreasing during the recovery-phase (**Figure 26B**). The confined floodplain reservoir represents the temporary sediment accumulation in floodplains and acts as catchment in lower reaches. The temporary deposition of sediments in confined floodplains is minor compared to the amount of transported material.

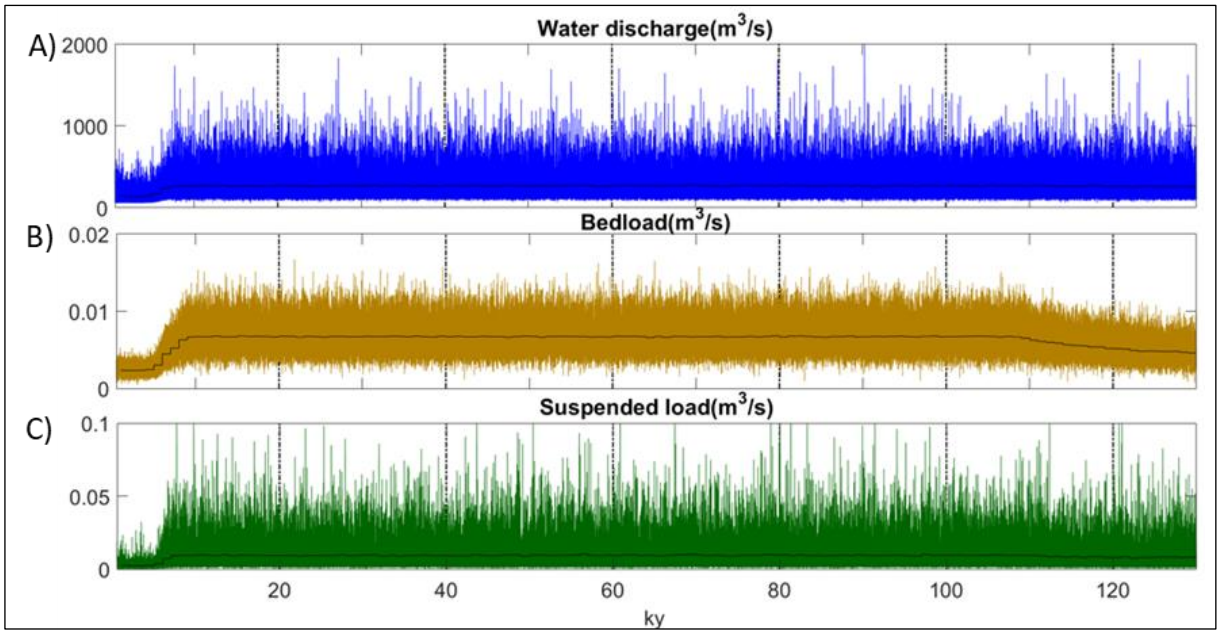

Figure 25. Panel A depicts the water discharge of the river system with the peak values (blue) and the average value (black). Panel B shows the peaks of the bedload transport (yellow-brown) and the average bedload transport (black). Panel C illustrates the suspended load peaks (green) and the average suspended load (black) of the river system.

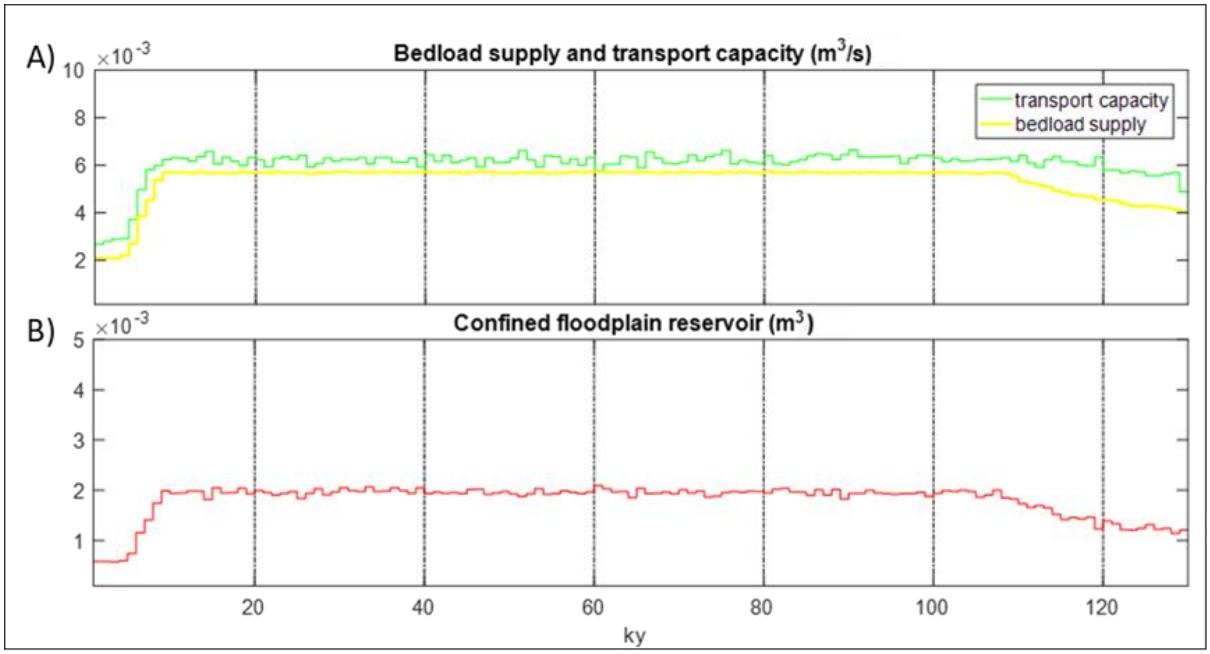

Figure 26. The bedload supply (yellow) and the transport capacity (green) are depicted in Panel A. Panel B shows the emergence of downstream sediment depositions as confined floodplain reservoirs.

The changes in erosion rate (**Figure 27**) in the catchment area over the investigated period were calculated with the river system response model routines (Forzoni, 2014) based on the precipitation output of the climate catchment model (**Figure 23B**) and the parameters of **Table 1**. The erosion rate is around 12.5 mm/ky before the sudden temperature increase occurred. The erosion rate reacts to the temperature increase at 5 ky with a sudden rise followed by a rapid decrease with a subsequent increase to 18 mm/ky. The erosion rate remains on

an increased level for the entire PETM body. When the temperature started decreasing, the erosion rate fell almost exponentially and reached values slightly below the initial erosion rate at time 0 ky. Subsequently, the erosion rate slightly increases and ends up on the same erosion rate as in the beginning.

The transported bedload in the river system divided into average bedload transport and peak bedload show a slow increase at 5 ky followed by a very sharp increase at 10 ky (**Figure 28A**). The average bedload transport increases from 0.4 x 10^{-3} m^3/s to 0.5 x 10^{-3} m^3/s. The suspended load fraction is also presented in peak load and average suspended load. In contrast to the bedload curve the suspended load increases rapidly with the temperature onset at 5 ky (**Figure 28B**). When the temperature started falling at 110 ky, the suspended load decreases as well. This decrease differs between the peak curve and the average curve. The peak curve decreases even further than the initial value at time 0 ky before it starts increasing again towards the initial value. The shape of the bedload and suspended load curves equals the presented results from the climate catchment model (**Figure 25**) except for the quantities.

The simulated sediment storage in the lower reaches of the system where sediment is deposited in floodplain environments, fluctuates over the entire simulation period (**Figure 28C**). The fluctuation shows that an increase in sediment storage is always followed by a decrease. The transition between the increase and decrease is short and changes immediately from one extreme to the other. However, an increase in sediment storage as a response to the temperature increase is still visible in the curve. The fluctuations of the sediment storage tend to lower values after the temperature starts decreasing at 110 ky.

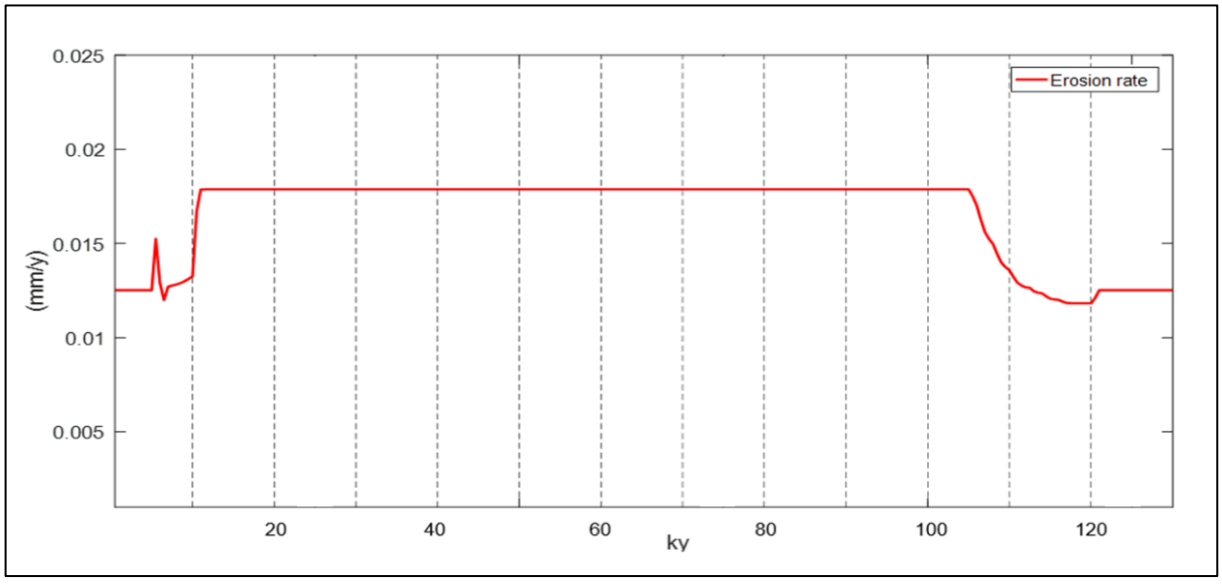

Figure 27. The computed erosion rate in the catchment according to the input parameters of Table 1 and the computed precipitation input of **Figure 23B.**

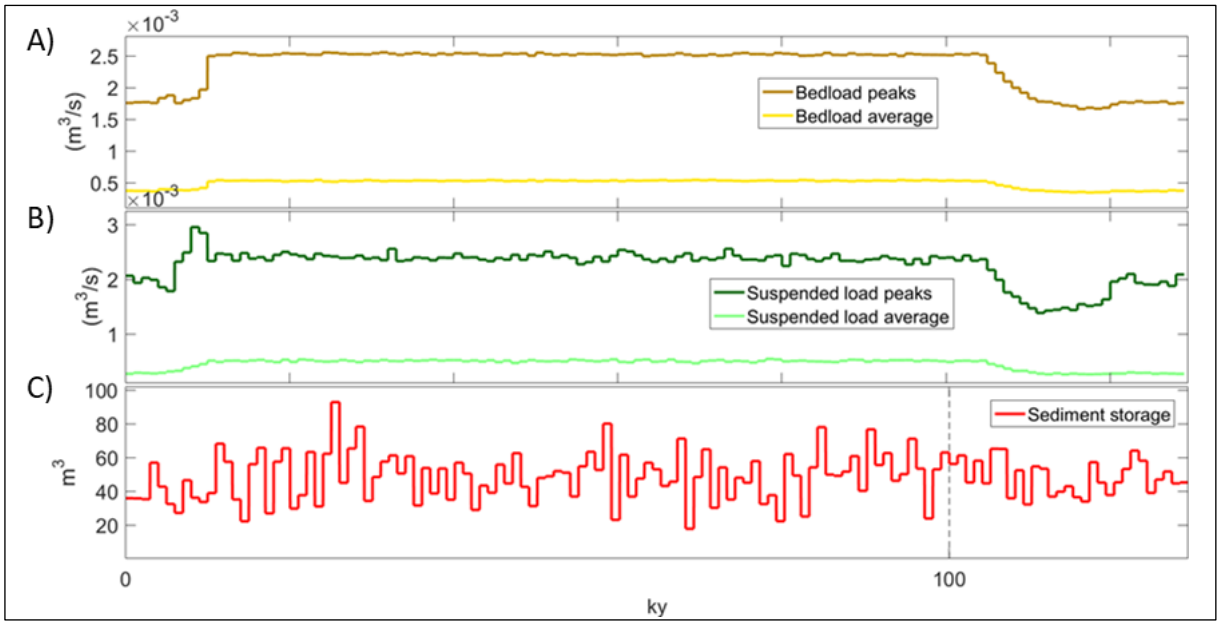

Figure 28. The resulting semi-quantitative numbers for the bedload (Panel A) and suspended load (Panel B) transport of the Golo river system response model in PaCMod. The sediment storage is presented in Panel C. The results are based on the input parameters of Table 1 and the precipitation input of **Figure 23B.**

The results of the climatic and sedimentary response analysis by the PaCMod simulation models can be summarized by the following findings:

- The precipitation and the evaporation increased simultaneously with the temperature increase during the PETM, resulting in a positive net precipitation
- The water discharge of the river system followed the trend of the precipitation curve and led to an increased water discharge during the PETM body.
- The transported bedload and suspended load increased because of the temperature and precipitation increase during the PETM. The suspended load responded rapidly to the temperature onset, whereas the bedload fraction showed a sharp response with a short time delay of around 5 ky.
- The erosion rate in the catchment area increased because of the increased temperatures during the PETM body.
- The sediment storage in the lower reaches of the catchment strongly fluctuates but tends to increase during the PETM.

5. Discussion

5.1 Isotope excursion and CIE onset

In the newly generated isotope series, a carbon isotope excursion with the three distinctive phases was found which is related to the PETM, the pre-onset PETM body and recovery. The pattern of the only existing isotope measurements from section 3 in the Hengyang basin (Bowen et al., 2002) resembles the developed isotope results in this study. However, the resolution of the isotope series presented by Bowen et al. (2002) was low. They neither detected a clear PETM body nor the recovery. Additionally, the determination of the CIE onset was based on an insufficient number of isotope measurements (Bowen et al., 2002; Ting et al., 2003; Wang et al., 2011) such that the allocation was only speculative and inaccurate.

The newly conducted high-resolution isotope signal clearly identified the PETM body in interval 3B and 3A. The PETM body is terminated by the onset of the recovery-phase at 63 m found through the rapid shift towards heavier isotope compositions and a change in sediment character. This rapid shift in isotope compositions, which marks the initiation of the recovery-phase, resembles the isotope signal of the Bighorn basin where the same rapid shift occurs (Bowen et al., 2001; Van der Meulen, 2015). The carbon isotope signal of the lowest units of what is regarded as PETM body at 37 - 39 m shows a more dispersed signal with excursion values around - 12‰ going together with heavier carbon isotopes down to - 8‰ $\delta^{13}C$ (**Figure 22**). That differs from the overlying units of the PETM body showing very stable carbon isotopes. Such a dispersed signal was also found in the PETM CIE body in the Tremp Basin in Spain, just above the Claret Conglomerate (Anema, 2017). In addition, the isotope signal of the PETM body in the Bighorn basin, which is characterized by a continuous decline towards heavier isotope compositions starting from the base of the body and ending when the rapid recovery shift occurs, is also interrupted by a sudden excursion to heavier isotopes in the lower half of the PETM body (Van der Meulen, 2015; Van der Meulen et al., 2018). Whether these dispersed and heavier isotope signal excursions are analogous depends on the timing of the occurrence of these events and can only be determined with an exact age model of the Hengyang basin together with the accurate allocation of the CIE onset.

In the Dongfeng section, the averaged isotope composition of the PETM body is shifted around 3.3‰ towards lighter isotopic composition compared to the mean isotope signal between 22 m and 30.5 m, which is interpreted as pre-PETM signal. It is concluded that the main CIE onset occur above the highest isotope results of interval 3C or in the stratigraphic gap between 32 and 37 m. Thus, the CIE onset is placed between 30.5 m and 37 m.

Bowen et al. (2002) established an age model of the Hengyang Paleocene strata based on magnetostratigraphy. By means of this age model, a pre-onset sedimentation rate of around 0.22 m/ky was determined. A 104 ky duration from the base of the onset to the end of the PETM body was established in the Bighorn basin by Van der Meulen et al. (2018). Assuming constant sedimentation rates in the Hengyang basin across this greenhouse warming event, this duration would have resulted in a 22.9 m thick PETM body including the onset. With the beginning of the recovery-phase at 63 m, the CIE onset would roughly occur at 40 m. This means that the CIE onset would lie 3 m above the stratigraphic gap in which the CIE onset is envisioned. Only slightly higher

sedimentation rates are needed to place the PETM onset within the stratigraphic gap and no strong arguments for largely increased sedimentation rates in the Hengyang basin across the PETM were found.

However, the pre-PETM sedimentation rates are averages over the whole interval between the PETM and the top of magnetochron C25n. Therefore, the age model used is fraught with uncertainties. An exact timing is because of the 6.5 m wide range of the possible CIE onset location, which corresponds to a rough time range of 30 ky, unfeasible and thus further clarification of potential correlations of the dispersed signals in the lower PETM body between the Hengyang, Bighorn, and Tremp basin remains uncertain.

The averaged isotope signal (- 9.1‰ $\delta^{13}C$) of interval 3C between 22 m and 30.5 m is characterized through a relative low SD 0.7 which emphasizes the high precision of the measured isotope compositions in contrast to the basal interval (3D) of the Dongfeng section with an SD of 1.3. However, the isotope signals of interval 3C are already shifted more than 2‰ $\delta^{13}C$ to lighter isotopic values in comparison with the basal interval 3D and must be regarded as pre-onset excursion values. Therefore, the samples of interval 3C were separated from the basal pre-PETM interval 3D and analysed as an individual group. Pre-onset isotope excursion (POE) values were also identified in the Bighorn basin which occurred roughly 10 ky, 20 ky, 40 ky and 60 ky, respectively, before the main CIE onset (Meijer, 2015). However, in the isotope signal of the Dongfeng section all the values of interval 3C are shifted and less dispersed so that neither distinguishable excursions nor a trend within the interval can be identified. They clearly differ from the detected POEs in the Bighorn basin.

The isotope signals of interval 3D are highly dispersed around the mean of - 6.9‰ $\delta^{13}C$ and were interpreted as pre-PETM isotope values. These dispersions were most likely the consequence of a mixing of carbonate material of lacustrine and pedogenic origin, as lacustrine carbonate depositions dominate interval 3D. Other differences which were generally suggested as influential on the isotopic signal of pedogenic carbonates are the type of vegetation (Smith et al., 2007; Diefendorf et al., 2010), the formation depth (Cerling, 1991), infiltration of isotopically different water (Cerling and Quade, 1993), precipitation (Wynn, 2007), diagenesis (Swart, 2015) and a combination of soil CO_2 and meteoric pore water (Cerling, 1984). These are though not the likely reason for the dispersion because they would have occurred in all the intervals. However, the wide dispersions of isotope signals were, aside from the lower part of the PETM body, only found in interval 3D which was interpreted to be lacustrine deposits. Hence, it is suggested that the lacustrine environment caused the detected dispersion in interval 3D.

5.2 Palustrine deposits under temperate pre-PETM climate conditions

The paleosols from the base to 10 m in stratigraphic level were identified as layers of pre-PETM age. This interval is characterized by red beds with an intermediate part consisting of olive-greyish units alternating with limestone layers. Preserved features in the limestone and olive-greyish units such as burrows, gastropods and ostracods reveal a lacustrine deposition with a weak pedogenetic imprint. Fluctuation of the water table and subaerial exposure of these lacustrine sediments initiate pedogenesis forming a so called palustrine limestone (Freytet and Verrecchia, 2002). The greyish colour is an indication of reduced environmental conditions (Cole

and Picard, 1981; Kraus and Riggins, 2007) which is also seen in the rarity of bioturbation indicating suboxic to anoxic conditions (Ekdale and Mason, 1988). Therefore, it is interpreted that the limestone and olive-greyish layers were deposited under reduced conditions in a shallow perennial lake which is vulnerable to water table fluctuation to allow soil development. The absence of evaporitic deposits in these lacustrine layers indicates a freshwater or oligohaline lake environment.

The red beds contrasted with the olive-greyish beds by being periodically deposited in ephemeral wetlands or in a floodplain, where fine clastic sediments were deposited. The reddish colour indicates the occurrence of hematite and can be interpreted as deposition under oxidized paleo-conditions (Sagri et al., 1987, Kraus and Riggins, 2007). Both the greyish soils and the reddish soils consist mostly of clay with subordinated silt. They are characterized by unimodal distributions with a low median and a low standard deviation highlighting the almost complete absence of clastic coarser material inputs in the lacustrine and floodplain deposits. The entire interval is dominated by mixed-layers illite-smectite, smectite and illite whereas kaolinite is almost absent.

Smectite is regarded as an indicator for warm and arid climate with alternating humid and dry seasons (Singer, 1984; Yemane et al., 1987) whereas illite is a by-product of physical weathering which typically occurs in colder and more drier environments with weak weathering (Singer, 1984). Kaolinite is an erosive product of (K/Na)-Al feldspar weathering (Huang, 1974) and is therefore regarded as a product of enhanced silicate weathering which is typical for humid and wet climates (Bolle and Adatte, 2001; Saleh, 2013; Chen et al., 2016).

Diagenetic reactions and mineral transitions strongly affect the clay mineral assemblage in the sediments and could lead to misinterpretations in terms of paleoclimate reconstructions and paleo depositional environment. These thermal and pressure forced reactions such as the conversion from smectite to illite are mainly taking place after a burial depth of more than 2 kilometres (Chamley, 1994). Although less is known about the burial history of the Paleogene sequences of the Hengyang basin, it is assumed that the overburden of 2 km was not reached. The reason behind this lies in the presence of a high smectite fraction in all intervals which refuses late diagenesis (Bolle and Adatte, 2001). Additionally, the structure of the sandstone samples showed only evidence of early stage diagenesis in forms of concavo-convex structures, which already occur at shallow depths (Borak and Friedman, 1981). Therefore, the diagenetic impact on the clay mineral assemblage of the studied units is regarded as extraneous.

The high abundance of smectite and illite and the absence of kaolinite in the pre-PETM units indicates that the climate was temperate, arid with low weathering. However, seasonality was likely not strongly pronounced as shown by only minor abundance of slickensides in this basal interval. Kraus and Riggins (2007) reported that slickensides only form under pronounced wet and dry seasons or alternatively, through the fluctuation of the water table (Kraus, 1998). The latter is more likely the reason for the minor slickensides in the basal interval because of the non-continuous occurrence of slickensides and the alteration of water level in the lacustrine environment.

Other evidence for a low weathering during the pre-PETM phase is found in the abundance of illite, the almost total lack of kaolinite and in the mineralogy of the pre-PETM sandstones. Basu (1976) found in an empirical approach that feldspars are readily weathered in humid and wet conditions because of the vulnerability of

feldspars against dilution effects (Hsü, 2014). However, feldspars were highly abundant in the pre-PETM sandstone samples and object a strong weathering or indication of humidity.

Like the red beds but contrasting to the greyish-beds of the basal interval, the siltstone layers of the alluvial sandstone bodies of interval 3C deposited under oxidized environmental conditions. The reason behind this was found in the reddish colour and in the sandstone samples in which an iron oxide rim around the quartz and feldspar grains exists. This was classified based on the schema of Chan et al. (2006) as early Fe^{3+} grain coating. The reddish siltstone layers intercalating the alluvial sand bodies are mottled and occasionally contain carbonate nodules indicating a weak soil formation that episodically occurred on these silty floodplain deposits. The upper part of these overbank deposits between 27 and 32 m are characterized by the occurrence of silty-sandy bimodal distributions which is also seen in the abundance of EM3 and EM4 in these units (**Figure 22**). These coarser units were deposited in proximal crevasse splay deposits and were not found in the basal interval between 0 and 10 m. These coarser deposits took place at a time when the isotope signal was already shifted towards lighter isotopic pre-onset compositions indicating a preceding shift in atmospheric $\delta^{13}C$ composition. Therefore, the impact of a pre-onset climatic shift on these coarser pre-onset deposits cannot be ruled out.

Even though laterally exposure of rocks in the studied location are limited, it is likely that the alluvial deposits of interval 3C belong to an avulsion system. The reasons behind this lie in the findings of some alluvial channel deposits around 60 m north-east of interval 3C in vicinity of the lake (**Figure 3**) and the succession of PETM over bank deposits in the Dongfeng section.

5.3 Pronounced seasonality and periodical weathering – PETM floodplain environments

The units from 37 m to 63 m were deposited during the PETM body and are interpreted as proximal to distal crevasse splay deposits with subsequent soil formation. The very fine-grained sandy layers are overlain by mostly clayish and silty paleosols with abundant pedogenic features and a characteristic reddish to dark brown colour. Therefore, it is suggested that the primarily oxidized environmental conditions found in the red beds of the pre-PETM continued throughout the PETM body. Greyish-greenish colours are completely absent in the PETM body and do not insinuate any reduced conditions as it was found in the lacustrine beds of the basal pre-PETM interval.

The overbank deposits, as they occur in the PETM body of the Dongfeng section, form due to a breach of a river bank (Brierley and Hickin, 1992). This typically occurs at times of peak flood discharge or when flood waters outreach the levee (Coleman, 1969). Coarser silt accumulates with sandy particles in marginal channel crevasse splay deposits whereas clay and finer silt particles tend to accumulate in more distal floodplains (Coleman, 1969; Kraus, 1999). Aside from clay dominance, grain size analysis of the PETM body units showed high silt fractions and sandier grains which is reflected in the abundance of the bimodal distributed EM3. However, the silt and sand fraction rise and decline alternately during the PETM, especially in interval 3B, indicating that river channels are close at times containing coarser deposits and potentially prograde into more distal parts of the basin when the deposits of silt and sand are depleted.

The pedogenic features of the finer over bank deposits are strongly pronounced in the PETM. Slickensides and mottling abundantly occur in the PETM body and more frequently than in the pre-PETM units. The abundance of slickensides and the mottled structure indicate intensified dry periods alternating with wetter episodes (Kraus and Riggins, 2007). The clay analysis of the PETM body units showed a massive increase in smectite which supports the indication of pronounced dry and wet seasonality during the PETM. Furthermore, the illite fraction declined in the PETM units which marks a considerable shift away from temperate climate conditions of the pre-PETM.

The kaolinite content remained almost absent in the PETM and in the pre-PETM units and did not show evidence of humidity. However, the transformation of smectite to kaolinite only takes place under abundant rainfall in humid conditions (Pal et al., 1989). According to the mica weathering sequence, which is presented in Deepthy and Balakrishnan (2005), the shift from illite to smectite in the PETM emphasizes that weathering intensified during the PETM but the frequency of rainfall was not high enough to reach the formation of kaolinite. The kaolinite / smectite ratio (K/Sm) is often used as a climate proxy to distinguish between aridity, in which the K/Sm ratio is close to 0, and humid climate where K/Sm values are increased (Adatte et al., 2002; Chen et al., 2016). The K/Sm ratio of the pre-PETM phase in the Dongfeng section has an average value of about 0.09. In the PETM body, the averaged K/Sm ratio decreased to 0.04. Using this paleoclimate indicator, the decrease in the K/Sm ratio indicates a clear climatic shift towards more aridity in the PETM.

Carbonate nodules and micro-accumulation of carbonates are strongly present in the PETM body and more abundant than in the pre-PETM soils. Carbonate nodules are often linked with moderately well drained soil layers (Kraus and Riggins, 2007) where the MAP should not exceed 760 mm (Royer, 1999) or 1000 mm (Retallack, 1994). This range lies in the simulated MAP from the PaCMod model. However, a recent study of Abels et al. (2016) showed that bulk oxide MAP estimates indicate that soil nodules also occur in environments with MAP between 1200 and 1500 mm/yr. Furthermore, the soil drainage also depends on the clay content, where clay rich soils are less permeable and therefore less drained (Kraus, 2002). The clay fraction of the PETM body units fluctuate over the entire interval and therefore it is expected that the level of drainage variegates as well. A correlation between the abundance of carbonate nodules and the drainage pattern is untenable and without further studies analysing bulk oxide ratios in the soils or leaf physiognomy leaves the MAP patterns at the PETM in the Hengyang basin unresolved. Nevertheless, it is likely that the weathering during the PETM was enhanced in comparison to the pre-PETM basal interval 3D. The reason behind this is found in the increased smectite fraction, the paleosol structures and the mineralogy of the PETM crevasse sandstones. Smectite forms in areas which are characterized by flooding during humid seasons followed by accumulation in the soil during dry seasons (Robert and Kennett, 1994). The massive increase in smectite in the PETM units reflects that the flooding events and the dry seasons drastically intensified in the PETM in comparison to the pre-PETM phase which goes hand in hand with the increased abundance of slickensides in the PETM units.

The crevasse sand bodies of the PETM units are mineralogically mature and mostly consist of quartz grains. Feldspars which are vulnerable to weathering (Basu, 1976; Hsü, 2014) were almost absent in the PETM sandstones indicating a period with enhanced weathering. This is contrasting to the feldspar rich sandstones of

the pre-PETM phase. Most likely, the weathering transformed the feldspars and micas into smectite but not into kaolinite. An even more intensification of weathering would have led to kaolinite formation, since kaolinite is the last step of the feldspar weathering sequence before hydroxide minerals are formed (McKinley et al., 2003). The increased weathering in the Hengyang region occurred only episodically during the pronounced wet seasons.

During these periods of enhanced weathering and flooding episodes, an avulsion system with an aggradation of floodplain deposits, which were subsequently faced with intensified drying and altered by pedogenesis involving the formation of frequent slickensides features and mottles, emerged in the Hengyang basin because of the PETM. The enhanced weathering and flood events alternated by intensified drying led to avulsion and to coarser alluvium deposits which were absent in the basal pre-PETM interval. This is also seen in the comparison of the grain size analysis, in which the distributions of the pre-PETM1 group were very clay rich and of unimodal type, whereas bimodal coarser distributions abundantly occurred within the PETM body. This trend in coarsening deposits during the PETM is regarded as a sedimentary response to the intensified flooding events during the PETM. The deposit of coarser particles matches the theoretical consideration of the established generalized PETM simulation and other model predictions (Armitage et al., 2011) of increased sediment discharge as a function of intensified weathering and flooding events.

The absence of coarser floodplain deposits in the basal pre-PETM interval could have had three main reasons. First, the basal pre-PETM interval reflects only distal floodplains or clay rich ephemeral wetlands of the lake environment. Second, coarser material was bypassed and not deposited in the floodplains. Third, the level of weathering and water discharge was too low and flooding events rare to transport coarser bedload. The findings presented here support the latter reason where evidence of temperate climate with low weathering was found. However, based on the findings of this thesis and the available information, the other two reasons cannot be entirely ruled out.

5.4 Recovery Phase – Reduced environmental conditions

The paleosols ranging from 63 m to the top of the analysed stratigraphy significantly differ from the paleosols underneath and were allocated to the recovery-phase of the PETM marked by the rapid shift towards heavier isotopic compositions. These units are characterized by purple colour followed by some light-grey layers which were deposited in more waterlogged distal floodplains or even in a lacustrine setting. These greyish and purple colours usually indicate reduced environments related to seasonal drainage, iron degradation and partial depletion of hematite (Kraus and Riggins, 2007; Kraus et al., 2013). Therefore, it is conclusive that a shift from oxidized PETM conditions towards reduced environmental conditions in the recovery-phase occurred.

However, the recovery-phase found in the Dongfeng section is only 2.5 m thick and the outcrop of moderate quality which does not allow any further conclusions.

5.5 Sediment transport and accumulation rate

The pre-PETM and PETM sandstones are sedimentary immature and are hardly rounded. The roundness which mainly happens through abrasion increases with the distance of transportation (Plumley, 1948). The hardly rounded grains from the PETM and pre-PETM samples therefore represent relative short transportation paths. This is unexpected because of the relatively large distance from the potential coastal catchment to the Hengyang basin which was suggested by Yan et al. (2011) (**Figure 1**). However, the reconstruction of palaeogeographical settings including the location of source rocks is always uncertain. Therefore, it could be reasonable that a relatively proximal catchment was the main source of the sediment depositions in the Hengyang basin.

The PETM sandstone samples are strongly dominated by quartz and were therefore interpreted as mineralogically more mature than the pre-PETM sandstones that contain a higher amount of feldspars and other lithic fragments. Feldspar in sandstones is common in areas with granitic source rocks, which mainly consist of quartz and feldspar (Basu, 1976). This is consistent with the findings of Yan et al. (2011) in which they estimated a coastal catchment of volcanic granites during late Cretaceous (**Figure 1**). The difference in the abundance of feldspar of the pre-PETM and PETM samples was explained through changes in climate, where enhanced periodical weathering during the PETM led to a feldspar depletion in the sandstones. However, another reason could be found in characteristically different catchments. Hsü (2014) reported that previously deposited sediments acting as catchment in downstream locations are built up of less diverse minerals and mostly consist of quartz minerals. It could then be reasonable that the influx from catchments at lower regions were more significant during the PETM than during the pre-PETM phase. However, this explanation is speculative and depends on many unknown paleo settings, such as paleogeomorphology, source rock and transport path.

Regarding the sediment accumulation, slow accumulation rates favour the development of pedogenesis and leads to less numerous but thicker soil layers (Kraus, 2002). The paleosols of the PETM body stretches roughly over 26 meters with numerous but cumulative and variable thick paleosols. The paleosols from the PETM body reflect depositions of only B horizons which indicate that the developed A horizons were eroded or overprinted and modified to B horizons. This modification can only occur at relatively slow accumulation rates or at intense soil formation (Mason and Jacobs, 2007). Based on this, it is concluded that the rate of pedogenesis exceeded the rate of deposition in the Dongfeng section during the PETM body. Consequently, the paleosols can be categorized as composite or cumulative paleosols (Kraus, 1999). However, the paleosols of the PETM body contain abundant carbonate nodules and slickensides which indicate a steady condition of deposition and are therefore of cumulative paleosol type.

5.6 Generalized PETM model response

The obtained results of the PETM climate and sediment model with PaCMod are discussed and placed into model perspectives and compared to other simulations and PETM field data. Additionally, the simulated outcomes are associated with the presented findings from the Hengyang basin. The significance and weaknesses

of the model are addressed to some extent. An elaborate perspective on the relevance of PaCMod is presented in Forzoni (2014).

5.6.1 Simulated climate response

The simulated MAP increased as a response to the temperature rise during the PETM and reached a stable value of almost 900 mm/year during the PETM body. A general increase in precipitation at the PETM was also found in the climate model of Winguth et al. (2010) and reflects the coupling of increased global mean temperature with increased global MAP (Collins et al., 2013). Even though the global precipitation increased in the PETM, the precipitation patterns differ regionally (Carmichael et al., 2013). The modelled precipitation in the region of the Hengyang basin in the PETM increased not only in PaCMod but also in the other two models (Winguth et al., 2010; Carmichael et al., 2013). This increase in precipitation was indeed found in the pedogenic features, clay assemblage and sandstone mineralogy within the PETM body of the Dongfeng section. The simulated MAP of 900 mm/year lies on the lower range of estimated PETM precipitation (800 - 1320 mm/year) values from leaf physiognomy in Wyoming (Wing et al., 2005). Besides precipitation, evaporation increased as a response to the increased atmospheric temperature. Nevertheless, the amplified evaporation did not exceed the boosted precipitation and therefore a positive net precipitation resulted. The estimated daily net precipitation was determined to be around 2 mm/day. This result is slightly higher than presented by Carmichael et al. (2017) in which the daily difference between precipitation and evaporation in east Asia was determined to be around 0.5 - 0.6 mm/day during the PETM.

The simulated climate response to the PETM in the Hengyang basin resulted in increased precipitation which was seen in the characteristics of the PETM rocks. However, the intensified precipitation in the Hengyang basin occurred periodically under pronounced seasonality rather than persistent as it occurs in humid climates. The PETM model in PaCMod does not provide any information about the frequency and intensity of rainfall and is strongly coupled to the temperature input. This result provides no answer as to whether the rainfall occurred prolonged or episodically. However, even other complex numerical climate models have problems predicting frequency and intensity of rainfall (Sun et al., 2006). Therefore, the understanding of paleosols including their pedogenic features and mineral composition is crucial since they reveal meaningful information about complex changes in hydrological cycles and climate shifting. Often the increased seasonality of the PETM is linked with intensified storms (McInerney and Wing, 2011) which is considered in PaCMod (**Table 1**) and its impact discussed in the supplementary material (***9.3***). Because of increased precipitation, the catchment model results show enhanced erosion, higher water discharge and related transport capacity for suspended load and bedload.

5.6.2 Simulated sedimentary response

The simulated increase in precipitation led to an increased river water discharge and enhanced erosion during the PETM. An increase in erosion is often linked with an increase in silicate weathering which has been identified and reported through the observation of a rise in kaolinite content during the PETM in marine and continental records (Robert and Kennett, 1994; Schmitz and Pujalte, 2003; Chen et al., 2016).

In the Hengyang basin, no rise in kaolinite was observed. This does not mean that an increase in weathering and erosion was absent. Kaolinite reflects more increased persistent weathering patterns which typically occurs in humid climate (Murray, 1999). The increased weathering in the Hengyang basin occurred seasonally and is preserved in the pedogenic features and the rise in smectite. Millot et al. (2002) found an empirical relationship between chemical weathering and physical erosion in which a rise in weathering goes hand in hand with an increase in erosion. Therefore, increased erosion is the expected consequence of the enhanced precipitation during the PETM. The simulated erosion rate showed a sharp peak at the onset of the temperature rise before it increases to a stable PETM erosion rate. The erosion rate in PaCMod is calculated in terms of runoff, vegetation cover and hillslope angle (Forzoni et al., 2014). A sudden change in runoff as it is expected during the onset can strongly affect the erosion rate (DiBiase and Whipple, 2011) and is likely the reason for the sudden peak in erosion at the temperature onset.

The increased water discharge during the PETM led to a rise in transported bedload and suspended load in the river channel. The transported volume of larger silt grains and sandy particles are in proportion to the suspended clay and finer silt volume. The difference was found in a short time lag of the bedload response to the PETM onset. The time lag of the coarser particles is linked with the lower mobility and lower transport speed of bedload material than suspended finer grains. The capability of a river to transport coarser particles strongly depends on the stream velocity and is illustrated in the Hjulström diagram (Hjulström, 1939). The stream velocity in turn increases with increasing water discharge (Leopold, 1953). An increased response in coarser particles to the boosted water discharge during the PETM is thus reasonable. An increase in coarser splay deposits was indeed found in the PETM units of the Dongfeng section and matches the simulated sedimentary response here.

A sophisticated numerical model which was developed to predict sediment discharge as a function of climate zones was developed by Cecil and Dulong (2003). They estimated a nearly zero solid sediment discharge under perhumid climates whereas in dry subhumid conditions with alternating dry and wet seasons the sediment discharge is at maximum. Therefore, it is assumed that the sediment discharge in the Hengyang basin during the PETM was at maximum. The PaCMod catchment model predicted that the river transport capacity exceeds the transported bedload which means that the river would have had more capacity to transport additionally obviously non-existent sediments from the regolith. In other words, the increased sediment discharge as a response to the PETM climate change only manifests itself if sediments are available in the catchment, respectively in the regolith. Even though the bedload fraction theoretically increases during the PETM, coarser particles are only transported and deposited if they are supplied by the catchment. A good example is found in the Tremp basin where coarse material (Claret Conglomerate) was only deposited during the beginning of the PETM (Pujalte et al., 2015; Anema, 2017) and disappeared later because of a potential depletion in the catchment. A similar depletion in the catchment could have occurred in the Hengyang region, since the coarsening deposits in the PETM are only of minor extent compared to the massive Claret Conglomerate. However, the PETM units in the Dongfeng section are floodplain deposits and only records depositions of episodic peak flood events (Coleman, 1969) whereas most of the sediments were bypassed downstream by the river.

5.7 Integration of results with global findings

Chen et al. (2016) analysed the PETM climate response in the lacustrine sediments of the Nanyang basin in central China with the paleo latitude of ~ 31°N. They associated a rise in kaolinite from 0% to 5% with a simultaneous decrease in smectite, which was dominant before the CIE onset, with the PETM. Chen et al. (2016) concluded a warmer more humid climate with enhanced silicate weathering as a response to the PETM in the Nanyang region. The decrease in smectite and the rise in kaolinite are apparently opposing the presented findings in the Hengyang basin. This is rather astonishing since the two-paleo location (Hengyang Basin 27°N; 108°E) lay in close vicinity at the PETM. However, Carmichael et al. (2017) estimated PETM paleo coordinates of 38°N, 107°E for the Nanyang basin, which lay distinctly more north than reported by Chen et al. (2016). The PETM climate model of Winguth et al. (2010) showed a northward shift of the intertropical convergence zone and an increasing precipitation trend from northern lower (30°) to higher (50°) midlatitudes. A potential farther north paleo location of the Nanyang basin may explain a wetter climate to a certain extent. It is also conceivably that climate differs spatially on a small scale in central China, as it was modelled by Carmichael et al. (2017). However, some concerns must be raised about the findings of Chen et al. (2016). Their allocation of the CIE onset was placed where no isotopically significant shift occurred. The units with the highest kaolinite fraction occur before the isotope record shifted to the most negative values and therefore their findings are to be regarded with some scepticism.

The climatic response to the PETM in the Big Horn basin (paleo latitude: 45°N, Supplementary table of Carmichael et al., 2017) was studied with alluvial paleosols and revealed an intensified and transient drying with episodically wet cycles during the PETM (Kraus and Riggins, 2007; Kraus et al., 2013) which is comparable with the findings in the paleosols of the Hengyang basin. A recent but not yet published clay study work by Wang et al. (2018) in the Bighorn basin shows a decrease in kaolinite (- 3%) and an increase in smectite (+ 11%) in the PETM and is therefore in line, except for the quantities, with the clay results of the Hengyang basin. A clay study of bathyal marine and shelf PETM-deposits (paleo latitude: 37°N, after Supplementary table of Carmichael et al., 2017) in the Tremp region in Spain is characterized through abundant calcite nodules and an increase (up to factor 2) in kaolinite and smectite revealing dominantly dry conditions with alternated wet seasons with an overall increased intra-annual humidity and enhanced physical erosion in the PETM (Schmitz and Pujalte, 2003). Except for the rise in kaolinite the increase in smectite and the interfered dry conditions with wet cycles are in accordance with the Bighorn basin and the Hengyang basin.

Similar results of the paleoclimate reconstruction in the Hengyang, Bighorn and Tremp basin suggest a transient drying with intensified wet periods in the paleo midlatitudes (27°N - 46°N) during the PETM. However, regional differences can occur and are highlighted by Carmichael et al. (2017).

The sedimentary response to the PETM in Tremp basin was analysed by Colombera et al. (2017). They found a response in the fluvial system in terms of increased channel depositions, thicker channel fills and bar forms and thicker sets of cross-stratified sandstones. These alluvial responses are interpreted as consequences of increased bedload transport and increased water discharge (Colombera et al., 2017). The rise in water discharge and increase of bedload transport was also seen in the results of the numerical model with PaCMod.

PETM related coarsening deposits in the Tremp basin were reported by Pujalte et al. (2015) and further emphasize the hypothesis of increased bedload transport as a response to the PETM. A similar alluvial response as in the Tremp basin is found in the Bighorn basin where sediment supply increased, coarser grain sizes were deposited and avulsion became more frequent (Newbury, 2010). Evidence for possible avulsions and coarser deposits were also found in the PETM floodplains of the Dongfeng section. However, the coarser deposits were of minor extent compared to the Bighorn and Tremp basin because of the bypassing of sediment downstream and a potential depletion of coarse material in the catchment. Nevertheless, the hypothesis of increased bedload material and coarsening deposits was not only found in the Tremp, Bighorn and the Hengyang basin it was also shown in the generalized PETM model in PaCMod and characterizes the sedimentary response to the PETM.

6. Conclusion

The negatively shifted CIE, characteristic for the PETM, was measured and strongly improved the existing low-resolution isotope signal in the Hengyang basin. The PETM body with values around - 12.4‰ $\delta^{13}C$ and the recovery back to heavier isotope compositions was clearly observed. However, the onset of the CIE was not directly measured because of the missing exposure of the lithologies containing the CIE onset.

The pre-PETM phase is captured in reduced olive-greyish palustrine deposits and oxidized fine-grained reddish floodplain or ephemeral wetland paleosols with slow pedogenetic imprint. The pre-PETM units are mostly dominated by mixed layers I-Sm, smectite and illite indicating a temperate climate which is also supported by less weathered sandstones. As a response to the PETM, a floodplain environment emerged in the Hengyang basin and the characteristics of the floodplain paleosols changed drastically. The dominantly oxidized reddish-brown paleosols of the PETM contained abundant carbonate nodules, slickensides and mottles indicating an alteration between dry and wet cycles. Furthermore, a drastic increase in smectite and a pronounced decline in illite was found which was interpreted as climatic response to the PETM towards more aridity with intensified drying and wet seasons.

The microscopic analysis of the PETM crevasse sandstones which mostly consist of quartz supports the intensified wet periods with enhanced weathering which led to the observed feldspar depletion. A boosted precipitation as a response to the abrupt greenhouse warming event was predicted in the numerical simulation in PaCMod and matches the findings from the field studies. The climatic response to the PETM in the Hengyang basin resembles the findings in the Bighorn and Tremp basin and suggest a transient drying alternated with intensified wet seasons during the PETM in the lower to middle midlatitudes. The simulated sedimentary response to the PETM stand out due to an increased sediment discharge in which bedload and suspended load drastically increased because of a boosted water discharge from the catchment downstream. The increase in bedload was indeed found in the coarser PETM crevasse splay deposits which were absent in the basal pre-PETM interval of the Dongfeng section. However, these coarsening deposits are in comparison to the findings in the Bighorn and Tremp basin only minimally pronounced. The reason behind this is that most of the sediments, including the coarse grains, are bypassed downstream by the river and the floodplain deposits capture only an episodically and small portion of the transported material. Additionally, a potential depletion of coarse material in the catchment was suggested as another plausible reason for an inhibited sedimentary response.

All in all, this thesis provides valuable insights into the climatic and sedimentary response to the PETM on the Asian continent which was rare so far. Nevertheless, some uncertainties arose during the research and indicates that further research is needed to deepen the understanding of the climatic and sedimentary responses to the PETM in the Hengyang region.

Following future research objectives are suggested:

- The basal pre-PETM interval of the Dongfeng section is characterized by very dispersed isotopic compositions and stable isotope signals are rare. It is suggested that enlarging the understanding of the pre-PETM interval by means of a drilling and coring project would result in valuable information concerning the characteristics of the pre-PETM depositions. The possibility of detecting continuous and stable isotope compositions to enable a clearly identifiable isotope baseline could then be used as a reference to clearly recognize pre-PETM isotopic excursions.

- The pre-PETM2 group show a constant significantly negatively shifted isotope composition over a moderate thickness of around 8 meters. The existence of pre-onset excursions has been detected and reported in the Bighorn basin. However, the characteristics of these excursions significantly differ from the here detected persistent excursion. Therefore, it is suggested to increase the resolution of the isotope measurements in this interval to identify the pattern and the time constraint of the excursion and evaluate whether potential climatic and sedimentary responses are associated with this excursion.

- The PETM body is terminated by the recovery-phase which was clearly found. However, without the detection of the CIE onset, establishing a reliable age model is impossible. It is suggested to unveil the CIE onset and the missing units between interval 3B and 3C with a drilling and coring project. The resulting lithological information would potentially provide further evidence of unexposed coarsening deposits after the CIE onset which would further support the hypothesis of coarser deposits as a sedimentary response to the PETM.

- The comprehension of temperature changes and the associated alteration in precipitation during the PETM is challenging but it is crucial to ascertain the climatic response to this greenhouse warming event. Measurements of clumped isotopes from the pedogenic carbonate nodules and an analysis of bulk oxide ratios from paleosols may enable further insights into the paleoclimate of central China.

7. Acknowledgments

Very special thanks go out to my supervisor Dr. Hemmo Abels and my co-supervisors Dr. Joep Storms and Dr. Miren Vizcaino for their assistance and meaningful discussions during this project. Thank you to Dr. Chaowen Wang and M.S. Kaipeng Ji from China University of Geosciences, Wuhan without whom the field work for the entire project would not have been possible. They also provided the clay mineral results. I also would like to thank Arnold van Dijk for his guidance with the isotope measurements at the Geoscience Laboratory at Utrecht University. Leonard Bik is thanked for thin section preparation and Siavash Honardar for assistance with the thin section analysis. Thank you to Martine Hagen, Hans Hateren and Dr. Marteen Prins for their assistance during the grain size laboratory work and the end-member modelling at VU Amsterdam. Thanks to Dr. Andrea Forzoni of Deltares for supporting and providing me the PaCMod model and to Youwei Wang from TU Delft for the intensive discussions concerning PaCMod. Many thanks to Jeffrey Olsen for proofreading my English and his review of this thesis. Finally, thanks go to the Dutch Royal Academy of Science, KNAW for funding the field campaign via a Joint Research Project grant 530-6CDP19 to Dr. Hemmo Abels of Delft University of Technology, Netherlands, and Prof. Hanlie Hong of China University of Geosciences, Wuhan, China.

8. References

Abels, H.A., Lauretano, V., Van Yperen, A.E., Hopman, T., Zachos, J.C., Lourens, L.J., Gingerich, P.D., Bowen, G.J., 2016. Environmental impact and magnitude of paleosol carbonate carbon isotope excursions marking five early Eocene hyperthermals in the Bighorn Basin, Wyoming, *Climate of the Past*, V.12, p.1151-1163.

Abdul Aziz, H., Hilgen, F.J., van Luijk, G.M., Sluijs, A., Kraus, M.J., 2008. Astronomical climate control on paleosol stacking patterns in the upper Paleocene-lower Eocene Willwood Formation, Bighorn Basin, Wyoming. *Geology*, V36, p531-534.

Adatte, T., Keller, G., Stinnesbeck, W., 2002. Late Cretaceous to early Paleocene climate and sea-level fluctuations: the Tunisian record, *Palaeogeography, Palaeoclimatology, Palaeoecology*, V178, p.165-196.

Aitchison, J.C., Ali, J.R., Davis, A.M., 2007. When and where did India and Asia collide? *Journal of Geophysical Research*, V.112, p.1-19.

Anema, J., 2017. Providing more understanding of the sudden change in sediments at the Paleocene-Eocene boundary, in the Tremp-Graus Basin, Southern Pyrenees, *Report Minor TU Delft.*

Armitage, J.J., Duller, R.A., Whittaker, A.C., Allen, P.A., 2011. Transformation of tectonic and climatic signals from source to sedimentary archive, *Nature Geoscience*, V.4, p.231-235.

Baczynski, A.A., McInerney, F.A., Wing, S.L., Kraus, M.J., Bloch, J.I., Secord, R., 2017. Constraining paleohydrologic change during the Paleocene-Eocene Thermal Maximum in the continental interior of North America, *Palaeogeography, Palaeoclimatology, Palaeoecology*, V.465., p.237-246.

Basu, A., 1976. Petrology of Holocene fluvial sand derived from plutonic source rocks: implications to paleoclimatic interpretation, *Journal of Sedimentary Petrology*, V.46, N.3, p.694-709.

Bolle, M.P., Adatte T., 2001. Palaeocene-early Eocene climate evolution in the Tethyan realm: clay mineral evidence, *Clay Minerals*, V36., p.249-261.

Borak, B., Friedman, G.M., 1981. Textures of sandstones and carbonate rocks in the worlds deepest wells (In excess of 30000 FT. Or 9.1 KM): Anadarko Basin, Oklahoma, *Sedimentary Geology*, V.29, p.131-151.

Bouilhol, P., Jagoutz, O., Hanchar, J.M., Dudas, F.O., 2013. Dating the India-Eurasia collision through arc magmatic records, *Earth and Planetary Science Letters*, V.366, p.163-175.

Bowen, G.J., Koch, P.L., Gingerich, P.D., Norris, R.D., Bains, S., Corfield, R.M., 2001. Refined isotope stratigraphy across the continental Paleocene-Eocene boundary on Polecat Bench in the northern Bighorn Basin. *Papers on Paleontology*, No.33, p.73-88.

Bowen, G.J., Clyde, W.C., Koch, P.L., Ting, S.Y., Alroy, J., Tsubamoto, T., Wang, Y.Q., Wang, Y. 2002. Mammalian dispersal at the Paleocene/Eocene boundary, *Science*, V.295, p.2062-2065.

Brierley, G.J., Hickin, E.J., 1992. Floodplain development based on selective preservation of sediments, Squamish River, British Columbia, *Geomorphology*, V.4, p.381-391.

Carmichael, M.J., Inglis, G.N., Badger, M.P.S., David, B., Naafs, A., Behrooz, L., Remmelzwaal, S., Monteiro, F.M., Rohrssen, M., Farnsworth, A., Buss, H.L., Dickson, A.J., Valdes, P.J., Lunt, D.J., Pancost, R.D., 2017. Hydrological and associated biogeochemical consequences of rapid global warming during the Paleocene-Eocene Thermal Maximum, *Global and Planetary Change*, 157, p.114-138.

Cecil, C.B., Dulong, F.T., 2003. Precipitation models for sediment supply in warm climates, *Society of Sedimentary Geology (SEPM)*, V.77, p.21-27.

Cerling, T.E., 1984. The stable isotopic composition of modern soil carbonate and its relationship to climate, *Earth and Planetary Science Letters*, V.71, p.229-240.

Cerling, T.E., 1991. Carbon dioxide in the atmosphere: evidence from Cenozoic and Mesozoic paleosols. *American Journal of Science*, V291 (4), p.377-400.

Cerling, T.E., Quade, J., 1993. Stable carbon and oxygen isotopes in soil carbonates. In: Swart, P.K., Lohmann, K.C., Mckenzie, J., Savin, S. *Climate Change in Continental Isotopic Records, American Geophysical Union Monograph*, V.78, p.217-231.

Chamley, H., 1994. Clay Mineral Diagenesis. *In Parker A., Sellwood B.W. (eds) Quantitative Diagenesis: Recent Developments and Applications to Reservoir Geology. NATO ASI Series,*V.453, p.161-181.

Chan, M.A., Bowen, B.B., Parry, W.T., Ormö, J., Komatsu, G., 2006. Red rock and red planet diagenesis: Comparison of Earth and Mars environment. *Publication of the geological society of America,* V.15, No.8, p.4-10.

Chen, Z., Ding, Z., Yang, S, Wang, X., 2016. Increased precipitation and weathering across the Paleocene-Eocene Thermal Maximum in central China, *Geochemistry, Geophysics, Geosystems,* V.17, I6, p.2286-2297.

Cole, R.D., Picard, M.D., 1981. Sulfur-Isotope variations in marginal-lacustrine rocks of the Green River formation, Colorado and Utah, *SEPM Special Publication,* N.31, p.261-275.

Coleman, J.M., 1969. Brahmaputra River: Channel Processes and sedimentation, *Sedimentary Geology,* V3., N.2/3, p.129-239.

Collins, M., R. Knutti, J. Arblaster, J.-L. Dufresne, T. Fichefet, P. Friedlingstein, X. Gao, W.J. Gutowski, T. Johns, G. Krinner, M. Shongwe, C. Tebaldi, A.J. Weaver and M. Wehner, 2013: Long-term Climate Change: Projections, Commitments and Irreversibility. In: Climate Change 2013: The Physical Science Basis. Contribution of Working Group I to the Fifth Assessment Report of the Intergovernmental Panel on Climate Change [Stocker, T.F., D. Qin, G.-K. Plattner, M. Tignor, S.K. Allen, J. Boschung, A. Nauels, Y. Xia, V. Bex and P.M. Midgley (eds.)]. Cambridge University Press, Cambridge, United Kingdom and New York, NY, USA.

Colombera, L., Arévalo, O.J., Mountney, N.P., 2017. Fluvial-system response to climate change: The Palaeocene-Eocene Tremp Group, Pyrenees, Spain, *Global and Planetary Change,* V.157, p.1-17.

DeConto, R., Galeotti, S., Pagani, M., Tracy, D.M., Pollard, D., Beerling, D.J., 2010. Hyperthermals and orbitally paced permafrost soil organic carbon dynamics, *AGU,* PP21E-08.

Deepthy, R., Balakrishnan, S., 2005. Climatic control on clay mineral formation: Evidence from weathering profiles developed on either side of the Western Ghats, *Earth System Science,* V.114, No.5, p.545-556.

DiBiase, R.A., Whipple, K.X., 2011. The influence of erosion thresholds and runoff variability on the relationships among topography, climate, and erosion rate, *Journal of Geophysical Research,* V.116, F04036.

Dickens, G.R., 2000. Methane oxidation during the late Paleocene Thermal Maximum. *Bulletin de la Societe Geologique de France,* V.171, p.37-49.

Diefendorf, A.F., Mueller, K.E., Wing, S.L., Koch, P.L., Freeman, K.H., 2010. Global patterns in leaf ^{13}C discrimination and implications for studies of past and future climate. *PNAS,* V.107, No.13, p.5738-5743.

Ding, L., Spicer, R.A., Yang, J., Xu, Q., Cai, F., Li, S., Lai, Q., Wang, H., Spicer, T.E.V., Yue, Y., Shukla, A., Srivastava, G., Khan, M.A., Bera, S., Mehrotra, R., 2017. Quantifying the rise of the Himalaya orogen and implications for the South Asian monsoon, *Geology,* V.45, N.3, p.215-218.

Ekdale, A.A., Mason, T.R., 1988. Characteristic trace-fossil associations in oxygen-poor sedimentary environments, *Geology,* V16(8), p.720-723.

Folk, R.L., Andrews, P.B., Lewis, D.W., 1970. Detrital sedimentary rock classification and nomenclature for use in New Zealand. *Journal of Geology and Geophysics,* 13:4, p.937-968.

Forzoni, A., De Jager, G., Storms, J.E.A., 2013. A spatially lumped model to investigate downstream sediment flux propagation within a fluvial catchment, *Geomorphology,* V.193, p.65-80.

Forzoni, A., 2014. Transmission of climate, sea-level, and tectonic signals across river systems. (Book)

Forzoni, A., Storms, J.E.A., Whittaker, A.C., de Jager, G., 2014. Delayed delivery from the sediment factory: modelling the impact of catchment response time to tectonics on sediment flux and fluvio-deltaic stratigraphy, *Earth Surf. Process. Landforms,* V39, p.689-704.

Fossilworks database, 2016. PaleoDB collection 180727, Changpiliang, IVPP Loc. 76005 (Eocene of China), http://fossilworks.org/cgi-bin/bridge.pl?a=collectionSearch&collection_no=180727

Freytet, P., Verrecchia, E.P., 2002. Lacustrine and palustrine carbonate petrography: an overview. *Journal of Paleolimnology,* V.27, p.221-237.

Gingerich, P.D., 2003. Mammalian responses to climate change at the Paleocene-Eocene boundary: Polecat Bench record in the northern Bighorn Basin, Wyoming, *Geological Society of America Special Paper,* V.369, p.463-478.

Gingerich, P.D., 2010. Mammalian faunal succession through the Paleocene-Eocene Thermal Maximum (PETM) in western North America, *Vertebrata Palasiatica*, V10, p.308-327.

Heinemann, M., Jungclaus, J.H., Marotzke, J., 2009. Warm Paleocene/Eocene climate as simulated in ECHAM5/MPI-OM, *Clim. Past*, V.5, p.785-802.

Houseknecht, D.W., 1984. Influence of Grain Size and Temperature on Intergranular Pressure Solution, Quartz Cementation, and Porosity in a Quartzose Sandstone, *Journal of Sedimentary Petrology*, V.54, No.2, p.348-361.

Hjulström, F., 1939. Transportation of detritus by moving water: Part 1. Transportation, In P.D. Trask (ED.), *Recent marine sediments, Symposium Oklahoma*, p.5-31.

Hsü, K.J., 2014. Physics of sedimentology, 2nd edition, Springer, (Book).

Hu, X., Garzanti, E., Wang, J., Huang, W., An, W., Webb, A., 2017. The timing of India-Asia collision onset – Facts, theories, controversies, *Earth-Science Reviews*, V.160, p.264-299.

Huang, W.H., 1974. Stabilities of Kaolinite and Halloysite in Relation to Weathering of Feldspars and Nepheline in Aqueous Solution, *American Mineralogist*, V.59, p.365-371.

Jaramillo, C., Ochoa, D., Contreras, L., Pagani, M., Carvajal-Ortiz, H., Pratt, L.M., Krishnan, S., Cardona, A., Romero, M., Quiroz, L., Rodriguez, G., Rueda, M.J., De la Parra, F., Morón, S., Green, W., Bayona, G., Montes, C., Quintero, O., Ramirez, R., Mora, G., Schouten S., Bermudez, H., Navarrete, R., Parra, F., Alvarán, M., Osorno, J., Crowley, J.L., Valencia, V., Vervoort, J., 2010. Effects of Rapid Global Warming at the Paleocene-Eocene Boundary on Neotropical Vegetation, *Science*, 330, p.957-961.

Jackson, M.L., 1975. Soil Chemical Analysis. Madison, W1, USA.

John, C.M., Bohaty, S.M., Zachos, J.C., Sluijs, A., Gibbs, S., Brinkhuis, H., Bralower, T.J., 2008. North American continental margin records of the Paleocene-Eocene thermal maximum: Implications for global carbon and hydrological cycling, *Paleoceanography*, Vol. 23, p.1-20.

Kennett, J.P., Stott, L.D., 1991. Abrupt deep-sea warming, palaeoceanographic changes and benthic extinctions at the end of the Palaeocene. *Nature*, Vol 353, p.225-229.

Klootwijk, C.T., Gee, J.S. Peirce, J.W., Smith, G.M., 1992. An early India-Asia contact: Paleomagnetic constraints from Ninetyeast Ridge, ODP Leg 121, *Geology*, V.20, p.395-398.

Koch, P.L., Zachos, J.C., Gingerich, P.D., 1992. Correlation between isotope records in marine and continental carbon reservoirs near the Paleocene/Eocene boundary, *Nature*, V.358, p.319-322.

Koch, P.L., Zachos, J.C., Dettman, D.L., 1995. Stable isotope stratigraphy and paleoclimatology of the Paleogene Bighorn Basin (Wyoming, USA), *Palaeogeography, Palaeoclimatology, Palaeoecology*, V.115, p.61-89.

Kraus, M.J., 1999. Paleosols in clastic sedimentary rocks: their geologic applications, *Earth Science Reviews*, V.47, p.41-70.

Kraus, M.J., 2002. Basin-Scale Changes in Floodplain Paleosols: Implications for Interpreting Alluvial Architecture. *Journal of Sedimentary Research*, V.72(4), p.500-509.

Kraus, M.J., Riggins, S., 2007. Transient drying during the Paleocene-Eocene Thermal Maximum (PETM): Analysis of paleosols in the bighorn basin, Wyoming. *Palaeogeography, Palaeoclimatology, Palaeoecology*, V.245, p.444-461.

Kraus, M.J., McInerney, F.A., Wing, S.L., Secord, R., Baczynski, A.A., Bloch, J.I., 2013. Paleohydrologic response to continental warming during the Paleoceen-Eocene Thermal Maximum, Bighorn Basin, Wyoming. *Palaeogeography, Palaeoclimatology, Palaeoecology*, V.370, p.196-208.

Kurtz, A.C., Kump, L.R. Arthur, M.A. Zachos, J.C., Paytan, A., 2003. Early Cenozoic decoupling of the global carbon and sulfur cycles, *Paleoceanography*, V18, N4, p.14.1-14.14

Leopold, L.B., 1953. Downstream change of velocity in rivers, *American Journal of science*, V.251, p.606-624.

Li, Z.X., Li, X.H., 2007. Formation of the 1300 km-wide intracontinental orogen and post-orogenic magmatic province in Mesozoic South China: a flat – slab subduction model, *Geology*, V35, p.179-182.

Liu, Xun, Fu, De Yung, 1986. Sedimentary facies and the tectonic development of the Hengyang Basin, Hunan Province: *Bulletin of the Chinese Academy of Geological Sciences*, V. 13, p.13-16.

Magioncalda, R., Dupuis, C., Smith, T., Steuerbraut, E., Gingerich, P.D., 2004. Paleocene-Eocene carbon isotope excursion in organic carbon and pedogenic carbonate: direct comparison in a continental stratigraphic section, *Geology*, V.32, p.553-556.

Marshall, J.D., 1992. Climatic and oceanographic isotopic signals from the carbonate rock record and their preservation, *Geol. Mag.*, V.129 (2), p.143-160.

Mason, J.A., Jacobs, P.M., 2007. Nature of Paleosols, In: *Encyclopedia of Quaternary science, Elias,S.A, Mock, C.J.*, Elsevier, V.2, p.2086-2095.

McInerney, F.A., Wing, S.L., 2011. Thermal Maximum: A Perturbation of Carbon Cycle, Climate, and Biosphere with Implications for the Future. *Annu. Rev. Earth Planet. Sci.*, 39, p.489-516.

McKinley, J.M., Worden, R.H., Ruffell, A.H., 2003. Smectite in sandstones: a review of the controls on occurrence and behaviour during diagenesis, *Clay Mineral Cements in Sandstones, International Association of Sedimentologists*, V34., p.109-128.

Meijer, N., Abels, H.A., Lourens, L.J., 2015. Onset of the Paleocene-Eocene Thermal Maximum (PETM) in the northern Bighorn Basin, Wyoming, Master Thesis, Utrecht University.

Millot, R., Gaillardet, J., Dupré, B., Allègre, C.J., 2002. The global control of silicate weathering rates and the coupling with physical erosion: new insights from rivers of the Canadian Shield, *Earth and Planetary Science Letters*, V.196, p.83-98.

Murray, H.H., 1999. Applied clay mineralogy today and tomorrow, *Clay Minerals*, V.34, p.39-49.

Murphy, B.H., Farley, K.A., Zachos, J.C., 2010. An extraterrestrial 3He-based timescale for the Paleocene – Eocene Thermal Maxmium (PETM) from Walvis Ridge, IODP site 1266, *Geochim. Cosmochim.* Acta 74, p.5098-5108.

Nelson, 2018. Earth and Environmental Sciences 2120 Petrology, http://www.tulane.edu/~sanelson/eens212/index.html

Newbury, S.S., 2010. The sedimentary Response to Climate Change during the Paleocene-Eocene Thermal Maximum, Southeastern Bighorn Basin, Wyoming, USA, *Geological Sciences Graduate Theses & Dissertations*, 20.

Pal, D.K., Deshpande, S.B., Venugopal, K.R., Kalbande, A.R., 1989. Formation of di- and trioctahedral smectite as evidence for paleoclimatic changes in southern and central peninsular India, *Geoderm*, V.45, p.175-184.

Paterson, G.A., Heslop, D., 2015. New methods for unmixing sediment grain size data, *Geochemistry, Geophysics, Geosystems*, V16, p.4494-4506.

Pearson, P.N., Thomas, E., 2015. Drilling disturbance and constraints on the onset of the Paleocene-Eocene boundary carbon isotope excursion in New Jersey, *Climate of the past*, V.11, p.95-104.

Penman, D.E., Hönisch, B., Zeebe, R.E., Thomas, E., Zachos, J.C., 2014. Rapid and sustained surface ocean acidification during the Paleocene-Eocene Thermal Maximum, Paleoceanography, 29, p.357-369.

Pettijohn, F.J., Potter, P.E., Siever, R., 1973. Sand and Sandstone. *Springer-Verlag*, p.1-617.

Plumley, W.J., 1948. Black Hills Terrace Gravels: A Study in Sediment Transport, *The Journal of Geology*, V.56, No.6, p.526-577.

Prins, M.A., Postma, G., Weltje, G.J., 2000. Controls on terrigenous sediment supply to the Arabian Sea during the late Quaternary: the Makran continental slope, *Marine Geology*, V.169, p.351-271.

Pujalte, V., Bacceta, J.I., Schmitz, B., 2015. A massive input of coarse-grained siliciclastics in the Pyrenean Basin during the PETM: the missing ingredient in a coeval abrupt change in hydrological regime, *Clim. Past*, V.11, p.1653-1672.

Retallack, G.J., 1988. Field recognition of paleosols, *Special Paper of the geological society of America, V216, p.1-20.*

Retallack, G.J., 1994. The environmental factor approach to the interpretation of paleosols. *Amundson, R., Harden, J.W, Singer, M.J., Factors of soil formation.* V33., p31-64.

Robert, C., Kennett, J.P., 1994. Antarctic subtropical humid episode at the Paleocene-Eocene boundary: clay-mineral evidence, *Geology*, V.22, p.211-214.

Röhl, U., Westerhold, T., Bralower, T.J., Zachos, J.C., 2007. On the duration of the Paleocene-Eocene thermal maximum (PETM), *Geochemistry Geophysics Geosystems*, Vol.8, No 12, p.1-13.

Royer, D.L., 1999. Depth to pedogenic carbonate horizon as a paleoprecipitation indicator. *Geology*, V.27, p.1123-1126.

Sagri, M., Abbate, E., Bruni, P., 1989. Deposits of ephemeral and perennial lakes in the Tertiary Daban Basin (Northern Somalia), *Palaeogeography, Palaeoclimatology, Palaeoecology*, V.70, p.225-233.

Saleh, H.M.A.K., 2013. Sedimentology, Geochemistry and Mineralogy of the Paleocene-Eocene Thermal Maximum (PETM): Sediment Records from Egypt, India and Spain. *Thèse de doctorat UNIL*.

Schmitz, B., Pujalte, V., 2003. Sea-level, humidity, and land-erosion records across the initial Eocene thermal maximum from a continental-marine transect in northern Spain, *Geology*, V.31, No. 8, p.689-692.

Singer, A., 1984. The Paleoclimatic interpretation of Clay minerals in sediments – a Review, *Earth-Science Reviews*, V.21, p.251-293.

Smith, T., Rose, K.D., Gingerich, P.D., 2006. Rapid Asia-Europe-North America geographic dispersal of earliest Eocene primate Teilhardina during the Paleocene-Eocene Thermal Maximum, *Proceedings of the National Academy of Sciences*, V. 103 (30), 11223-11227.

Smith, F.A., Wing, S.L., Freeman, K.H., 2007. Magnitude of the carbon isotope excursion at the Paleocene-Eocene thermal maximum: The role of plant community change, *Earth and Planetary Science Letters*, V.262. p.50-65.

Snell, K.E., Thrasher, B.L., Eiler, J.M., Koch, P.L., Sloan, L.C., Tabor, N.J., 2012. Hot summers in the Bighorn Basin during the early Paleogene, *Geology (2013)*, V.41(1), p.55-58.

Sun, Y., Solomon, S., Dai, A., Portmann, R.W., 2006. How often does it rain? *Journal of Climate*, V19, p.916-934.

Sun, Z., Yang, Z., Yang, T., Pei, J., Yu, Q., 2006. New Late Cretaceous and Paleogene paleomagnetic results from south China and their geodynamic implications., *Journal of Geophysical Research, V.111, B03101.*

Svensen, H., Planke, S., Malthe-Sørenssen, Jamtveit, B., Myklebust, R., Eidem Rasmussen, T., Rey, S.S., 2004. Release of methane from a volcanic basin as a mechanism for initial Eocene global warming, *Nature*, V.429, p.542-545.

Swart, P.K., 2015. The geochemistry of carbonate diagenesis: The past, present and future. *Sedimentology*, V.62. p.1233-1304.

Ting, S.Y., 1998. Paleocene and early Eocene land mammals ages of Asia. *Bulletin of Carnegie Museum of Natural History, V.* 34 p.127-147.

Ting, S.Y., Bowen, G.J., Koch, L.P., Clyde W.C., Wang, Y., McKenna, M.C., 2003. Biostratigraphic, chemostratigraphic, and magnetostratigraphic study across the Paleocene-Eocene boundary in the Hengyang Basin, Hunan, China, *Geological Society of America Special Papers*, V. 369, p.521-535.

Turner, S.K., Hull, P.M., Kump, L.R., Ridgwell, A., 2017. A probabilistic assessment of the rapidity of the PETM onset. *Nature communications*, V.8, 353.

Van der Meulen, B., 2015. Constraints on the duration of the Paleocene-Eocene Thermal Maximum by orbitally-influenced fluvial sediments of the northern Bighorn Basin, Wyoming, MSc Thesis – Utrecht University, p.1-26.

Van der Meulen, B., Lourens, L.J., Meijer, N., Van Broekhuizen, S., Van Ginneken, S., Gingerich P.D., Abels, H.A., 2018. Carbon isotope and mammal recovery from extreme greenhouse warming at the Paleocene-Eocene boundary in astronomically-calibrated fluvial strata, Bighorn Basin, Wyoming, USA. *Unpublished manuscript.*

Van Hateren, J.A., Prins, M.A., Van Balen, R.T., 2017. On the genetically meaningful decomposition of grain-size distributions: A comparison of different end-member modelling algorithms. *Sedimentary Geology, p.1-23.*

Wang, C., Lourens, L.J., Adriaens, R., Elsen, J., Vandenberghe N., Hong, H., Gingerich, P.D., Abels, H.A., 2017. Clay mineralogical constraints on weathering in response to early Eocene hyperthermal events in the Bighorn Basin, Wyoming, *Bulletin of the Geological Society of America*, V.129. p.997-1011.

Wang, Y., Tong, Y., Li, Q., 2011. Chinese Continental Paleocene-Eocene Boundary and Its Correlation, *Acta Geologica Sinica*, V.85, No.2, p.443-451.

Wang, C., Abels, H., et al., 2018. Clay analysis in the Bighorn basin, Wyoming. *Unpublished manuscript*.

Westerhold, T., Röhl, U., Wilkens, R.H., Gingerich, P.D., Clyde, W.C., Wing, S.L., Bowen, G.J., Kraus, M.J., 2018. Synchronizing early Eocene deep-sea and continental records-cyclostratigraphic age models for the Bighorn Basin Coring Project drill cores, *Climate of the Past*, V.14, p.303-319.

Wing, S.L., Harrington, G.J., Smith, F.A., Bloch, J.I., Boyer, D.M., Freeman, K.H., 2005. Transient floral change and rapid global warming at the Paleocene-Eocene boundary, *Science*, V.310, p.993-996.

Winguth, A., Shellito, C., Shields, C., Winguth, C., 2010. Climate response at the Paleocene-Eocene Thermal Maximum to greenhouse gas forcing – a model study with CCSM3, *Journal of Climate*, V.23, p.2562-2584.

Wright, J.D., Schaller, M.F., 2013. Evidence for a rapid release of carbon at the Paleocene-Eocene Thermal maximum, *Proc. Natl. Acad. Sci. USA*, V.110, p15908-15913.

Wynn, J.G., 2007. Carbon isotope fractionation during decomposition of organic matter in soils and paleosols: Implications for paleoecological interpretation of paleosols. *Palaeogeography, Palaeoclimatology, Palaeoecology*, V.251, p.437-448.

Yemane, K., Robert, C., Bonnefille, R., 1987. Pollen and clay mineral assemblages of a late Miocene lacustrine sequence from the northwestern Ethiopian highlands. *Palaeogeography, Palaeoclimatology, Palaeocecology*, V.60, p.123-133.

Young, C.C., Bien, M.N., Lee, Y.Y., 1938. Red beds of Hunan, *Geological Survey of China*, V. 18, p.259-300.

Zachos, J.C., Röhl, U., Schellenberg, S.A., Sluijs, A., Hodell, D.A., Kelly, D.C., Thomas, E., Nicolo, M., Raffi, I., Lourens, L.J., Mc Carren, H., Kroon, D., 2005. Paleoclimate: Rapid acidification of the ocean during the Paleocene-Eocene Thermal Maximum, *Science*, V308, p.1611-1615.

Zeebe, R.E., Dickens, G.R., Ridgwell, A., Sluijs, A., Thomas, E., 2014. Onset of carbon isotope excursion at the Paleocene-Eocene thermal maximum took millennia, not 13 years, *PNAS*, V.111, N.12, E1062-1063.

Zhu, M., Ding, Z.L., Wang, X., Chen, Z.L., Jiang, H.C., Dong, X.X., Ji, J.L., Tang, Z.H., Luo, P., 2010. High-resolution carbon isotope record for the Paleocene-Eocene thermal maximum from the Nanyang Basin, Central China. *Chinese Science Bulletin*, Vol 55, No 31, p.3606-3611.

Zhu, D.C., Wang, Q., Zhao, Z.D., Chung, S.L., Cawood, P.A., Niu, Y., Liu, S.A., Wu, F.Y., Mo, X.X., 2015. Magmatic record of India-Asia collision, *Scientific Reports*, V.5:14289, p.1-9.

9. Supplementary material

9.1 Oxygen Isotopes

The measured $\delta^{18}O$ isotope signals are plotted next to the $\delta^{13}C$ record (**Figure 29**). The oxygen isotope signal of interval 3D is dispersed and varies from - 5.5‰ to - 10‰ $\delta^{18}O$. At interval 3C the oxygen signals fluctuate around - 8.0‰ $\delta^{18}O$ and lie close to the values of the corresponding $\delta^{13}C$ measurement.

The oxygen isotopic composition of interval 3B shows a reverse trend with respect to the carbon isotopes. In other words when the $\delta^{13}C$ shifts to lighter compositions then the $\delta^{18}O$ signal shifts towards heavier compositions. The same inverse trend is visible in the lower part of interval 3A at a stratigraphic level from 54 m to 57 m. However, at 59 m when the $\delta^{13}C$ starts increasing towards heavier isotope compositions than the oxygen signal further fluctuates between - 5‰ and - 7‰ $\delta^{18}O$ and does not reveal an increasing nor decreasing trend during the recovery-phase. All in all, the precision of the $\delta^{18}O$ values is high over the entire stratigraphy except for interval 3D.

Oxygen isotopes contrasted with carbon isotopes are rarely analysed and reported because of their susceptibility to diagenesis and diverse fractionation effects (Marshall, 1992). Koch et al. (1995) ascertained that oxygen isotopes of spars are always depleted in $\delta^{18}O$ compared to the oxygen signal of micrite indicating a formation at higher temperatures and enhanced burial depths. However, spars were separated and excluded from the isotope ratio measurements and therefore are an unlikely influence on the isotopic composition.

It is known that the $\delta^{18}O$ composition of pedogenic carbonate shows strong correlation with the isotopic composition of the local meteoric water (Cerling and Quade, 1993). However, the isotopic composition of soil water can be different than the meteoric water because of potential infiltration of isotopically different water or by isotopic modification through evaporation (Cerling and Quade, 1993). The units of interval 3D were allocated as shallow lacustrine deposits with subaerial exposure and subsequent pedogenesis. Therefore, it is likely that the isotopic compositions of these carbonate nodules were affected through lacustrine waters with uncharacteristic and significantly different isotopic compositions which could explain the wide spread in $\delta^{18}O$ and in $\delta^{13}C$.

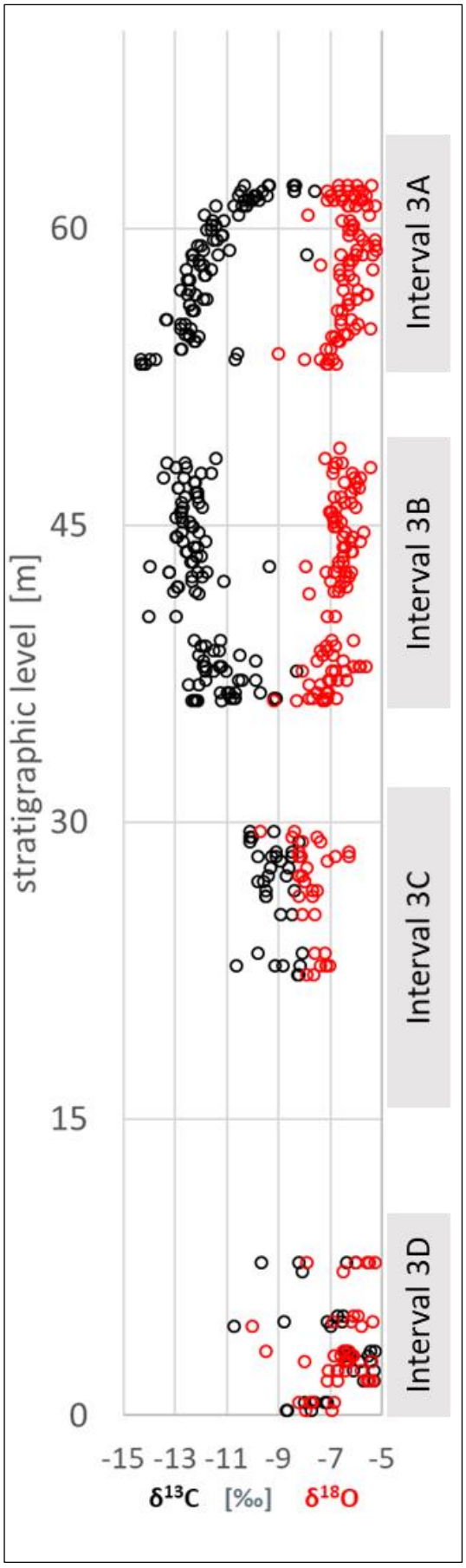

Figure 29. The carbon and oxygen isotope signals of the investigated stratigraphy.

9.2 End-member modelling

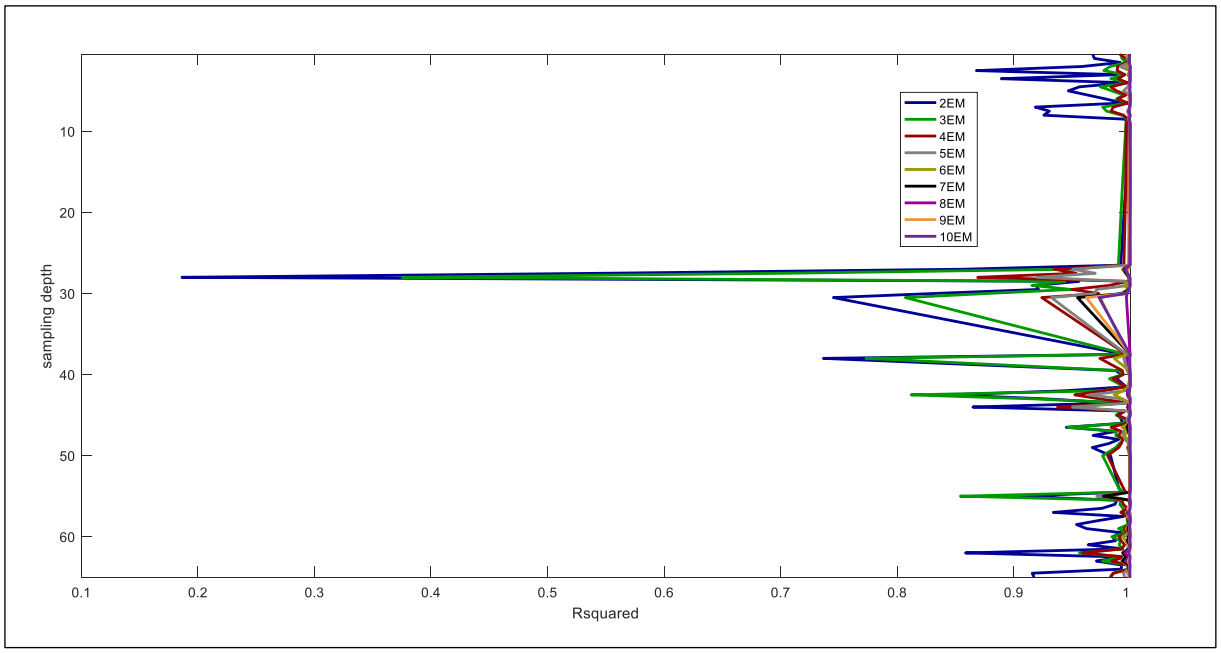

Figure 30. The R-square plot of end-member models with different number of end-members. The R-square plot reflects the goodness-of-fit statistics as a function of the stratigraphic level.

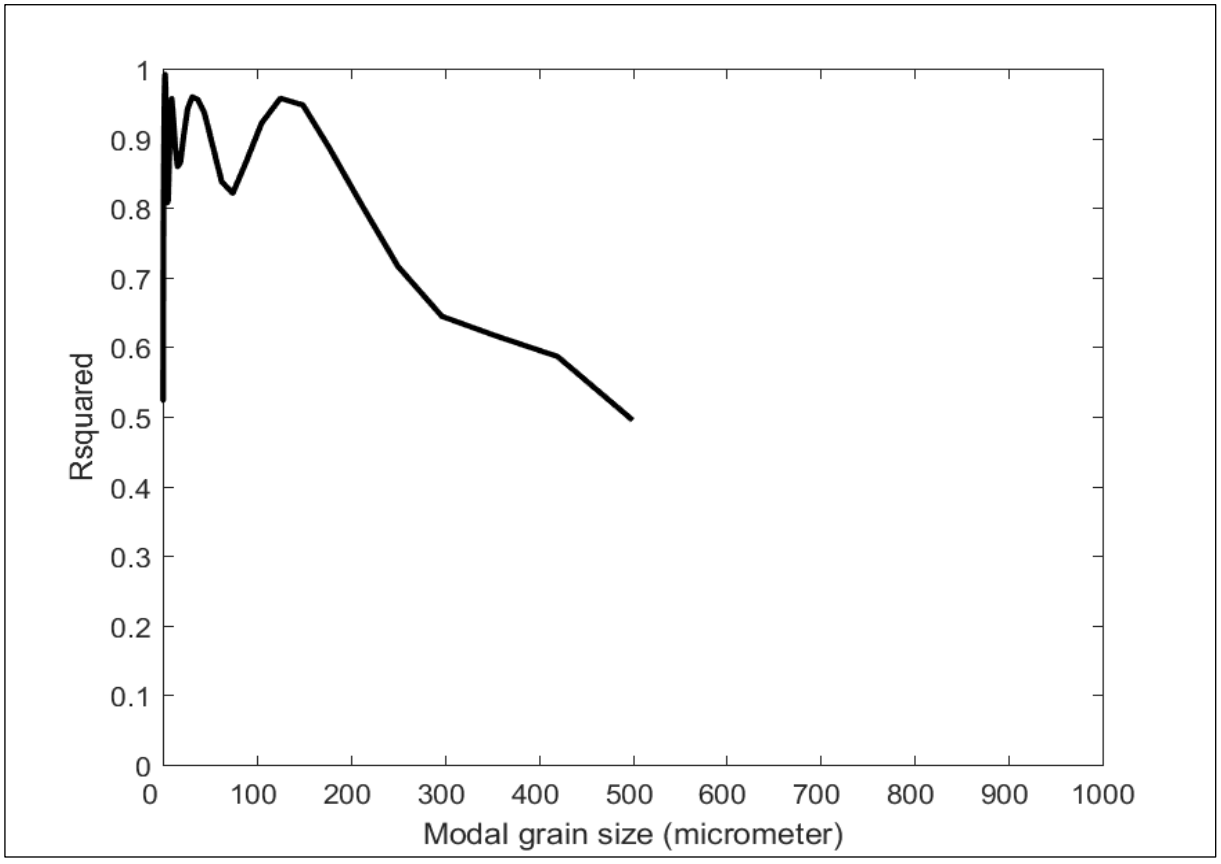

Figure 31. The R-square plot represents the goodness-of-fit statistics of the used end-member model for different grain sizes.

9.3 Sensitivity analysis of input parameters

The sensitivities of the most discussed and significant input parameters have been tested with the model to detect possible changes in the response to the rapid temperature change. The most interesting climate variables in the studies around the Paleocene-Eocene Thermal maximum are the intensity of seasonality and storminess. Altering the storminess coefficient led to drastically changing results and is inferred as very sensitive input parameter. An increase in storminess from 0.5 to 0.8 causes a decrease in water discharge and therefore a reduced bedload and a reduced suspended load (**Figure 32**). The storminess is inversely proportional to the probability of a wet day and explains that high storminess lead to less precipitation (Forzoni et al., 2013). The shapes of the transport curves do not change but they shift along the y-axis to smaller values. In contrast to the storminess, the effect of decreased seasonality lowers the water discharge, bedload and suspended sediment transport (**Figure 33**). A remarkable effect of increased seasonality, which is achieved in PaCMod through increased temperature differences between the seasons, is the increase in temporarily stored confined floodplain reservoirs (**Figure 34**).

The morphologic inputs such as the maximum relief of the catchment, river length and basin area also have an influence on the climate respectively sedimentary response. The maximum relief of the catchment turned out to be a very sensitive input parameter. The higher the relief the higher is the generated water discharge and the sediment supply increases drastically (**Figure 35**). The reason behind this is the strong dependence of altitude on precipitation (Forzoni, 2014). Water discharge is boosted because of the strong rise in net precipitation. In fact, precipitation increases with altitude whereas the value of evaporation does not. However, the shape of the water discharge curve and the sediment transport curves do not change and only shifts on the y-axis. The length of the river from the catchment to the deposition compared to the catchment relief is not sensitive and leads to only minor changes.

The most important lithological input parameter in the numerical model is the median grain size. However, the influence on the computation is only minor. The most significant change happens in the transport capacity of the river which decreases and sometimes becomes even less than the actual bedload transport (**Figure 36**). At the point where the bedload transport exceeds the transport capacity of the river, the fraction of sediment excess is stored as a confined floodplain (Forzoni, 2014).

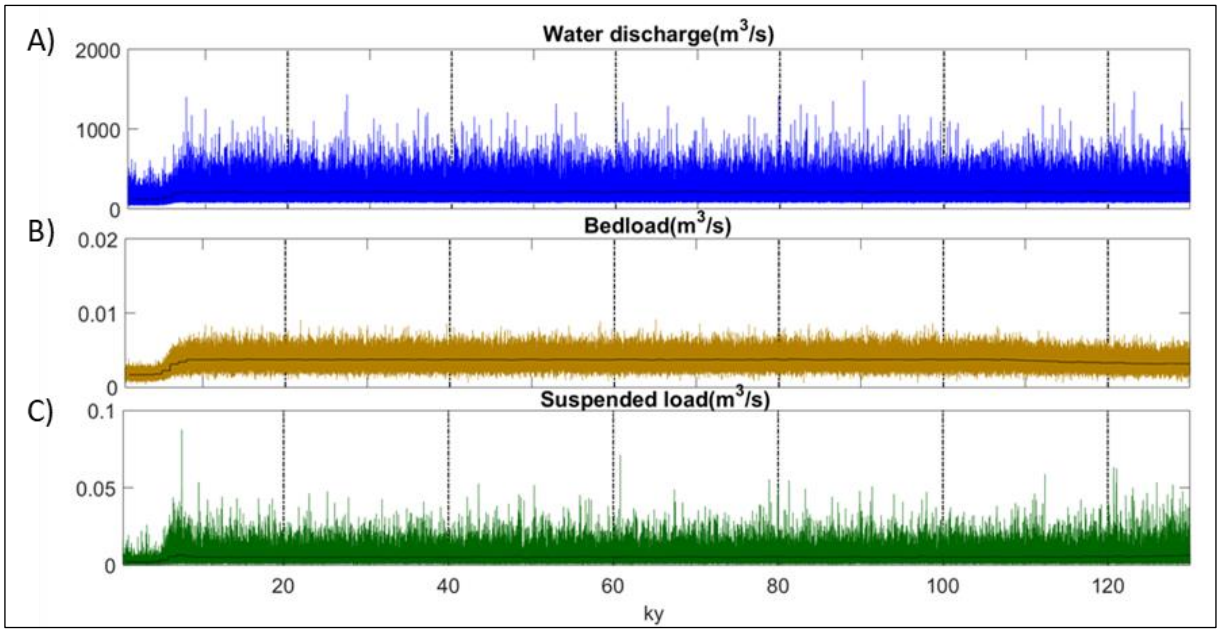

Figure 32. The simulated results with a storminess coefficient of 0.8 instead of 0.5. The water discharge is presented in Panel A, bedload transport in Panel B and the suspended load in Panel C.

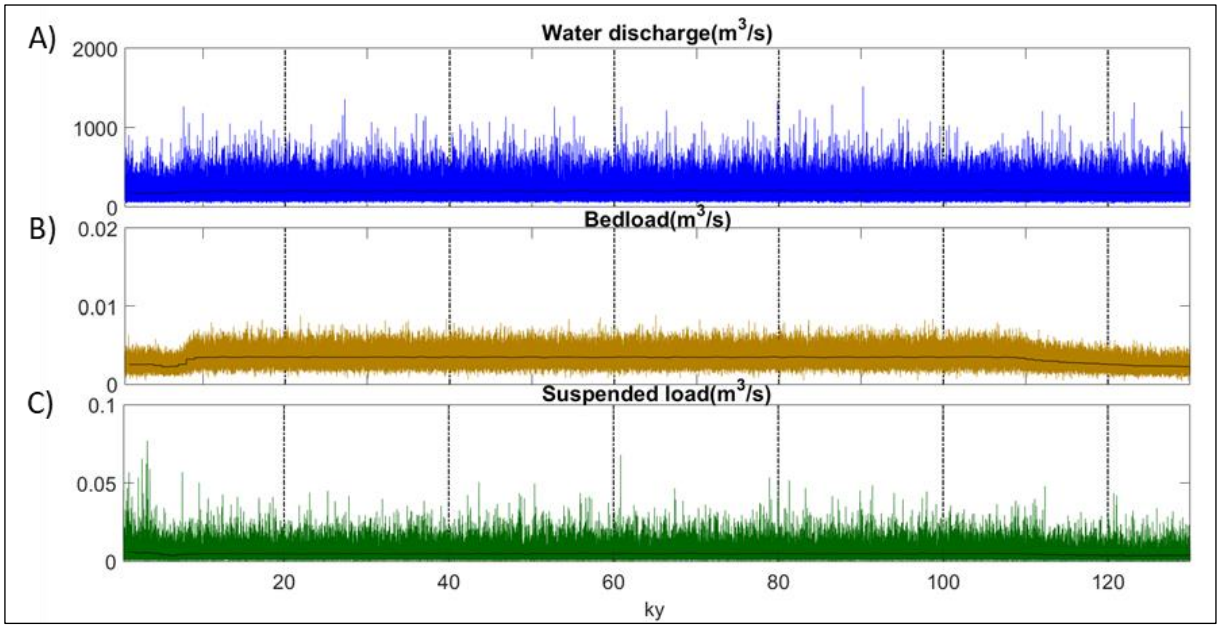

Figure 33. The simulation output with a seasonal temperature difference of 10˚C instead of 18˚C. The water discharge is presented in Panel A, bedload transport in Panel B and the suspended load in Panel C.

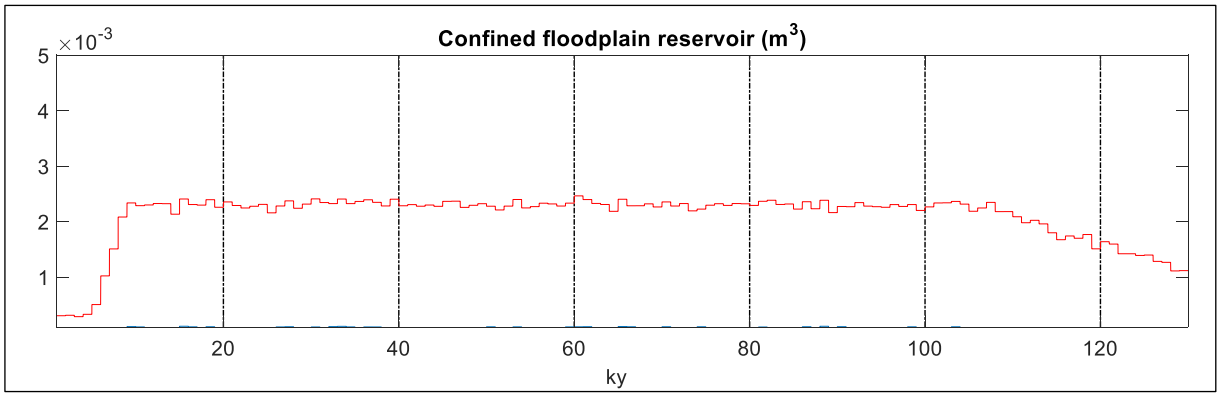

Figure 34. The confined floodplain output with an increased seasonal temperature difference of 20˚C instead of 18˚C.

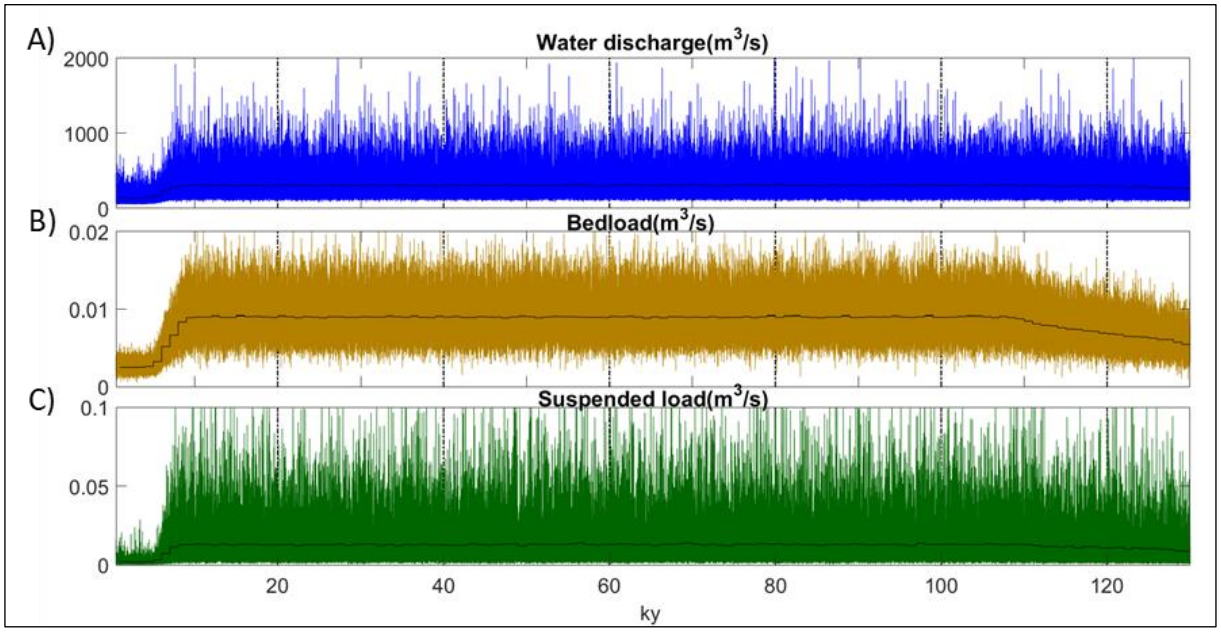

Figure 35. The simulated results with an increased relief from 1000 m to 1200 m. The water discharge is presented in Panel A, bedload transport in Panel B and the suspended load in Panel C.

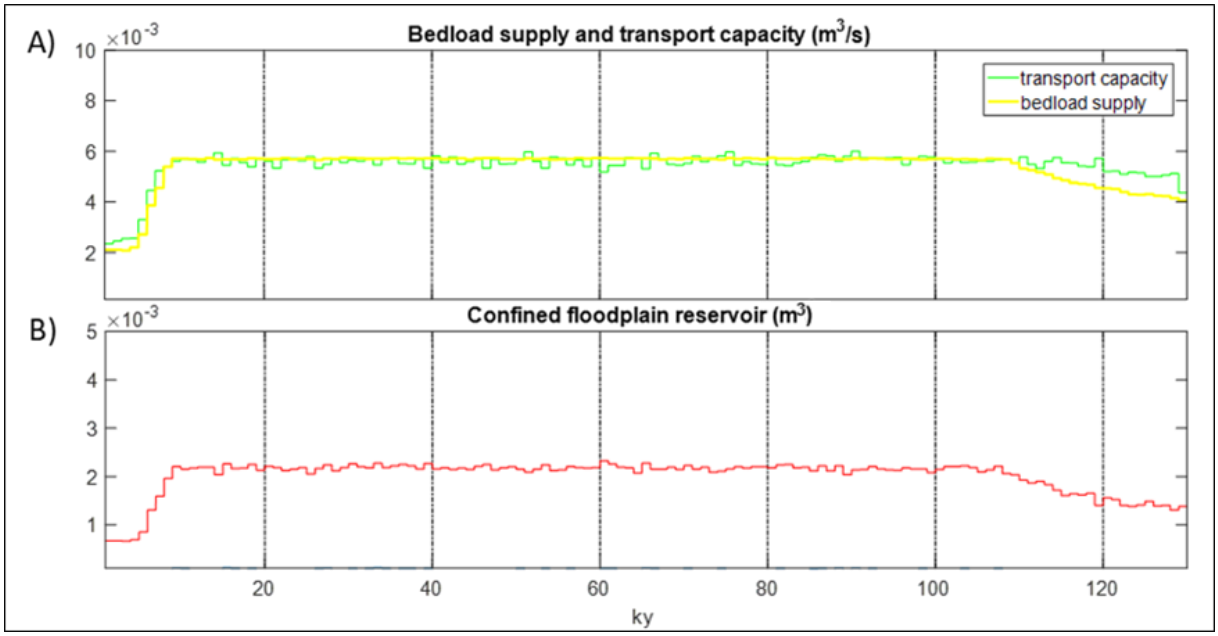

Figure 36. The simulated transport capacity (Panel A) and confined floodplain reservoir (Panel B) as a result of increased median grain size from 0.00025 m to 0.0025 m.